

Free-Surface Enthalpy Method for Transient Convection/Diffusion Phase Change

Amirsaman Farrokhpanah*¹, Javad Mostaghimi¹, and Markus Bussmann¹

¹*Department of Mechanical & Industrial Engineering, University of Toronto, Toronto, Canada*

Abstract

A three-dimensional model is developed for predicting impact and solidification behaviour of droplets generated by Suspension Plasma Spraying (SPS). The model utilizes Smoothed Particle Hydrodynamics (SPH) discretization of enthalpy equation to capture the phase change process. Surface tension is modelled as an internal force between all particles that will be cancelled in the bulk of fluid and generate unbalanced surface tension forces near the free surface. Developed model is validated against various experimental, analytical, and numerical results from literature. Results confirm accuracy and robustness of the new procedures. Finally, the improved SPH model is applied to study of Suspension Plasma Spraying by predicting impact and solidification of molten ceramic droplets on the substrate. These cases include predictions for spread factor and splat formation depending on impact velocities and temperatures. Results are used to explain different processes involved in substrate coating using SPS. Conditions of the droplets at the time of reaching the substrate, i.e. temperature, velocity, and diameter are obtained from a previous study using Finite-Volume and discrete phase models to track flight, evaporation, and atomization of suspension droplets injected into the plasma flow. Effects of high temperature gradients and non-continuum on solid particles in plasma flow are also taken into account.

Keywords: SPH, Phase Change, Suspension Plasma Spraying

1 Introduction

Coating is the process of covering a surface with particular materials with the goal of protection or forming more advanced materials. Thermal spraying, one of the examples of the coating process, uses heat from combustion or electrical arc to melt solid materials. These molten droplets are then accelerated using gas jet to impact a destination substrate and solidify on its surface. Thermal spray, originally driven by its aerospace applications, is

*farrokh@mie.utoronto.ca

now one of the most important methods for wear, thermal, and oxidation protection due to having a high deposition rate over a large area compared to many other coating methods [1]. Coating materials can be ceramics, alloys, polymers, and even composites which can be deposited over a wide range of materials such as plastic, steel, etc. Materials coated with these methods can possess many different properties such as high thermal resistance (thermal barrier coatings), wear protection by improving tribological properties of the surfaces that rub against each other, and antibacterial effects. Better understanding of this process will help in prediction of the properties and structure of the finished surfaces.

An interesting type of thermal spray is the Suspension Plasma Spraying (SPS) process. SPS is emerging as a powerful coating technique for depositing high quality thermal barrier coatings. This process has been demonstrated in figure 1. Fine ceramic powders are used for creating stable suspensions. The solvent can be fluids such as water or ethanol. The heat from plasma evaporates this carrier fluid and then melts the solid matter. The suspension droplets go through several breakups before evaporation is complete. Solid particles left after evaporation can become aggregated before melting. The molten particles will then impact the substrate at high velocities. Understanding effects of different parameters on the final quality of the droplets that impact the substrate helps in better prediction of the coating properties. Physical properties of the suspension, operating conditions of the plasma torch, along with injection parameters, i.e., position, angle, and speed, play important roles in this process. Interaction of the molten droplets upon impact and solidification on the substrate can all contribute to different depositions.

The goal here is to use numerical models to study the SPS process during impact and solidification on the substrate. In this manner, a numerical model explained in [31] is used to study the trajectory of suspension droplets as they get injected into a plasma jet and experience evaporation of the solvent, variation of physical properties of the suspension, and melting of the solid ceramic particles. The solution of this model is used here to study the impact and solidification of the generated ceramic particles in details. Results are used for predicting the quality of the final coated surface of the substrate.

The remainder of this section presents an introduction to the Smoothed Particle Hydrodynamic method followed by a review of numerical models available in literature for study of the phase change process. Details on the phenomena involved in Suspension Plasma Spraying can be found in [31].

1.1 Smoothed Particle Hydrodynamics (SPH)

SPH is a Lagrangian method introduced in the 70s [2, 3] for astrophysics simulations. Many studies since then have adopted the method for simulating different physical phenomena in fields like astrophysics, fluid sciences, oceanography, ballistics, etc. Cases such as tsunami simulations [5], simulation of floating bodies like ships [6], atomization of liquid jets [7], impact of liquid drops over surfaces [8], and other multiphase studies [9, 10, 11] are among those. High computation efficiency through parallelization capability, and the ability of handling complex geometries is among the main advantages of this method.

Many researches have conducted multiphase studies using SPH. An advantage of SPH in interfacial flows is the ability of capturing surface related phenomena using single-phase free-surface methods. For surface tension for instance, the effect is included as an inter-particle

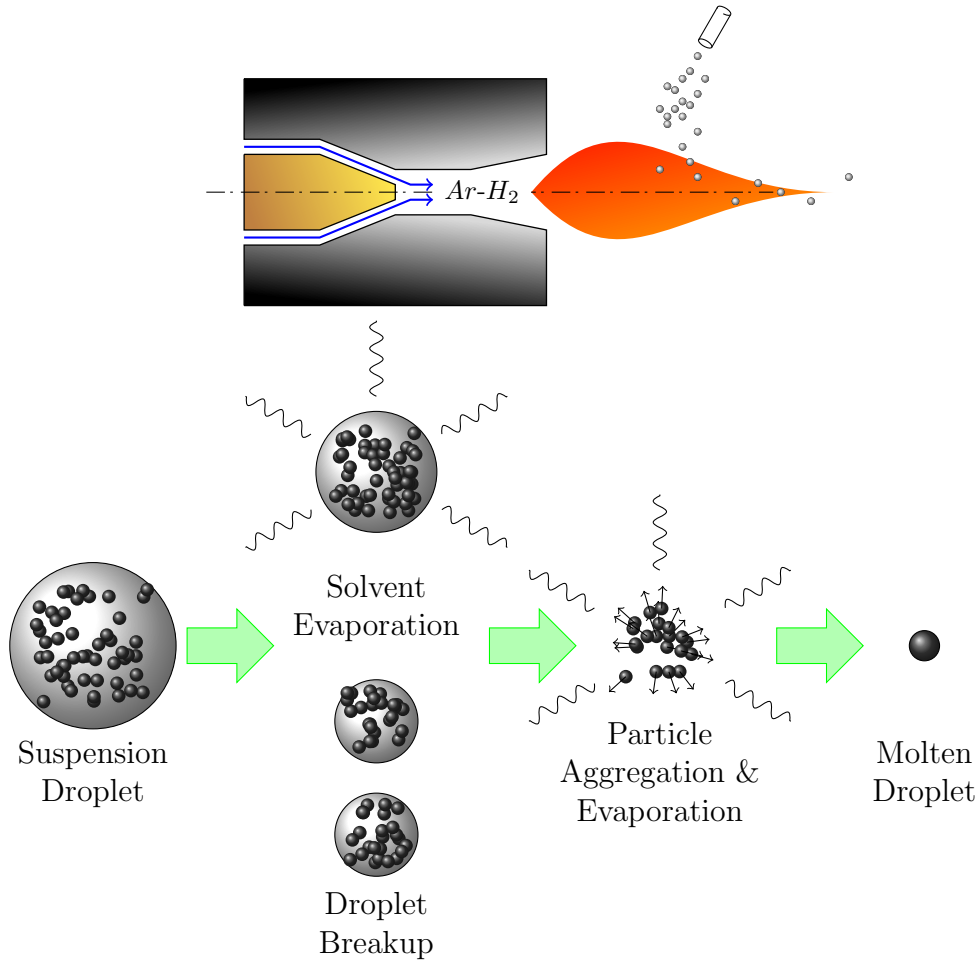


Figure 1: Suspension Plasma Spraying (SPS) process.

attractive force using microscopic analogies [18]. A sample droplet generated by this method is shown in figure 2. These forces cancel one another in the bulk of droplet leaving surface tension effects on the surface due to imbalanced cancellations. These methods are applicable to both single and multiphase problems and eliminate the need for surface reconstruction.

1.2 Phase change: Solidification & Melting

Solidification/melting during heat transfer is of importance in many engineering applications such as painting, freezing or thawing food products, and casting. The amount of heat needed for the phase change process to take place is called the latent heat. This heat is absorbed (released) during solidification (melting) at a constant temperature for pure materials and over a temperature range for alloys. Inclusion of this process into the numerical models demands making modifications to heat transfer calculations. This is either done by adding the heat as a source term, like the works of Passandideh [19] and Voller [20], or by modifying heat capacity coefficient, as in the works of Thomas et al. [21], Hsiao [22], and Dalhuijsen et al. [23].

Finite volume discretization was originally used for phase change studies, followed later

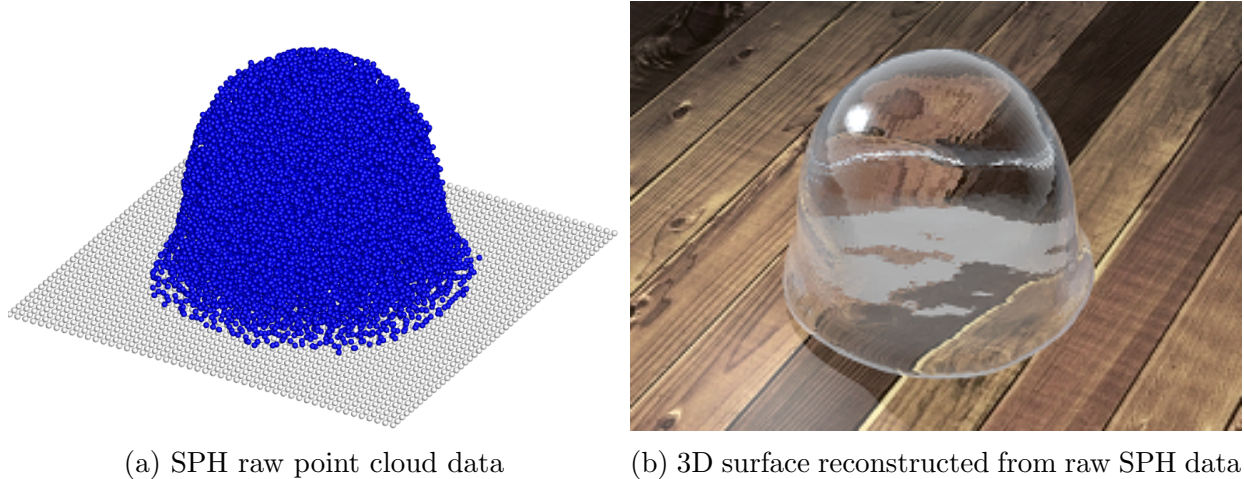


Figure 2: SPH simulation of single-phase droplet using microscopic forces (left) and a rendering of the reconstructed surface (right).

by finite element due to its flexibility in dealing with complex boundaries [23]. Usage of SPH formulations has also been suggested by several studies. Cleary et al. [24, 25] used explicit inclusion of latent heat as a post processing step in solving the enthalpy energy equation. This model has been applied to different studies such as casting [26] and droplet solidification [27, 28, 29]. Monaghan et al. [30] modelled solidification of pure and binary alloys using a stationary grid of ghost particles. The drawback was the need for extra set of particles resulting in doubling the number of particles involved and adding implementation complications.

1.3 This study

This work presents study of impact and solidification of molten Yttria-Stabilized Zirconia (YSZ) droplets on flat and patterned substrates. This process involves two main stages:

1. Suspension mixture is injected as a liquid jet into the plasma torch and is tracked while it goes through evaporation, breakup, and melting before it generates molten particles that reach the substrate. Particle conditions upon reaching the substrate have been obtained here from a separate study explained in [31]. Plasma torch operating conditions and physical properties of ceramic particles used in that study are presented in tables 1 and 2.
2. Smoothed Particle Hydrodynamic (SPH) discretization of the enthalpy equation is used to capture the impact and solidification of the droplets reaching the substrate. Effects of different conditions and initial substrate surface conditions are studied. The solidification model is enhanced here by introducing the SPH discretization of the enthalpy formulation of Cao et al. [40].

The remainder of this manuscript is structured as follows: SPH formulations using integral interpolations are introduced for modelling of the transient convective phase change problem.

These models are benchmarked against various analytical and numerical results to prove robustness of the procedure. Then application of the new model on study of impact and solidification of sub-micron ceramic droplets generated during Suspension Plasma Spraying is presented. Results are used for making predictions on the quality of the final coated substrate.

Table 1: Plasma torch operating conditions according to [31]

Case #	P (kW)	\dot{m} (slpm)
A	7	35
B	7	70
C	7	140
D	14	35
E	21	35

Table 2: Physical properties of Yttria-Stabilized Zirconia (YSZ)

Property	Value
ρ (kg/m^3)	5560
μ ($Pa \cdot s$)	0.029
σ (N/m)	0.43
C_p ($J/(kg \cdot K)$)	678.5
ΔH_{sf} (kJ/kg)	710
k ($W/(m \cdot K)$)	2.4
T_{mp} (K)	2975

2 Governing equations

2.1 Principles

Equations are discretized over a domain filled with SPH particles using integral interpolations. Consider the definition of the Dirac delta (δ) function in the form of

$$\delta(\mathbf{x} - \mathbf{x}_i) = \begin{cases} \infty & \mathbf{x} = \mathbf{x}_i \\ 0 & \mathbf{x} \neq \mathbf{x}_i \end{cases} \quad (1)$$

which has the identity property in the form of $\int_{-\infty}^{\infty} \delta(\mathbf{x} - \mathbf{x}_i) d\mathbf{x} = 1$. For integral representation of a function like $f(\mathbf{x})$, it can easily be shown that

$$\int_{\phi} f(\mathbf{x}) \delta(\mathbf{x} - \mathbf{x}_i) d\mathbf{x} = f(\mathbf{x}_i) \quad (2)$$

A more general case of this integral interpolation can be obtained by substituting delta function with an arbitrary smoothing kernel, $W(\mathbf{x} - \mathbf{x}_i, h)$, which has the following two properties:

$$\lim_{h \rightarrow 0} W(\mathbf{x} - \mathbf{x}_i) = \delta(\mathbf{x} - \mathbf{x}_i) \quad (3)$$

$$\int_{-\infty}^{\infty} W(\mathbf{x} - \mathbf{x}_i) d\mathbf{x} = 1 \quad (4)$$

h , which is usually accompanied by an integer multiplicand, k , determines the radius from \mathbf{x}_i on which the smoothing function is non-zero. Therefore integral interpolation in general form is

$$\int_{\phi} f(\mathbf{x}) W(\mathbf{x} - \mathbf{x}_i) d\mathbf{x} \cong f(\mathbf{x}_i) \quad (5)$$

which is only an approximation of $f(\mathbf{x}_i)$ unless $W(\mathbf{x} - \mathbf{x}_i, h)$ is the Dirac delta function [32]. Using same methodology as of using Riemann sums, the integral above can be turned into a summation in the form of

$$f(\mathbf{x}_i) \cong - \sum_{j=1}^N \frac{m_j}{\rho_j} f(\mathbf{x}_j) W(\mathbf{x}_j - \mathbf{x}_i, h) \quad (6)$$

The gradient (or divergence) of $f(\mathbf{x})$ can also be calculated using the same principles in the form of

$$\nabla f(\mathbf{x}_i) \cong \sum_{j=1}^N \frac{m_j}{\rho_j} f(\mathbf{x}_j) \nabla_i W(\mathbf{x}_j - \mathbf{x}_i, h) \quad (7)$$

It is however beneficial for numerical stability to use the following identities instead

$$\nabla f(\mathbf{x}) = \rho \left[\nabla \left(\frac{f(\mathbf{x})}{\rho} \right) + \frac{f(\mathbf{x})}{\rho^2} \nabla \rho \right]. \quad (8)$$

and

$$\nabla f(\mathbf{x}) = \frac{1}{\rho} [\nabla(\rho f(\mathbf{x})) - f(\mathbf{x}) \nabla \rho] \quad (9)$$

The SPH form of these identities after applying the same principles as mentioned before will be [32]

$$\nabla f(\mathbf{x}_i) = \rho_i \left[\sum_j^N m_j \left(\frac{f(\mathbf{x}_i)}{\rho_i^2} + \frac{f(\mathbf{x}_j)}{\rho_j^2} \right) \nabla_i W_{ij} \right] \quad (10)$$

and

$$\nabla f(\mathbf{x}_i) = \sum_j^N \frac{m_j}{\rho_j} [f(\mathbf{x}_j) - f(\mathbf{x}_i)] \nabla_i W_{ij} \quad (11)$$

2.2 Navier-Stokes equations

Navier-Stokes equations in a Lagrangian framework are

$$\frac{D\rho}{Dt} = -\rho\nabla \cdot v \quad (12)$$

$$\frac{Dv}{Dt} = \frac{1}{\rho}[-\nabla p + \mu\nabla^2 v + F^{st} + F^b] \quad (13)$$

where F^b represents external body forces such as gravity and F^{st} is the surface tension force. These equations are closed by equation of state, which calculates pressure using density in the form of [33]

$$P = P_0\left(\frac{\rho}{\rho_0}\right)^\gamma + b \quad (14)$$

where $\gamma = 7$ and 1.4 for liquid and gas phases, respectively, b is a background pressure, and P_0 represents a reference pressure adjusted to keep maximum density deviations from ρ_0 in the order of $O(1\%)$ [33].

Applying integral interpolation to continuity and Navier-Stokes equations

$$\frac{D\rho_i}{Dt} \cong \sum_{j=1}^N m_j (\mathbf{v}_i - \mathbf{v}_j) \cdot \nabla_i W \quad (15)$$

$$\frac{D\mathbf{v}_i}{Dt} \cong - \sum_{j=1}^N m_j \left(\frac{p_i}{\rho_i^2} + \frac{p_j}{\rho_j^2} \right) \nabla_i W + 4m_j \left(\frac{(\mu_i + \mu_j)\mathbf{x}_{ij} \cdot \nabla_i W}{(\rho_i + \rho_j)^2 |\mathbf{x}_{ij}|^2} \right) \mathbf{v}_{ij} + \frac{\mathbf{F}_{ij}^{st}}{m_i} + \mathbf{F}^b \quad (16)$$

where m is the mass of each particle. To avoid possible singularities, it is beneficial to expand $\frac{\mathbf{x}_{ij} \cdot \nabla_i W}{|\mathbf{x}_{ij}|^2}$ before calculations and remove a position vector that appears in both denominator and numerator, which can become close to or equal to zero.

Surface tension is calculated by applying interaction forces among particles in the form of [34]

$$\mathbf{F}_{ij} = \begin{cases} S_{ij} \cos\left(\frac{1.5\pi}{3h} |\mathbf{x}_{ij}|\right) \frac{\mathbf{x}_{ij}}{|\mathbf{x}_{ij}|} & |\mathbf{x}_{ij}| \leq h \\ 0 & |\mathbf{x}_{ij}| > h \end{cases} \quad (17)$$

between each i and j particles. S_{ij} is a constant that controls the magnitude of surface tension force between each phase. Contact angles and interactions between fluids and solids can be obtained by choosing different values for S_{ij} .

2.3 Particle Tracking

Tracking fluid surface is a challenging task in multiphase CFD studies. Knowledge of fluid interface helps in identifying where each phase is located inside the domain. Position and shape of interface can be used to calculate interfacial forces and phenomena such as surface tension, evaporation, chemical reactions, etc. Different CFD schemes have been used in tracking fluid interface. In Volume of Fluid Method (VOF), free surface is tracked by advection of a fraction function (C). This fraction function has a value of 1 at one phase,

0 at the other, and a value between 0 and 1 at the interface. The value of this function is then advected through cells on domain based on fluid velocity vectors by

$$\frac{\partial C}{\partial t} + v \cdot \nabla C = 0 \quad (18)$$

A similar methodology is also used in Level Set method. Here a function like ϕ is defined to divide the domain to three regions. ϕ gets the value of 0 on the fluid surface, has positive values on one side, and negative values on the other side of the interface. This curve is then moved using the same methodology as VOF by solving

$$\frac{\partial \phi}{\partial t} = v |\nabla \phi| \quad (19)$$

One of disadvantages of level set is the fact that it cannot conserve mass [35]. Both level set and VOF also need to have the equations mentioned before solved on the fluid domain which can be computationally expensive. SPH, being a Lagrangian method can help in removing this problem. Position of each SPH particle is updated at each iteration using

$$\frac{Dx}{Dt} = v \quad (20)$$

This makes sure that all particles, including those which form the interface, are moving with the fluid velocity. This procedure not only conserves mass exactly, but also rules out the need for solving any additional advection equation. In this method, particles of each phase are only needed to be marked once and the exact position of each phase will be available at any time due to the movement of the particles.

2.4 Boundaries

For particles that come in contact with a wall, the no-slip boundary condition needs to be applied. A proper implementation of this condition is of more importance in the scope of current work, as in most cases studied later, the fluid comes in contact with wall at comparably large velocities. Morris et al. [4] suggested giving the stationary wall particles an artificial velocity in the opposite direction of fluid flow. In this method, the distance of each particle from the wall needs to be calculated. Assuming the distance of a fluid particle outside the wall and the distance of a solid particle inside the wall are given as d_{fluid} and d_{solid} , the artificial velocity vector for solid particles can be calculated from

$$\mathbf{V}_{solid} = -\frac{d_{solid}}{d_{fluid}} \mathbf{V}_{fluid} \quad (21)$$

To avoid large velocities when particles are too close to the walls, it is customary to limit the value of $\frac{d_{solid}}{d_{fluid}}$ by 0.5. The main disadvantage of this formulation is that the exact location of the wall needs to be known prior to calculation. For instance, for cases with curved or vertical walls, or with moving boundaries such as a growing solidification front, the implementation of this algorithm is inefficient. To overcome this, Holmes et al. [36]

have proposed an alternative method. For each particle i , a state-specific particle density is defined as

$$\bar{n}_i = \sum_j \delta W(x_{ij}, h) \quad (22)$$

with δ being 1 when particles i and j are of the same state (both fluid or both solid), and 0 otherwise. In addition, a second particle density is defined which now contains all solid and fluid particles in the neighborhood of particle i

$$n_i = \sum W(x_{ij}, h) \quad (23)$$

It is evident that the ratio of \bar{n}_i and n_i , $\chi = \frac{\bar{n}_i}{n_i}$, is inversely proportional to the number of particles from the other phase existing in the neighborhood of particle i . For particles in the bulk of fluid (or solid), $\chi_i = 1$, for particles located exactly on the wall, $\chi_i = 0.5$, and for the rest χ_i is between these two limits. Using this ratio, Holmes et al. [36] have shown that the artificial velocity of solid particles in the wall can be calculated from

$$\mathbf{V}_{\text{solid}} = -\frac{\zeta_{\text{solid}}}{\max\left(\zeta_{\text{fluid}}, \frac{\sqrt{3}}{4}h\right)} \mathbf{V}_{\text{fluid}} \quad (24)$$

with $\zeta = \frac{kh}{0.5}(\chi - 0.5)$. This formulation can be used to satisfy the no-slip boundary condition on both flat and curved boundaries and hence has been used here.

Aside from the no-slip boundary condition, particles at high velocities may also penetrate the walls. To prevent this, a short-range repulsive force is placed on wall particles. This force is only active when the fluid particle is too close to a wall particle, say their distance is below initial particle spacing. This force is typically chosen in the form of Lennard-Jones potential as

$$f(x) = \begin{cases} D \left[\left(\frac{x_0}{|\mathbf{x}^*|}\right)^{12} - \left(\frac{x_0}{|\mathbf{x}^*|}\right)^6 \right] \frac{\mathbf{x}^*}{|\mathbf{x}^*|^2} & |\mathbf{x}^*| < x_0 \\ 0 & |\mathbf{x}^*| \geq x_0 \end{cases} \quad (25)$$

where D is a constant used for calibration, \mathbf{x}^* is the position vector pointing from the boundary particle towards the target fluid particle, and x_0 is the cutoff distance, taken equal to the initial particle spacing here.

2.5 Tensile Instability

It is a widely known concept that SPH particles subjected to negative pressures show tendency of forming small clusters. While simulation results are typically not significantly affected in the larger scale from this arrangement, it becomes important for the test cases of interest here. Having large impact velocities leads to large displacements in particle positions. For a single droplet impact, as particles in the drop are typically arranged nicely before the impact, this is not problematic. However, when multiple particles are impacting one after another, the particles from previous impacts, that now are in near stationary condition might have formed clusters, that would cause instabilities after secondary impacts.

Moreover, as the solidification front moves across the particles, solidification of a portion of particles in a cluster will make the solution unstable, as particles that prior to solidification were closer to one another and in equilibrium, will now be unbalanced and too close to solid particles to properly recover their positions. To overcome this, a proper model needs to be used to limit particle clusterings. Tensile instabilities have been studied in detail by studies such as Melen et al. [37] and Gray et al. [38]. Treatments offered by these studies, while being effective, are computationally costly. It was found here that more simple solutions, such as the model of Monaghan [39], also worked well in the current framework. In this algorithm, a correction term is added to the momentum equation which adjusts particles when negative pressures are present in the form of

$$\Pi = R^* f_{ij}^n \quad (26)$$

Here, $f_{ij} = \frac{W(x_{ij}, h)}{W(x_0, h)}$. x_0 is the initial spacing between particles, and n has the value of 4. The factor, R^* , is written as

$$R^* = R_i^* + R_j^* \quad (27)$$

where the value for R_i and R_j is calculated from

$$R_i = \begin{cases} \epsilon \frac{|p_i|}{\rho_i^2} & \text{if } p_i < 0 \\ 0 & \text{otherwise} \end{cases} \quad (28)$$

where ϵ is a problem dependent constant. Monaghan has also suggested including a correction term for particles with positive pressures in the form of

$$R^* = 0.01 \left(\frac{p_i}{\rho_i^2} + \frac{p_j}{\rho_j^2} \right) \quad (29)$$

2.6 Time Marching

In the current scope, particle positions and the rest of variables are updated at each time step using the conventional SPH formulation in the form of

$$\frac{D\mathbf{x}_i}{Dt} = \mathbf{V}_i \quad (30)$$

Algorithms such as velocity-verlet, Leapfrog, predictor-corrector, or Runge-Kutta can be used for performing numerical integration. The Leapfrog method has been chosen here. As explicit time marching schemes are stable under Courant-Friedrichs-Lewy (CFL) condition, time steps are limited here using

$$\Delta t \leq 0.25 \frac{h}{c} \quad (31)$$

where c is the speed of sound. Also based on viscous diffusion, another constraint can be imposed in the form of

$$\Delta t \leq 0.125 \frac{h^2}{\nu_{max}} \quad (32)$$

with ν being the maximum kinematic viscosity in the domain. For when acceleration forces are large, it is also beneficial to write a constraint based on the magnitude of forces exerted on each particle (f)

$$\Delta t \leq 0.125 \left(\frac{h}{f} \right)^{0.5} \quad (33)$$

The value of time steps are also limited by the choice of neighbour search algorithm. Depending on how particle neighbours are updated, time steps should be limited to prevent a particle from escaping or entering a neighbourhood without getting noticed.

2.7 Energy equation

The energy equation here is solved using methodology proposed by Cao et al. [40]. The three dimensional energy equation for laminar flow with no viscous dissipation is

$$\frac{\partial}{\partial t} (\rho H) + \frac{\partial}{\partial x} (\rho u H) + \frac{\partial}{\partial y} (\rho v H) + \frac{\partial}{\partial z} (\rho w H) = \frac{\partial}{\partial x} \left(k \frac{\partial T}{\partial x} \right) + \frac{\partial}{\partial y} \left(k \frac{\partial T}{\partial y} \right) + \frac{\partial}{\partial z} \left(k \frac{\partial T}{\partial z} \right) \quad (34)$$

For an incompressible fluid,

$$\frac{dH}{dT} = C(T) \quad (35)$$

Enthalpy is calculated with respect to a reference point. In the current context, the reference point is chosen to be the melting point of the solid material. At this temperature, enthalpy is assumed to be zero (see figure 3).

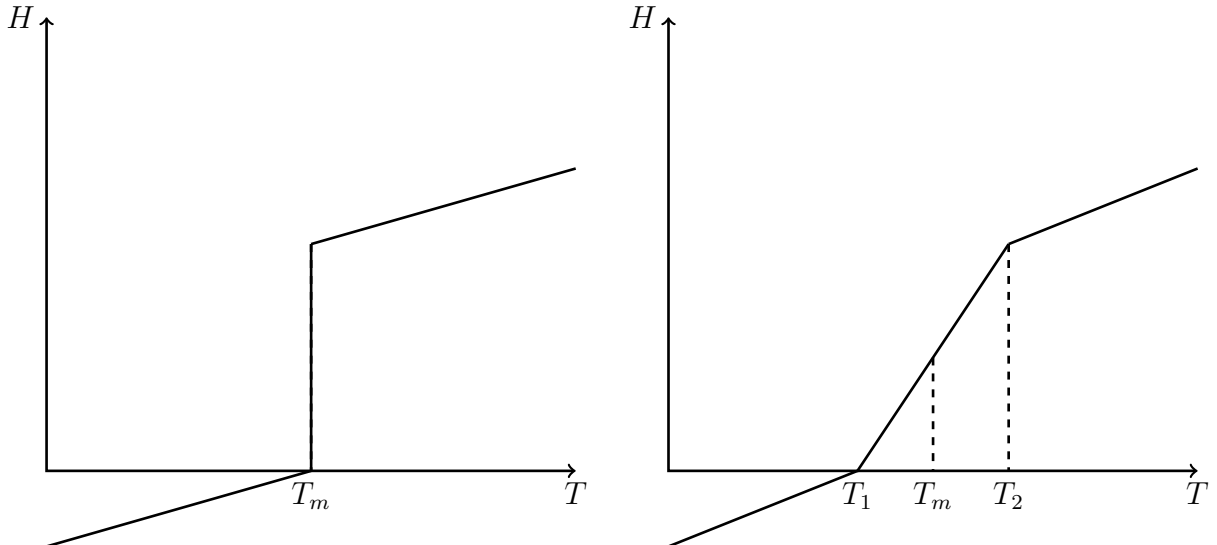


Figure 3: Enthalpy variation for a material with a single phase change temperature (left) and phase change over a temperature interval (right).

2.7.1 Temperature Calculation

Using this assumption along with equation 35, temperature can be calculated. For a pure substance with phase change at a single temperature,

$$T = \begin{cases} T_m + H/C_s & H \leq 0 \\ T_m & 0 < H < L \\ T_m + (H - L)/C_l & H \geq L \end{cases} \quad (36)$$

and for materials like alloys where phase change occurs over a temperature range,

$$T - T_1 = \begin{cases} H/C_s & H \leq 0 & \text{solid} \\ \Delta TH/(L + C_m \Delta T) & 0 < H < L + C_m \Delta T & \text{mushy} \\ H/C_l - [L + (C_m - C_l) \Delta T]/C_l & H \geq L + C_m \Delta T & \text{liquid} \end{cases} \quad (37)$$

As shown in figure 3, for materials where phase change occurs at a single temperature, enthalpy experiences a step jump at the melting temperature (T_m). For materials such as alloys with a phase change temperature interval (PCTI), phase change occurs over a temperature range T_1 to T_2 . When the temperature is within the PCTI, the material is mushy. In the current study and equation 37, enthalpy is assumed to vary linearly over the PCTI.

2.7.2 Kirchhoff temperature

In order to eliminate the constant values in equations 36 and 37, the Kirchhoff temperature is defined as $T^* = \int_{T_{ref}}^T k(\zeta) d\zeta$. Applying this definition to equations 36 and 37 gives

$$T^* = \begin{cases} k_s(T - T_m) & T < T_m \\ 0 & T = T_m \\ k_l(T - T_m) & T > T_m \end{cases} \quad (38)$$

for a material with a single phase change temperature and

$$T^* = \begin{cases} k_s(T - T_1) & T \leq T_1 \\ k_m(T - T_1) & T_1 < T < T_2 \\ k_l(T - T_1) & T \geq T_2 \end{cases} \quad (39)$$

for a material that changes phase over a temperature interval.

The constant values T_m and T_1 can now be omitted by substituting T from equations 36 and 37 into equations 38 and 39, respectively. This gives the Kirchhoff temperature as a function of enthalpy in the form of

$$T^* = \begin{cases} k_s H/C_s & H \leq 0 \\ 0 & 0 < H < L \\ k_l (H - L)/C_l & H \geq L \end{cases} \quad (40)$$

for a single phase change temperature and

$$T^* = \begin{cases} k_s H/C_s & H \leq 0 \\ k_m [\Delta TH/(L + C_m \Delta T)] & 0 < H < L + C_m \Delta T \\ k_l [H/C_l - [L + (C_m - C_l) \Delta T]/C_l] & H \geq L + C_m \Delta T \end{cases} \quad (41)$$

for phase change over a temperature range. The linearity of equations 40 and 41 allows the calculation of H or T^* when only one is known.

2.7.3 Source terms

Expressing $T^* = \Gamma(H)H + S(H)$, Γ and S can be derived from equations 40 and 41 as

$$\Gamma(H) = \begin{cases} k_s/C_s & H \leq 0 \\ 0 & 0 < H < L \\ k_l/C_l & H \geq L \end{cases} \quad S(H) = \begin{cases} 0 & H \leq 0 \\ 0 & 0 < H < L \\ -Lk_l/C_l & H \geq L \end{cases} \quad (42)$$

for a single temperature phase change and

$$\Gamma(H) = \begin{cases} k_s/C_s & H \leq 0 \\ k_m\Delta T/(L + C_m\Delta T) & 0 < H < L + C_m\Delta T \\ k_l/C_l & H \geq L + C_m\Delta T \end{cases} \quad (43)$$

$$S(H) = \begin{cases} 0 & H \leq 0 \\ 0 & 0 < H < L + C_m\Delta T \\ k_l[L + (C_m - C_l)\Delta T]/C_l & H \geq L + C_m\Delta T \end{cases}$$

for phase change over a temperature range.

2.7.4 Reconstruction of Lagrangian energy equation

With the definition of T^* , equation 34 can be rewritten as

$$\frac{\partial}{\partial t}(\rho H) + \frac{\partial}{\partial x}(\rho u H) + \frac{\partial}{\partial y}(\rho v H) + \frac{\partial}{\partial z}(\rho w H) = \frac{\partial^2 T^*}{\partial x^2} + \frac{\partial^2 T^*}{\partial y^2} + \frac{\partial^2 T^*}{\partial z^2} \quad (44)$$

and further expansion of T^* using equations 42 or 43 transforms equation 44 into

$$\frac{\partial}{\partial t}(\rho H) + \frac{\partial}{\partial x}(\rho u H) + \frac{\partial}{\partial y}(\rho v H) + \frac{\partial}{\partial z}(\rho w H) = \frac{\partial^2(\Gamma H)}{\partial x^2} + \frac{\partial^2(\Gamma H)}{\partial y^2} + \frac{\partial^2(\Gamma H)}{\partial z^2} + \frac{\partial^2 S}{\partial x^2} + \frac{\partial^2 S}{\partial y^2} + \frac{\partial^2 S}{\partial z^2} \quad (45)$$

For simplicity of notations, equation 44 can be rewritten as

$$\frac{\partial}{\partial t}(\rho H) + \nabla \cdot (\rho H \mathbf{V}) = \nabla^2 T^* \quad (46)$$

By expanding $\nabla \cdot (\rho H \mathbf{V})$ into

$$\frac{\partial}{\partial t}(\rho H) + \mathbf{V} \cdot \nabla(\rho H) + (\rho H) \nabla \cdot \mathbf{V} = \nabla^2 T^* \quad (47)$$

the first two terms on the left hand side can be combined to form a total derivative,

$$\frac{D(\rho H)}{Dt} = -(\rho H) \nabla \cdot \mathbf{V} + \nabla^2 T^* \quad (48)$$

Equation 48 for the total derivative is the Lagrangian form of the transformed enthalpy equation. This equation gives the variation of ρH with time for each SPH particle. Using the Lagrangian continuity equation $\frac{D\rho}{Dt} + \rho \nabla \cdot \mathbf{V} = 0$, the term $-\rho \nabla \cdot \mathbf{V}$ in equation 48 can be replaced by the total derivative of density resulting in

$$\frac{D(\rho H)}{Dt} = H \frac{D\rho}{Dt} + \nabla^2 T^* \quad (49)$$

2.8 SPH discretization

The enthalpy equation, in the form of equation 49, is discretized using an SPH formulation here. This equation resolves enthalpy while applying the effects of phase change latent heat. Here, ρH is taken as a single variable. At each iteration, the variation of ρH with respect to time is calculated and is used to obtain a new value for ρH for each particle in an explicit manner. Wherever a value of H is needed, ρH for that particle is divided by its density. In this case, equation 49 for particle i is written as

$$\frac{D(\rho H)_i}{Dt} = H_i \frac{D\rho_i}{Dt} + (\nabla^2 T^*)_i = H_i \frac{D\rho_i}{Dt} + (\nabla^2 \Gamma H)_i + (\nabla^2 S)_i \quad (50)$$

In equation 50, the values for H_i and $D\rho_i/Dt$ are known for each particle. The Laplacians for ΓH and S must be discretized and calculated in SPH form. To ensure numerical stability, these Laplacians are broken into two steps in the form of

$$(\nabla^2 \Gamma H)_i + (\nabla^2 S)_i = \nabla_i \cdot (\nabla_i(\Gamma H) + \nabla_i S) \quad (51)$$

The inner gradient is calculated here using equation 52 while the outer divergence is calculated using equation 53

$$\nabla f(x_i) = \sum_j^N \frac{m_j}{\rho_i} [f(x_j) - f(x_i)] \cdot \nabla_i W_{ij} \quad (52)$$

$$\nabla \cdot \Phi(\mathbf{x}_i) = \rho_i \left[\sum_j^N m_j \left(\frac{\Phi(\mathbf{x}_i)}{\rho_i^2} + \frac{\Phi(\mathbf{x}_j)}{\rho_j^2} \right) \cdot \nabla_i W_{ij} \right] \quad (53)$$

In this manner, the inner gradient in equation 50 becomes

$$\mathbf{G}_i = \nabla_i(\Gamma H) + \nabla_i S = \sum_j^N \frac{m_j}{\rho_i} \{ [\Gamma(H_j)H_j + S(H_j)] - [\Gamma(H_i)H_i + S(H_i)] \} \nabla_i \mathbf{W}_{ij} \quad (54)$$

Here, the values for Γ and S are calculated using equations 42 and 43 using the values of H at the particles i and j . Then the outer divergence in equation 51 becomes

$$(\nabla \cdot \mathbf{G})_i = \rho_i \left[\sum_j^N m_j \left(\frac{\mathbf{G}_i}{\rho_i^2} + \frac{\mathbf{G}_j}{\rho_j^2} \right) \cdot \nabla_i \mathbf{W}_{ij} \right] \quad (55)$$

These discretizations, however, can become unstable in some cases, especially when there is a discontinuity in the physical properties in the domain [41], for example, heat transfer between two materials with different thermal conductivities. To overcome this issue, a remedy suggested by Cleary et al. [41] has been used here. With this new formulation, the Laplacians in equation 50 are directly calculated using

$$\nabla^2(\Gamma H + S)_i = \sum_j^N 2 \frac{m_j}{\rho_j} (f_i - f_j) \frac{\nabla_i W_{ij}}{r_{ij}} \quad (56)$$

where the variable f is defined as

$$\begin{aligned} f_i &= \Gamma_{eff} H_i + S_i \\ f_j &= \Gamma_{eff} H_j + S_j \end{aligned} \quad (57)$$

and Γ_{eff} is defined as

$$\Gamma_{eff} = \begin{cases} \frac{2\Gamma_i\Gamma_j}{\Gamma_i+\Gamma_j} & \Gamma \neq 0 \\ 0 & otherwise \end{cases} \quad (58)$$

Substituting back into equation 50, the variations of ρH for particle i is calculated from

$$\frac{D(\rho H)_i}{Dt} = H_i \left(\frac{D\rho}{Dt} \right)_i + \nabla^2(\Gamma H + S)_i \quad (59)$$

As discussed before for the case of alloys, phase change goes through a mushy zone during melting and solidification. The existence of this region is due to the difference in phase change temperatures of elements forming the alloy. One element might start the solidification process sooner and along the way, the solid crystals that will nucleate and grow will lead to a slurry of solid and molten materials. This phenomena might happen in various ways. In one, the solidified phases might be growing at discrete sites. In this manner, the physical properties of the mixture will be closer to those of a suspension of solid phases in a liquid phase. On the other hand, the solidification might be happening as a solid front growing from a wall. This solid front will have smaller scale porous branches that spread into the heart of the still molten phase. In this manner, the liquid phase will be flowing through the porous solid phase that is growing in size. The flow in this case will be close to flow of liquid phase through porous material. Detailed explanations of these conditions can be found in the work of Voller et al. [42].

The effect of the mushy region is typically included in one of two ways. When the flow pattern is similar to flow through porous media, a Darcy source term can be added to the momentum equation, to account for the pressure drop for the fluid moving through pores. This flow is usually found in casting problems [42]. When the flow is more homogeneous, the effect of having a slurry-like mixture is accounted for by modifying the viscosity. In the current study, this approach has been chosen as it avoids variations in pressure forces that can lead to instabilities in SPH. Depending on the temperature or enthalpy values, a liquid fraction α and a solid fraction $\beta = 1 - \alpha$ can be defined for each particle at each iteration. Based on these values, the viscosity of each particle is updated using [42]

$$\mu = \alpha \mu_{liquid} + \beta \mu_{solid} \quad (60)$$

For particles that have a liquid fraction of unity, a new viscosity will be equal to the viscosity of the molten material. For liquid fractions of zero, the viscosity of each particle is set to very large to mimic solid matter. In between these two limits, viscosity is varied linearly. Some researchers have substituted this linear variation with [43]

$$\mu = \mu_{liquid} \left(1 + C \frac{\beta^3}{(1 - \beta)^3 + \epsilon} \right) \quad (61)$$

where C is a problem dependent constant and ϵ is introduced to avoid division by zero. The values for viscosity need to be calibrated for different materials and conditions. As will be shown later, equation 60 provides more stable solutions in the current framework and hence has been utilized in this study.

3 Validation and Results

3.1 Conduction Problem

3.1.1 Comparison to Analytical Solution

Similar to Cleary et al. [41], a two-dimensional infinite slab is assumed in $x - y$ plane with a temperature discontinuity in its middle at $x = 0$. The material properties are ρ_1, k_1, C_1 when $x < 0$ and ρ_2, k_2, C_2 when $x > 0$. The transient analytical solution to this problem with an initial temperature jump of T_0 across the discontinuity is in the form of [44]

$$T - T_{01} = \begin{cases} \frac{k_1 \alpha_1^{-1/2} T_0}{k_1 \alpha_1^{-1/2} + k_2 \alpha_2^{-1/2}} \left[1 + \frac{k_2 \alpha_2^{-1/2}}{k_1 \alpha_1^{-1/2}} \operatorname{erf} \left(\frac{x}{2\sqrt{\alpha_1 t}} \right) \right] & x > 0 \\ \frac{k_1 \alpha_1^{-1/2} T_0}{k_1 \alpha_1^{-1/2} + k_2 \alpha_2^{-1/2}} \left[\operatorname{erfc} \left(\frac{|x|}{2\sqrt{\alpha_2 t}} \right) \right] & x < 0 \end{cases} \quad (62)$$

Here, $\alpha = k/\rho C$ is the thermal diffusivity. To avoid the complications of modeling an infinite slab, the problem is modeled here with slight modifications[41]. To make the heat transfer one dimensional, a periodic boundary condition is applied perpendicular to heat flow direction in y direction. The x axis is also limited to $-1 < x < 1$ and a no-heat flux boundary condition is applied to its ends. It is evident the temperature profile will be slightly different than the analytical solution near the x limits, especially as time goes to infinity. The value of the temperature across all points should converge to $T_0/2$ by the end. These test cases are conducted with 80 particles in x direction. For the first case, the temperature jump and all thermal properties are taken to be unity. Figure 4 shows the temperature profile for this case for 0, 1, 3, 8, 10, and 20 μs . The solid lines in this figure are the analytical solutions obtained from equation 62. As expected, temperature values near the x limits of -1 and 1 start deviating from the analytical solution as time becomes larger. The values of temperature in the middle of the slab however are a good match to the analytical solution. The second case shows performance under discontinuity in thermal properties. The temperature jump is taken to be 10 and thermal properties of materials are same as before with the exception of $k_1 = 10$.

Figure 5 clearly shows that for small times, the simulation produces a perfect match to the analytical solution. As time grows, so does the error especially close to the boundaries. The

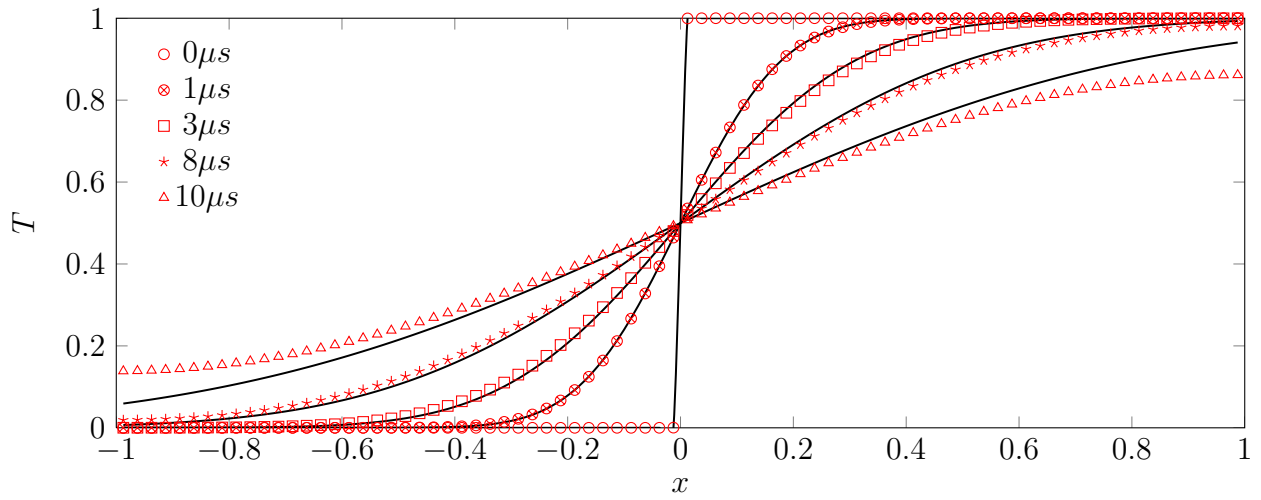


Figure 4: Temperature profile across the slab with an initial unit temperature jump at $x = 0$.

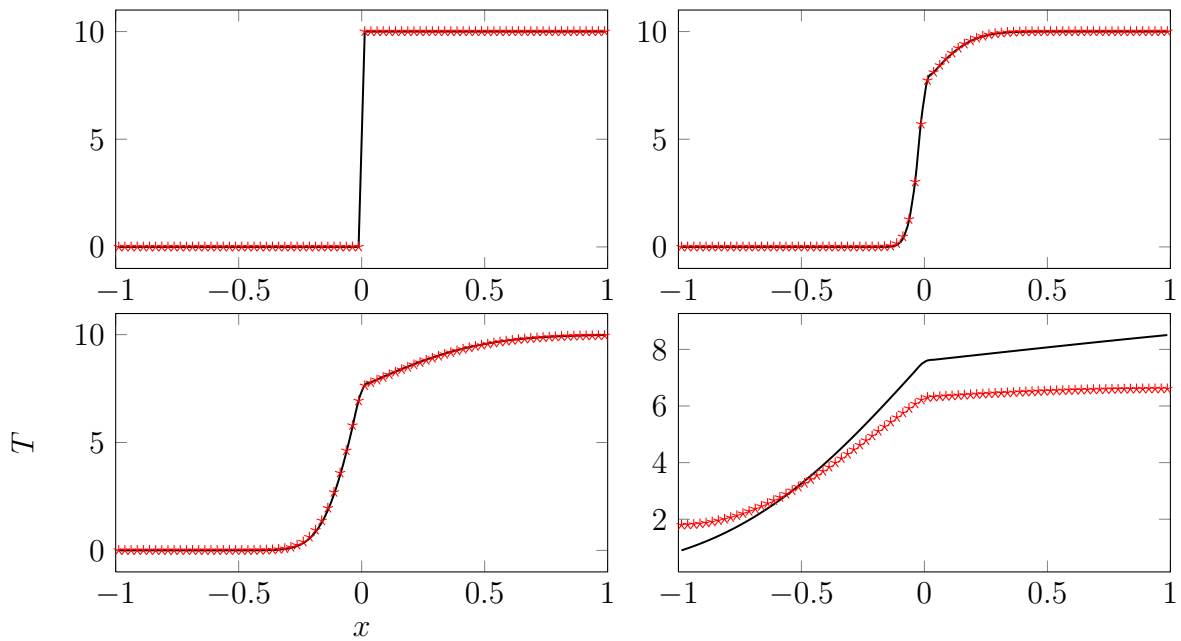


Figure 5: Temperature profile across a slab with a temperature jump of 10 at $t = 0$, $1ms$, $7ms$, and $0.2s$.

error values for this test case, calculated in the form of $L_2 = \sqrt{\frac{1}{N} \sum_{i=1}^N (T_i^{SPH} - T_i^{exact})^2}$, are plotted in figure 6.

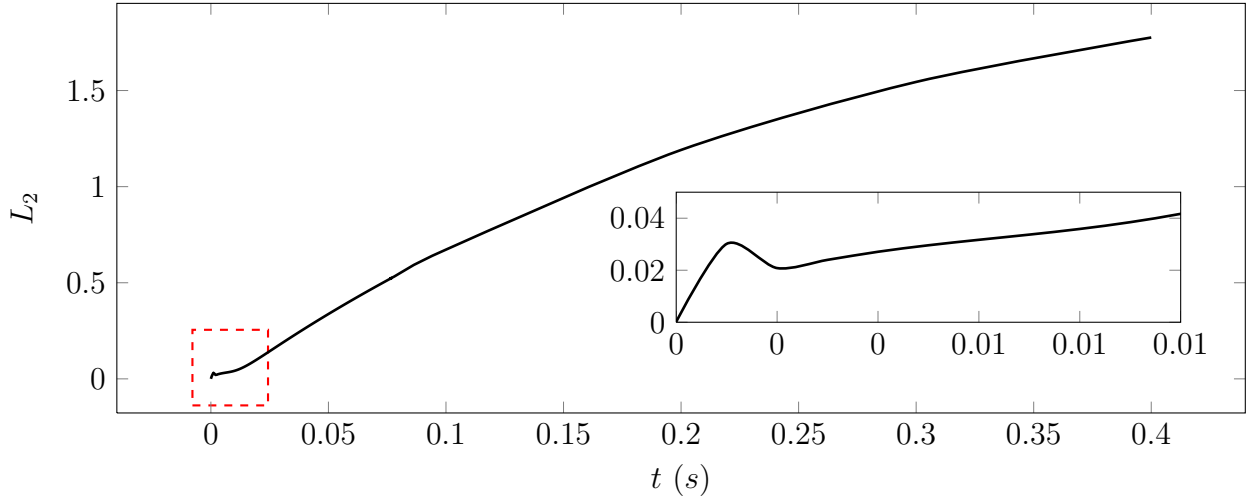


Figure 6: L_2 error values for temperature profile across a slab with a temperature jump of 10.

3.1.2 Comparison to Numerical Solution

For numerical comparison, result generated by the ANSYS Fluent software (Canonsburg, PA, USA) is used as benchmark. A two-dimensional solid square plate with a dimensionless side length of 1 is considered. The transient heat conduction inside this square is captured as it is heated from its sides. For simplicity, the density, thermal conductivity, and heat capacity are all chosen to be unity as well. The plate is initially at zero temperature. At $t > 0$, the temperature of the walls is set to unity. The test case is performed once using the SPH solver presented here, and once using the Fluent solver. Transient temperature profile on the diagonal of the square and the error values have been plotted in figures 7 and 8, respectively.

3.2 Two-dimensional Problem: Phase Change in the Corner of a Square

For the test cases described below, SPH particles are uniformly distributed with spacing of $\Delta x = \Delta y$ over the cross section of the cuboid as shown in figure 9. Domain is periodic in z direction. Since each particle has a neighbourhood with a radius of $3\Delta x$, 3 layers of particles have been placed in the wall in order to make sure all inner particles have a complete neighbourhood. Depending how the values of gradients at wall particles are calculated, these 3 layers of particles might need to have a full neighbourhood of particles. Although test cases show results are not much affected by this, in order to have valid gradients calculated at these 3 layers of wall particles, an extra 3 more layers are also added in the walls here to make

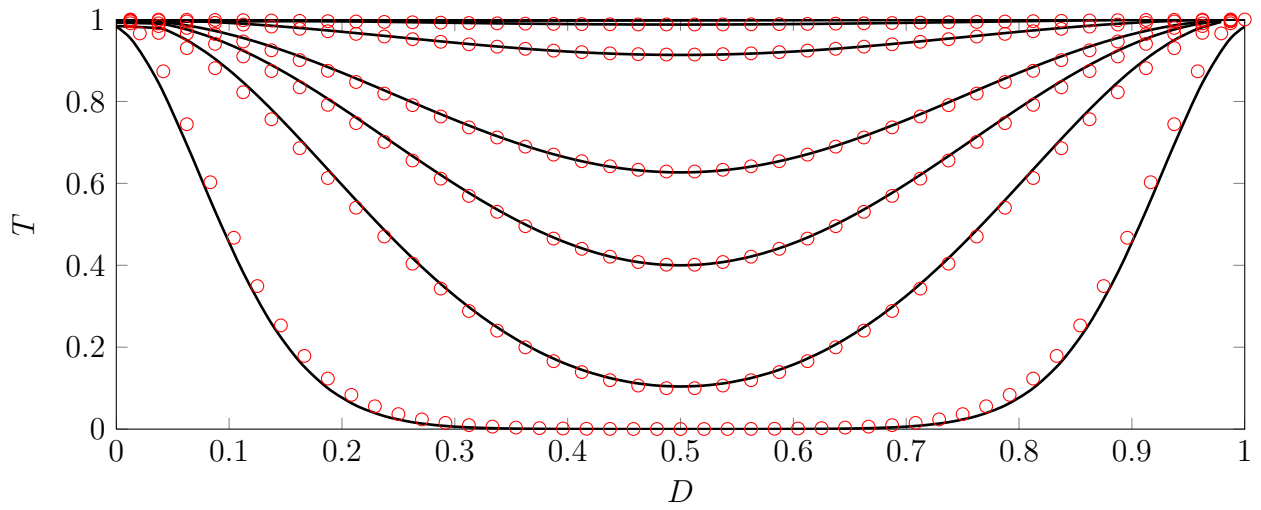


Figure 7: Temperature on the diagonal of the square for $t = 5, 25, 50, 75, 150,$ and $250ms$ (from bottom to top, respectively).

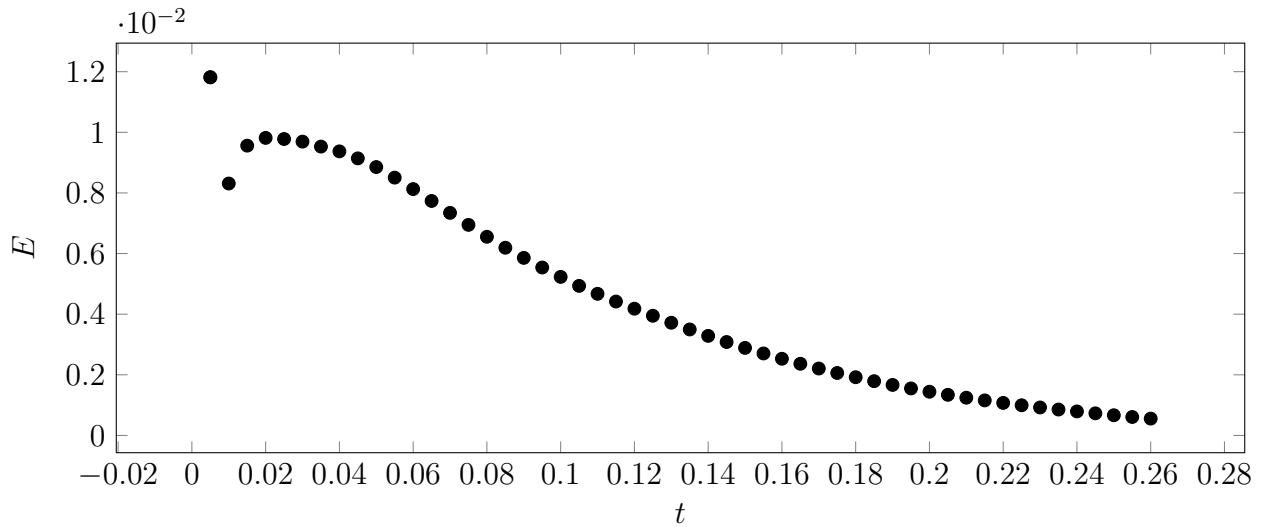


Figure 8: Difference in computed temperature values on the diagonal of the square plate, $E = \max(|T_{SPH} - T_{Fluent}|)$.

sure all wall particles that directly interact with inner particles have a full neighbourhood. The value of temperature of all wall particles are kept constant through all iterations.

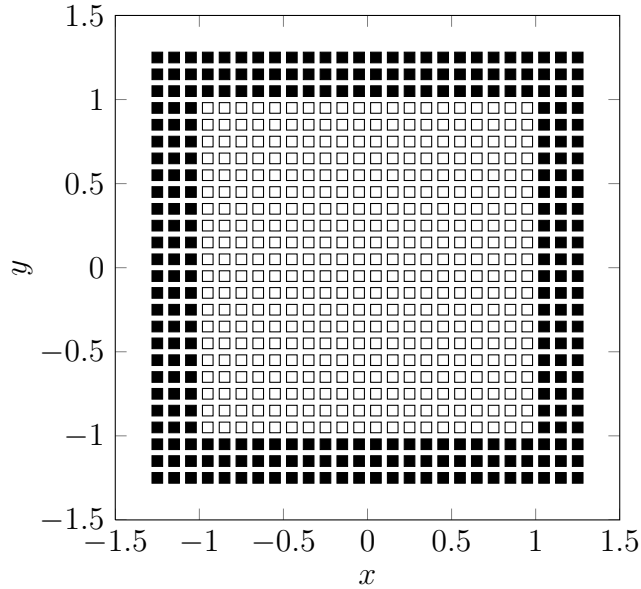


Figure 9: Initial positioning of fluid/solid particles (hollow squares) and wall particles (filled squares).

3.2.1 Comparison to Numerical Results

The numerical results available in literature for the Stefan problem are used for numerical validation of the model in the presence of phase change. To simulate the Stefan problem, the three dimensional cuboid shown in figure 10 is filled with fluid which is at liquid state initially. Solidification will start as the temperature of the walls drop to a value below freezing. This problem has been widely used in literature as a benchmark. In most of reported cases, only a portion of cuboid cross section is simulated (1/4 or 1/8). The boundaries inside fluid for these cases are assumed adiabatic due to the symmetry in this problem. Here however the prism is fully modelled. In z direction, a periodic boundary condition is imposed. For the wall, as SPH particles here see three particles immediate to them in their neighbourhood based on current configurations, three layers of particles with static ρH values are placed on the wall. In this way, it is made sure that all inner particles have complete wall neighbouring particles with wall temperature. All properties for solid and liquid are assumed to remain constant in each phase. Density is also assumed to be constant and equal for both phases. For the initial problem, fluid is assumed to be in liquid form and close to freezing temperature. Wall temperature is suddenly dropped below freezing point and solidification starts from the boundaries toward the centre of cuboid. Fluid and solid properties are assumed to be constant and the values for non-dimensional parameters are $\theta = (T_i - T_w)/(T_m - T_w) = 1$ and $St = C_s(T_m - T_w)/L = 0.641$. Figure 11 shows the solidification front along the diagonal of cross section of the cuboid. For comparison, results reported by Cao et al. [40], Crowley [45], and Hsiao et al. [22] have also been plotted in this figure.

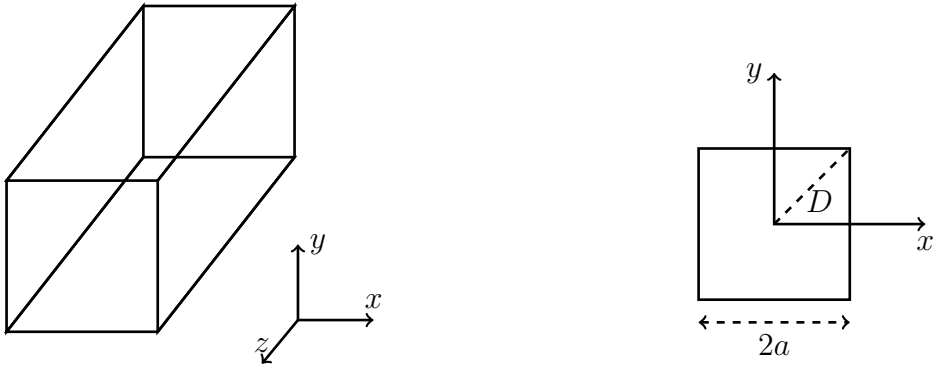


Figure 10: Problem description: fluid is assumed to be inside a Cuboid which is infinitely long in z direction. At the start of simulation, temperature at walls is suddenly dropped to a value below freezing temperature.

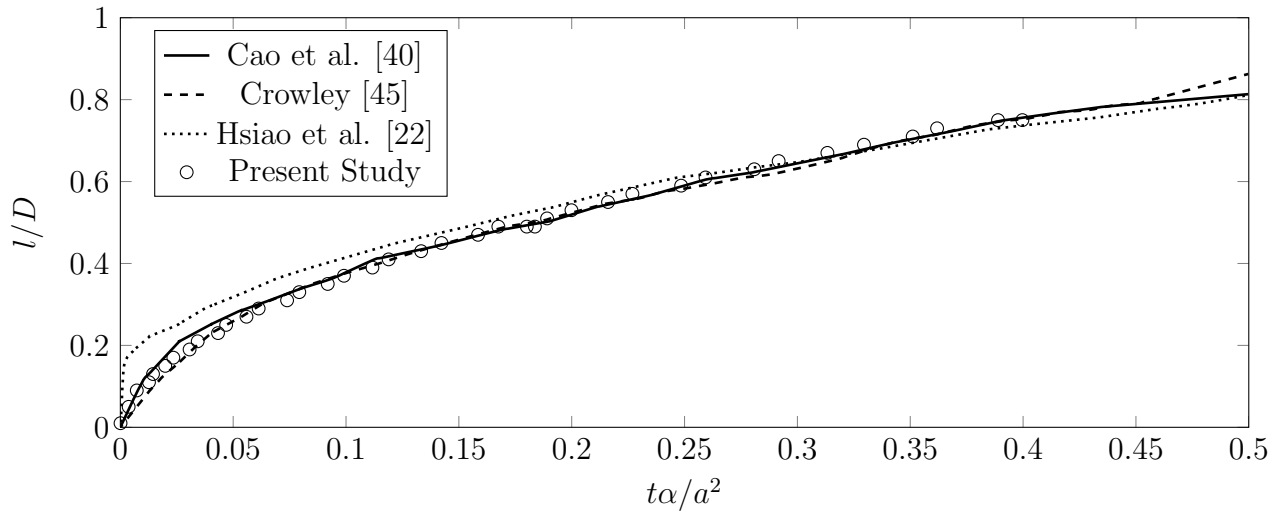


Figure 11: Solidification front moving along the diagonal of a cross section of the cuboid for saturated liquid (compared against Cao et al. [40], Crowley [45], and Hsiao et al. [22]).

The second problem has the same configuration as before with only the initial temperature being at a value larger than phase change temperature. Non-dimensional parameters for this problem are $\Theta = (T_i - T_w)/(T_m - T_w) = 9/7$ and $St = C_s(T_m - T_w)/L = 2$, $\alpha_l/\alpha_s = 0.9$, and $k_l/k_s = 0.9$. Figure 12 compares results for this test case against results of Cao et al. [40], Hsiao et al. [22], and Keung [46].

3.2.2 Effect of ΔT

The same test case has also been conducted using the same properties and the assumption that phase change occurs at a temperature range of $\Delta T = 20$. As evident, results are not sensitive to allowing the phase change to occur over a temperature range.

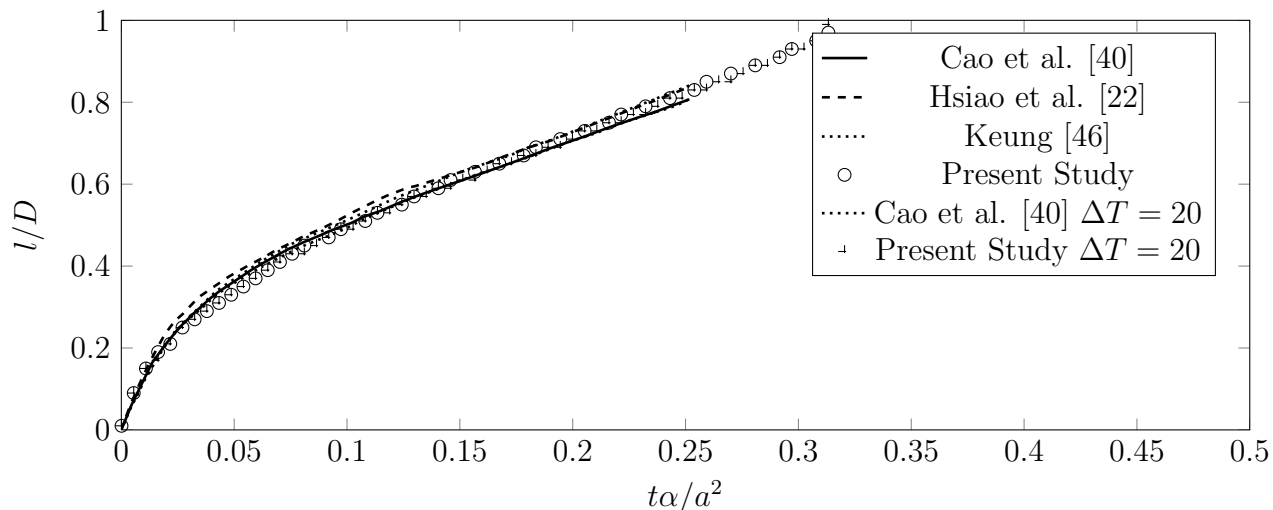


Figure 12: Solidification front moving along the diagonal of a cross section of the cuboid for liquid above freezing temperature (Cao et al. [40], Hsiao et al. [22], and Keung [46]).

3.2.3 Effect of particle resolution

To make sure solution is not dependent to the initial particle positioning (particle resolution), different resolutions has been chosen for problems above. Figure 13 shows variation of results as resolution is changed from 10×10 to 100×100 . It can be seen that by increasing the resolution, results converge to unique values. Results remain nearly identical for resolutions above these values.

3.2.4 Effect of Smoothing Kernel

Effect of choosing different smoothing functions has also been studied by choosing four common smoothing functions shown in table 3. First example from before has been repeated using each of these kernels. Figure 14 shows that the choice of smoothing kernel will not affect final results.

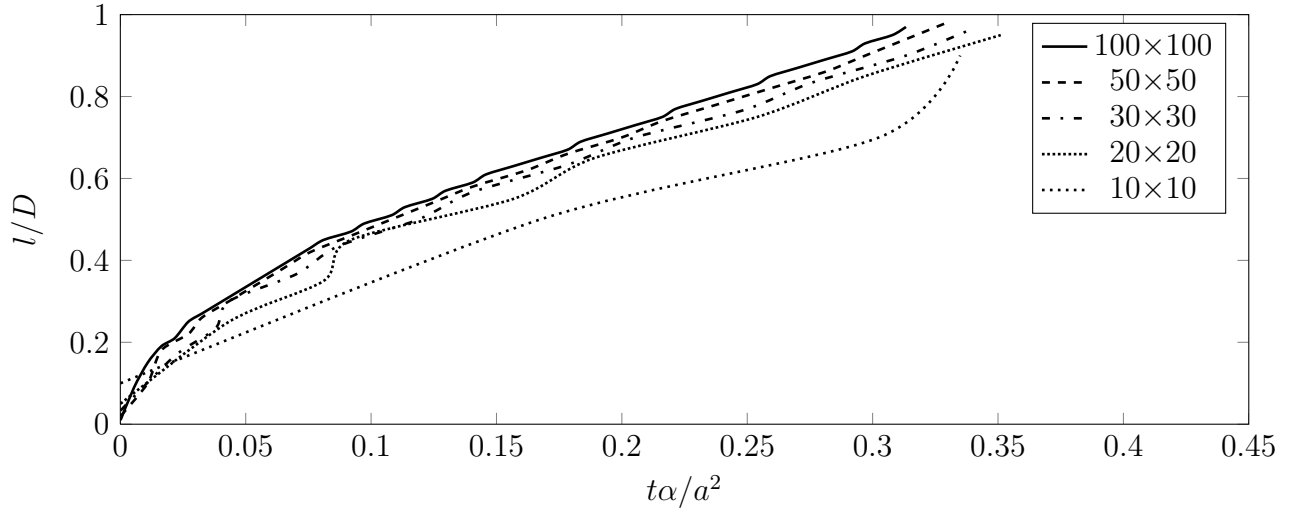


Figure 13: Mesh resolution dependency. Figure shows solidification front moving along the diagonal of a cross section of a cuboid (which has a size of 2 by 2). Mesh resolution on the cross section has been changed from 10×10 to 100×100 .

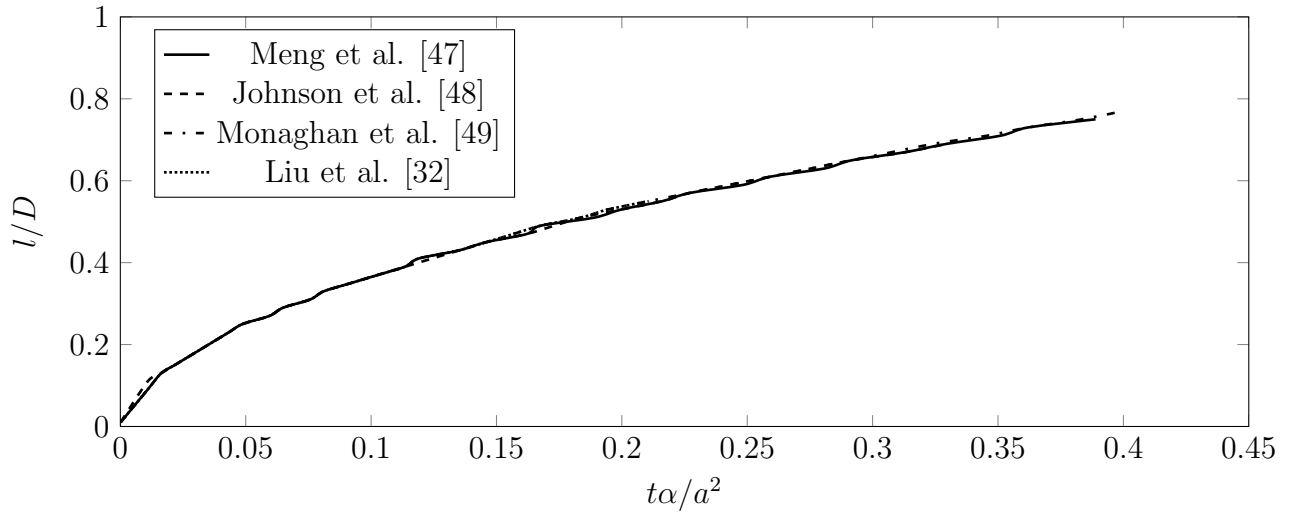


Figure 14: First example repeated using different kernels from table 3. Figure shows solidification front moving along the diagonal of a cross section of the cuboid for saturated liquid.

Table 3: Smoothing kernels used in Enthalpy Formulation test cases

Smoothing Kernels	
Meng et al. [47]	$W(R, h) = \frac{21}{16\pi h^3} \begin{cases} (1 - R/2)^4(2R + 1) & 0 \leq R \leq 2 \\ 0 & \textit{otherwise} \end{cases}$
Johnson et al. [48]	$W(R, h) = \frac{5}{4\pi h^3} \begin{cases} (3/16)R^2 - (3/4)R + 3/4 & 0 \leq R \leq 2 \\ 0 & \textit{otherwise} \end{cases}$
Monaghan et al. [49]	$W(R, h) = \frac{3}{2\pi h^3} \begin{cases} 2/3 - R^2 + R^3/2 & 0 \leq R < 1 \\ (1/6)(2 - R)^3 & 1 \leq R < 2 \\ 0 & \textit{otherwise} \end{cases}$
Liu et al. [32]	$W(R, h) = \frac{1}{4\pi h^3} \begin{cases} (2 - R)^3 - 4(1 - R)^3 & 0 \leq R \leq 1 \\ (2 - R)^3 & 1 < R \leq 2 \\ 0 & \textit{otherwise} \end{cases}$

3.3 Three-dimensional Problem: Droplet Impact & Solidification

The three-dimensional problem of interest here is impact and solidification of a molten drop. For comparison, test case conditions are chosen similar to test case of Aziz et al. [50] and Pasandideh et al. [51]. In this problem, a molten tin drop is impacted on a stainless steel substrate. The drop is initially at 240°C. The substrate is at room temperature. The impact is occurring at a low velocity of 1m/s. The drop has an initial diameter of 2.7mm. The spread factor (D/D_0) for this test case has been plotted in figure 15. Experimental results of Aziz et al. [50], and numerical result of Pasandideh et al. [51] have also been plotted here for comparison. Results indicate a good agreement to other numerical and experimental results for spread factor of the low velocity impacting drop. The final prediction for the spread factor here is closer to the numerical results of Pasandideh et al., both deviating near 6% from Aziz et al. experimental values.

3.4 Mushy zone

Providing an exact benchmark for the mushy implementation methods seems impossible for various reasons. There are not any robust and accurate empirical measurements of the mushy region available to match the framework of this work. For the numerical studies that have been dedicated to this matter, the typical problem that has been studied is natural convection. In this case, the material is allowed to solidify in a cube (or corner in 2D). During this process, the natural convection resulting from temperature variations will accelerate molten liquid to flow similar to a lid-driven cavity problem. This will result in an uneven growth of the solid front and can be used as a tool to measure the capability of mushy region handling. In the implementation in this work, however, the small time steps enforced on the simulation will make modeling of a natural convection cavity problem cumbersome. Therefore, instead

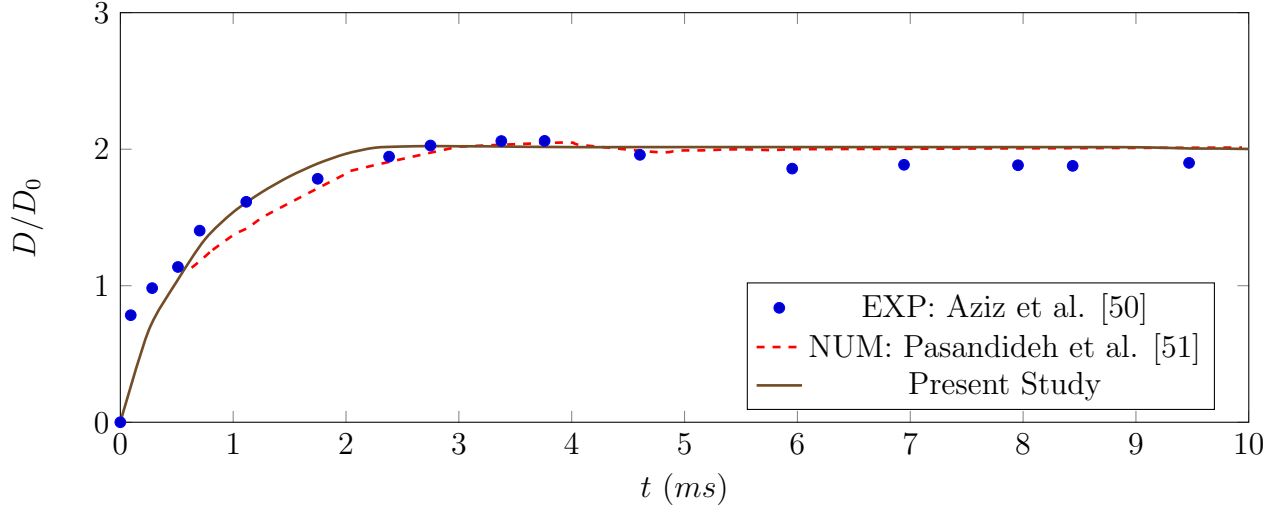


Figure 15: Spread factor (D/D_0) for a tin drop at 240°C with 2.7mm diameter impacting at 1m/s on a 25°C stainless steel substrate.

a more relaxed problem has been chosen here to provide a qualitative comparison of the formulations. In this problem, solidification problem in a cavity under natural convection is studied. However, in order to avoid long wait times for the flow pattern to form, a divergence free velocity field in the form of $v_\theta = 20\frac{r}{R}$ and $v_r = 0$ is imposed on the fluid at the start of the simulation. Figure 16 shows schematic drawing of this problem. Liquid phase here is confined inside a cavity. The lower and upper walls are isolated. The fluid is allowed to have heat transfer only with a cold and hot source on each side. The red arrows in this figure show the initial velocity field in the domain.

Particle positions for this test case after the solidification has been partially completed is shown in figure 17 at $t = 0.16$. The solidification front (for $\alpha = 0.5$) for equations 60 and 61 at this time has also been plotted in figure 18. It becomes evident that though both formulations used here provide similar results, the particle positions and arrangements are better preserved using 60. Hence, equation 60 has been used to capture mushy effects in the current study.

3.5 SPS Droplet Impact

3.5.1 Problem Specification

The developed phase change model is now applied to study impact and solidification of sub-micron molten ceramic droplets generated in Suspension Plasma Spraying. The plasma torch operating conditions are varied as shown in table 1 for cases A-E. From these test cases, sample particles have been chosen for closer examination of their impacts on the substrate. Analyzing impact points of molten droplets reveals that only a handful will have close impact points on the substrate in short time intervals. This comes from high efficiency of the SPS process in coating the surface, as the mist of particles generated from atomization of liquid suspension uniformly covers a large area, making it impossible to get multiple impacts on a

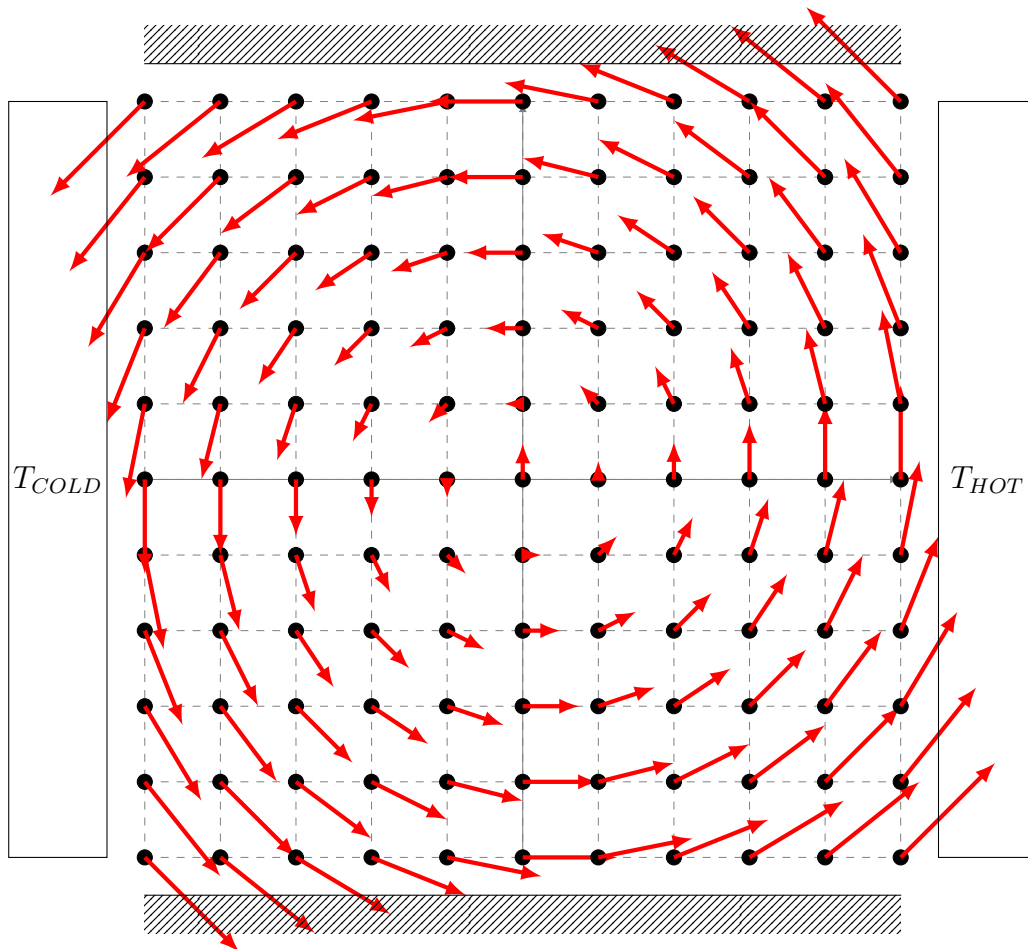


Figure 16: Divergence free initial velocity field for measuring effects of mushy region.

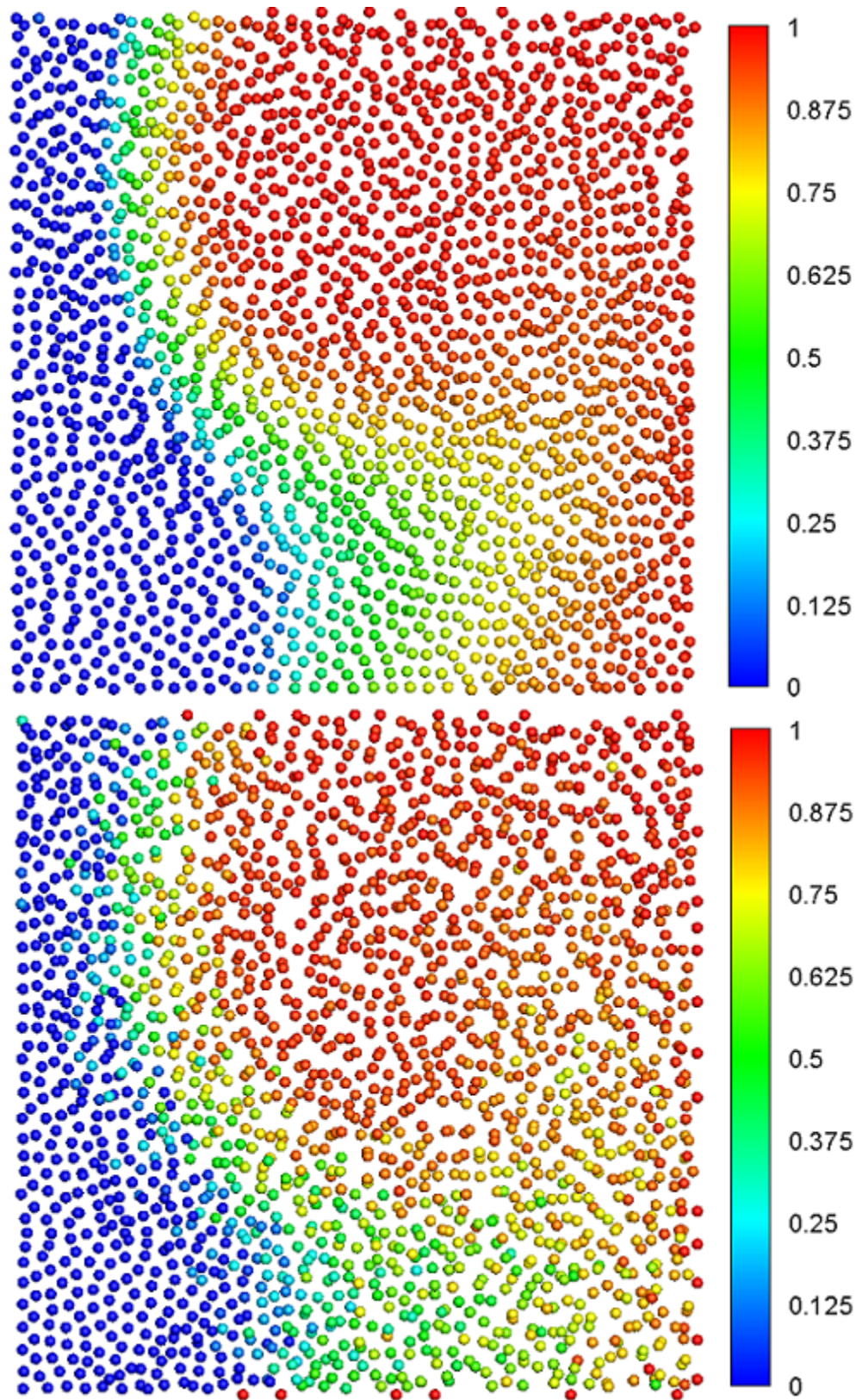


Figure 17: Particle positions in a 1×1 rectangle at $t = 0.16$ (s) colored by their liquid fractions. Mushy zone effected included using equation 60 (left) and equation 61 (right).

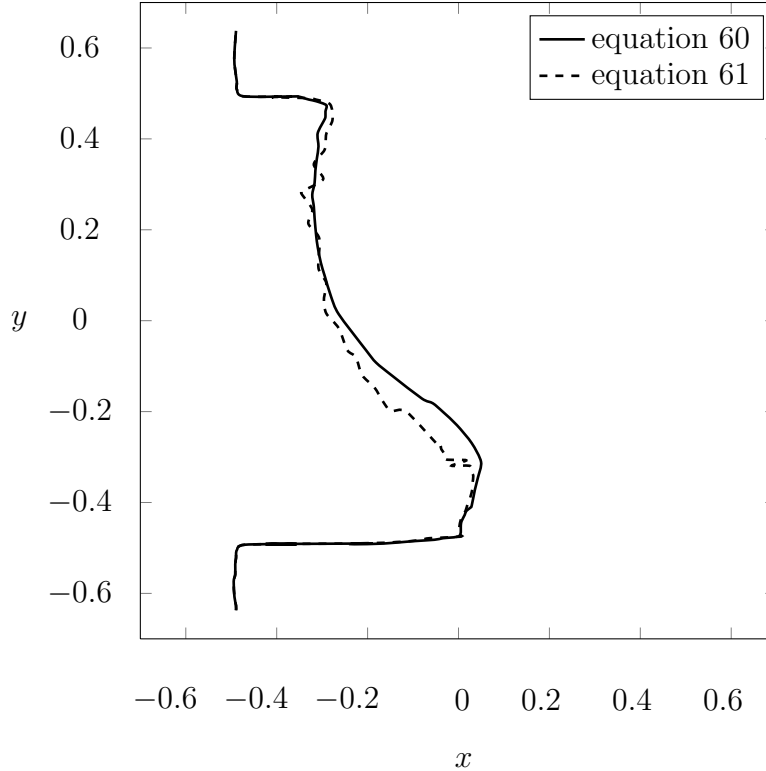


Figure 18: Solidification front (liquid fraction = 0.5) for equations 60 and 61 at $t = 0.16$.

particular place of the substrate in a short time interval. As an starting point here, a site on the substrate has been chosen for further study, where SPS data shows close impact of 5 particles (from case E, table 1). The impact points of these 5 particles are shown in figure 19. Although not all of these 5 particles have direct impacts, they will eventually overlap when their splats spread over the substrate. Properties of these particles at the time of impact are provided in table 4. As evident, droplets in this neighbourhood cover a wide range of possible diameters that are found during the SPS coating process.

Table 4: YSZ particles properties at impact

#	x (μm)	y (μm)	u (m/s)	v (m/s)	w (m/s)	T (K)	D (μm)
1	-6.6	3.0	-4.1	1.5	-207.6	3679.8	9.1
2	1.4	-2.9	-0.2	5.9	-226.1	3833.5	8.7
3	10.8	-9.3	27.7	5.1	-88.5	3523.5	3.0
4	4.7	5.7	15.3	16.1	-99.3	3543.3	2.9
5	-10.3	3.6	-8.1	35.3	-227.8	3638.2	4.2

In figure 19, the substrate is located in the $x - y$ plane. The z axis is perpendicular to the substrate and points towards the torch nozzle. Particles traveling to the substrate will have a negative velocity in the z direction. Velocity components parallel to the substrate, though small in magnitude, have also been included in this simulation. Sample simulation

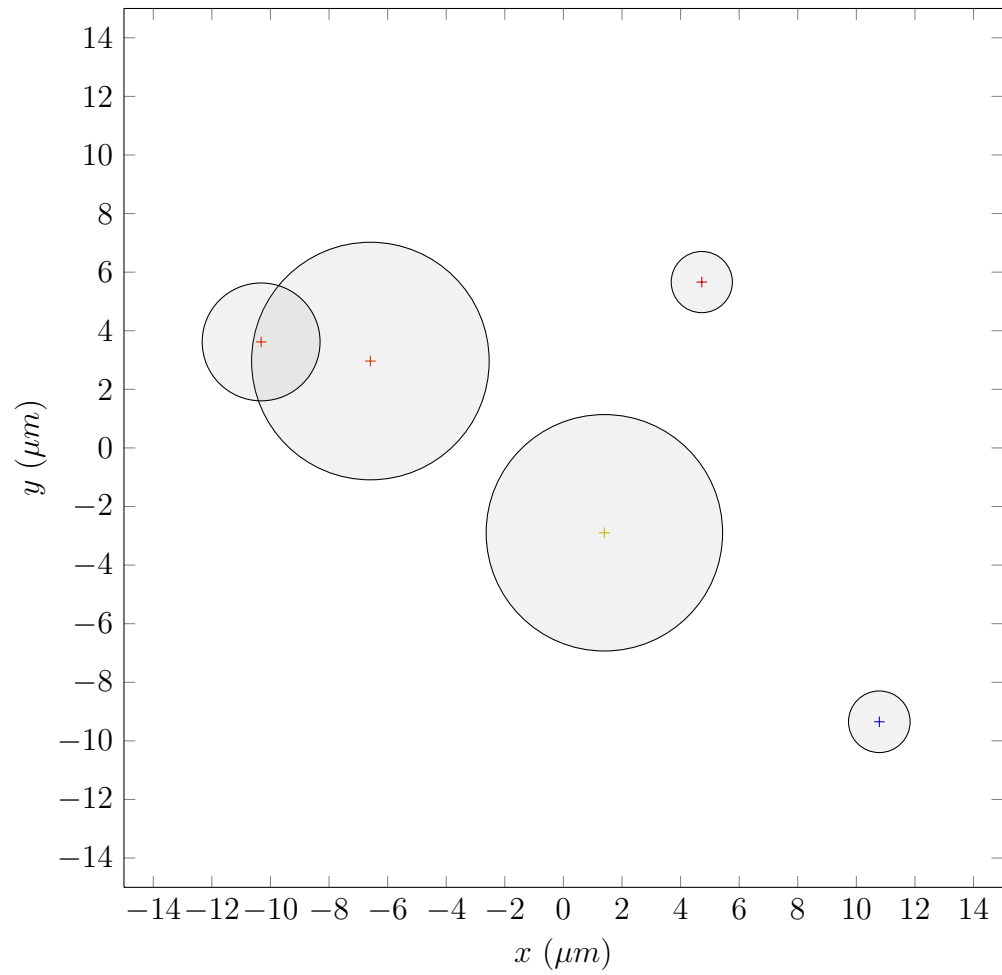


Figure 19: Position and diameter of five YSZ drops impacting the substrate obtained from case E (table 1).

cases show that the impact, spread and solidification of each particle happens orders of magnitude faster than the impact of the next particle. Hence, it is reasonable to assume that each particle is completely solidified before the next particle impacts close to it. For the simulations here, the material for the droplets and substrate is YSZ. Though at the start of the coating process, the substrate material will play an important role as typical metallic substrates will have higher thermal conductivities compared to YSZ, with more YSZ layers coating the surface over time, the new droplets will mostly impact a substrate covered by YSZ. The droplets are in molten liquid states corresponding to their values in table 4. The contact angle between drops and the surface is taken to be 90° [52], though as it will be discussed later, the capillary effects are negligible since $We \gg \sqrt{Re}$ here [53]. The solidification of molten drops is resolved using equation 49. The mushy zone effects are also included using equation 60. Gravity force is added with a value of $9.81m/s^2$ exerted on molten particles in the opposite direction of the z axis, although its effect is also not significant. As the impact velocities are high, it is important to apply a no-slip boundary condition on the substrate. Here, the efficient no-slip model of Holmes et al. [36] has been utilized which performs well on both flat and more complex wall geometries.

3.5.2 Multiple Splat Overlaps

Results are presented in figures 20-26. Figures have been colored by z magnitude at each point, identifying how the roughness of the substrate changes due to the increase in local height. Figures 20, 21, 23, and 24 show substrate after impact of droplets #1, #2, #3, and #4, respectively. The first two droplets have larger diameters near $9\mu m$ with impact velocities higher than $200m/s$. Hence, they have large spread factors and the splats cover a large area. The next two drops have smaller diameters near $3\mu m$ and lower impact velocities below $100m/s$. The last drop also has a small diameter, but impacts at the highest speed. The final coated substrate after five impacts is plotted in figures 25 and 26. The maximum height from substrate's surface for each solidified droplet is 0.91, 1.76, 1.53, 2.40, and 2.14 μm , for droplets #1 to #5, respectively. Hence, the highest peak in the finished coating corresponds to a height of $2.40\mu m$, which is achieved from overlapping splats of droplets #1, #2, and #4.

3.5.3 Spread Factor

As impact points of YSZ particles generated by suspension plasma spraying are well-spread on the substrate, the larger size droplets make the main contribution in creating roughness, by having splats that overlap one another. Smaller size particles mostly create isolated bumps, as the possibility of having direct binary impacts in short time periods is low, and because the spread factor for these smaller droplets is not relatively large. Table 5 shows some statistical information on YSZ particles in case E. For different particle diameter ranges, the number of YSZ droplets, the average impact velocities, and the average distance between the impact sites and the center of all impacts (\bar{r}) have been reported in this table. Here, r is defined as $\sqrt{(x - x_{mean})^2 + (y - y_{mean})^2}$. x_{mean} and y_{mean} mark the mean center for all the impacts. While the torch is located and is pointing to $(0, 0)$, since the injection is done with an angle, the particles will not impact near the $(0, 0)$ point and will be shifted to the

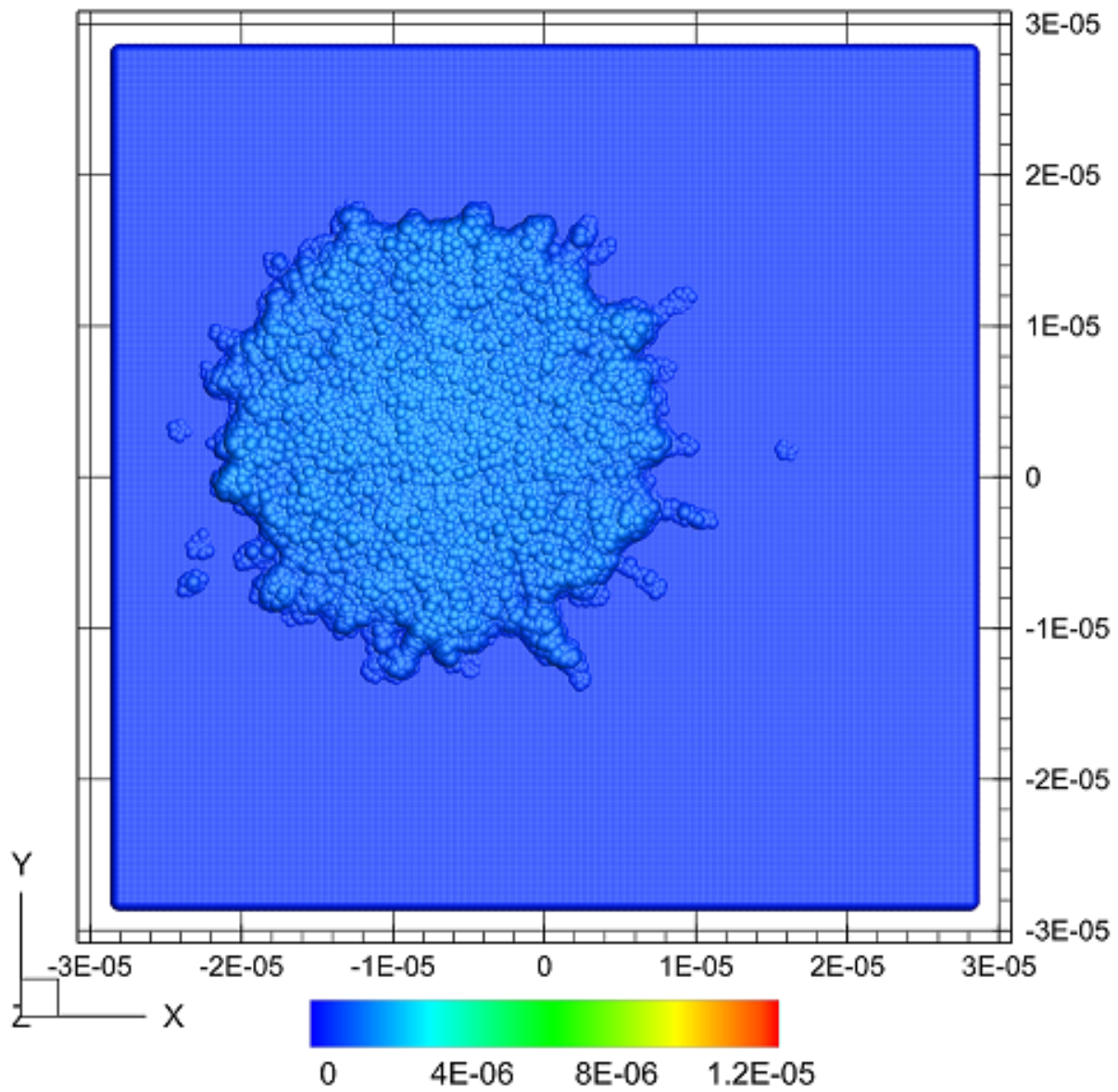


Figure 20: Solidification of droplet #1 on the substrate (table 4) colored by the height from the substrate.

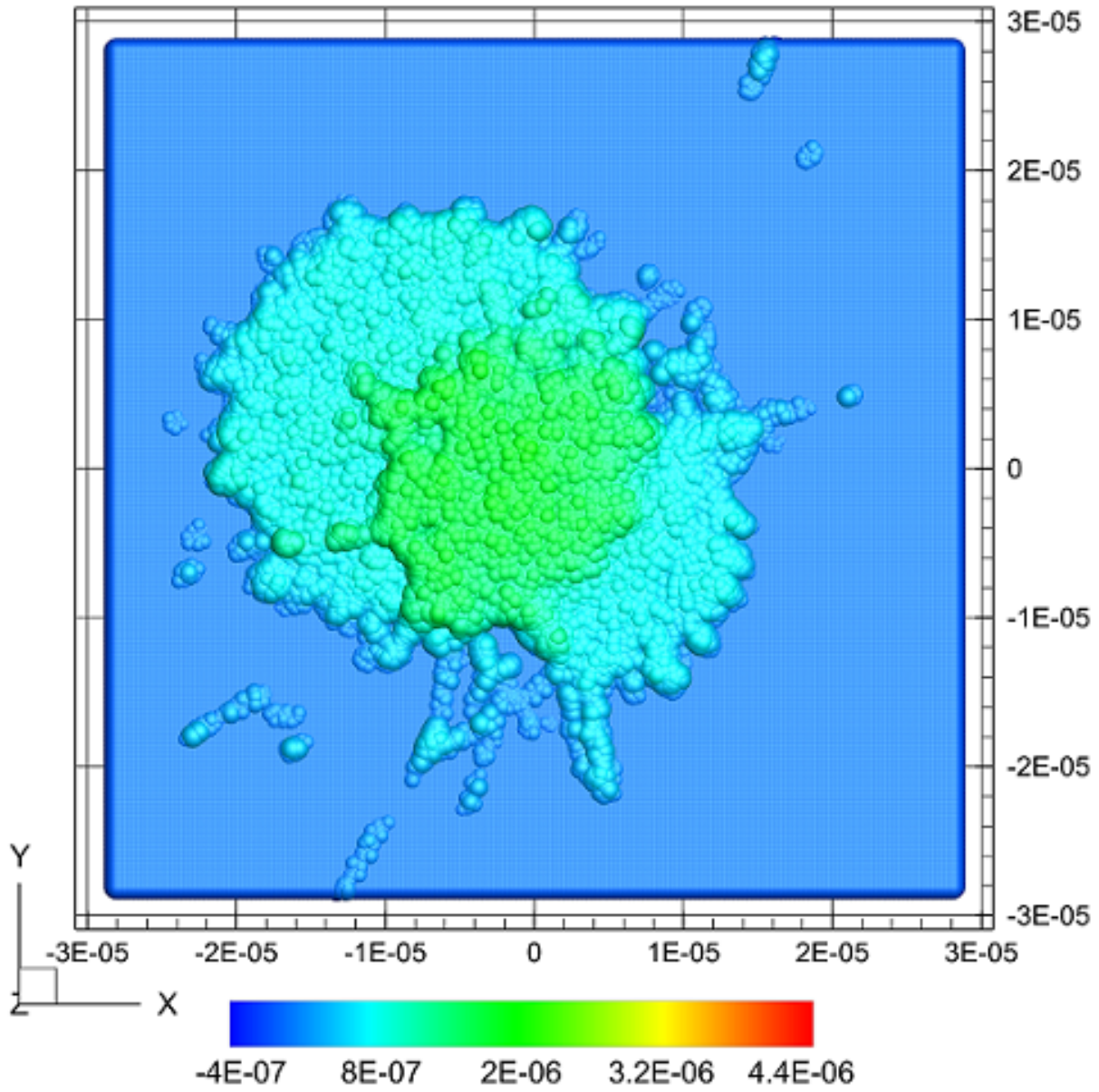


Figure 21: Solidification of droplet #2 on the substrate (table 4) colored by the height from the substrate.

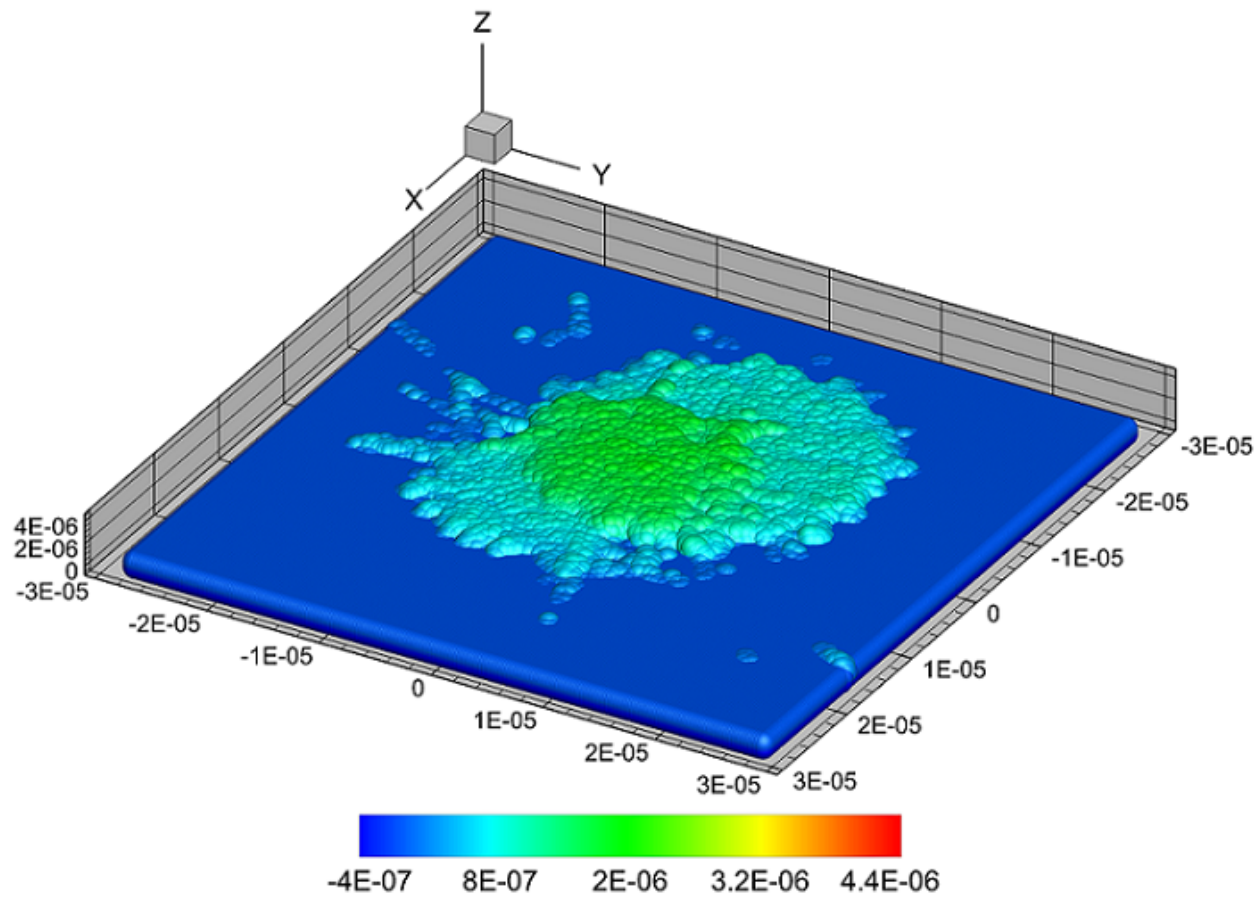


Figure 22: Solidification of droplet #2 on the substrate (table 4) colored by the height from the substrate.

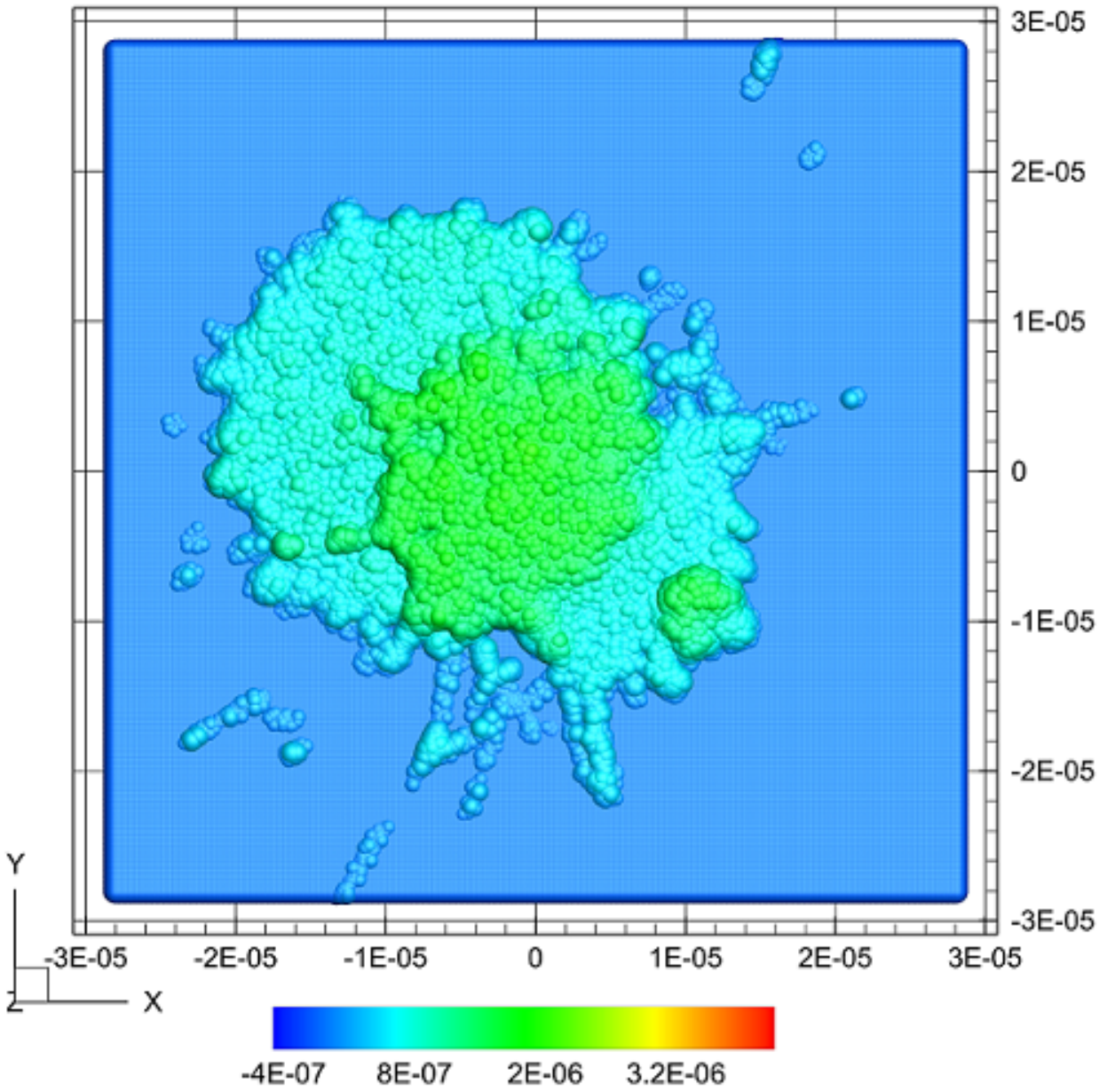


Figure 23: Solidification of droplet #3 on the substrate (table 4) colored by the height from the substrate.

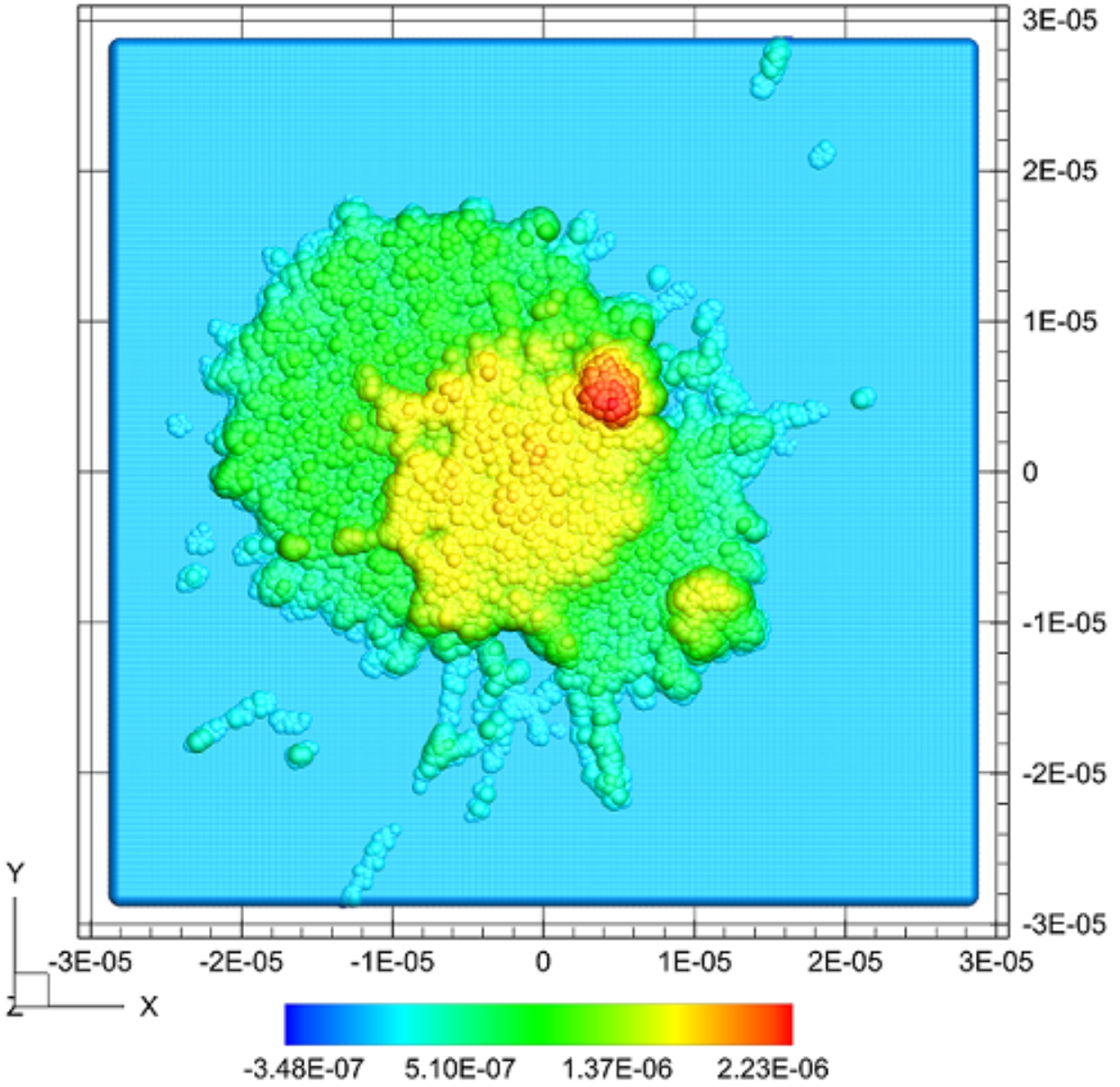


Figure 24: Solidification of droplet #4 on the substrate (table 4) colored by the height from the substrate.

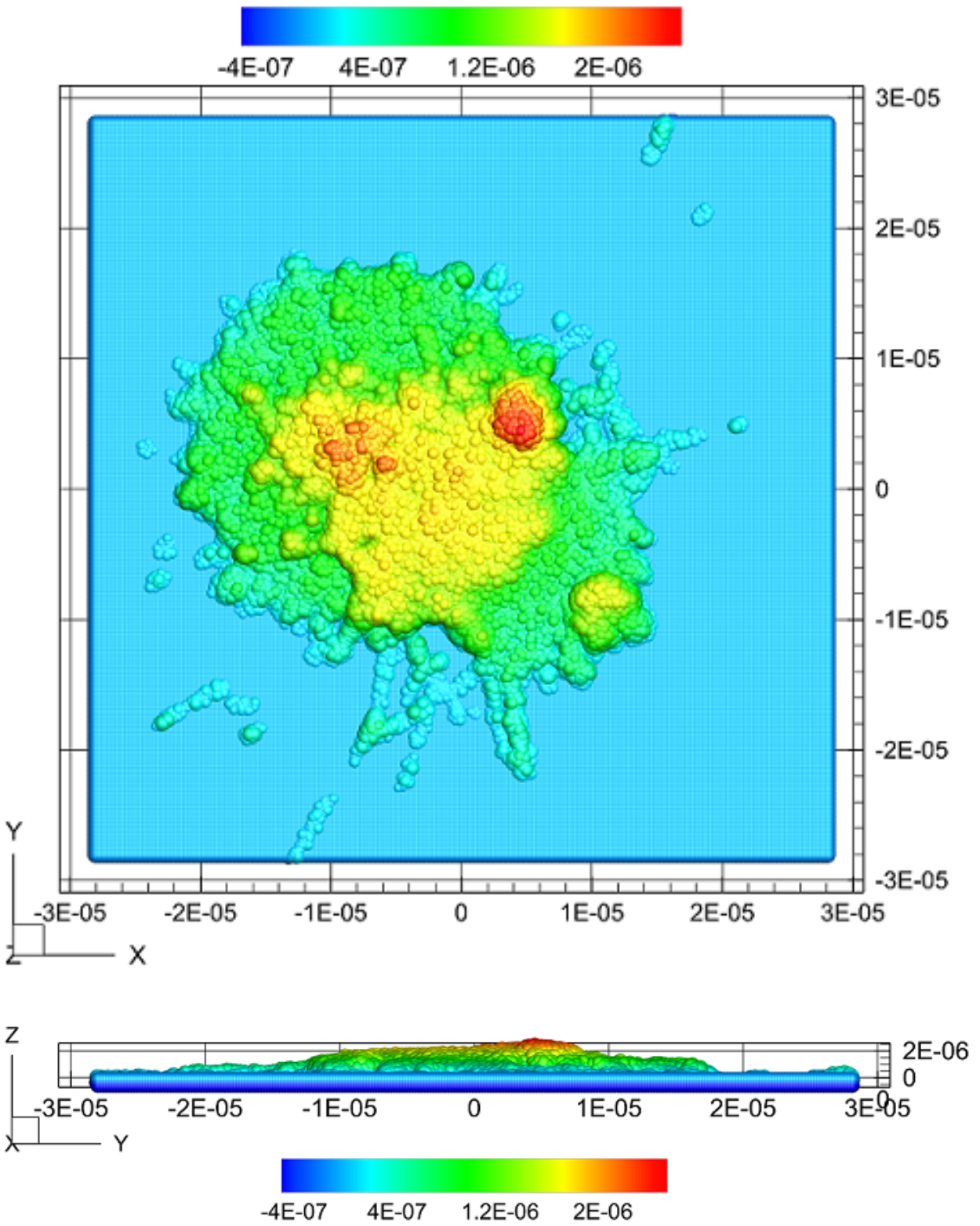


Figure 25: Solidification of five drops on the substrate (table 4) colored by the height from the substrate.

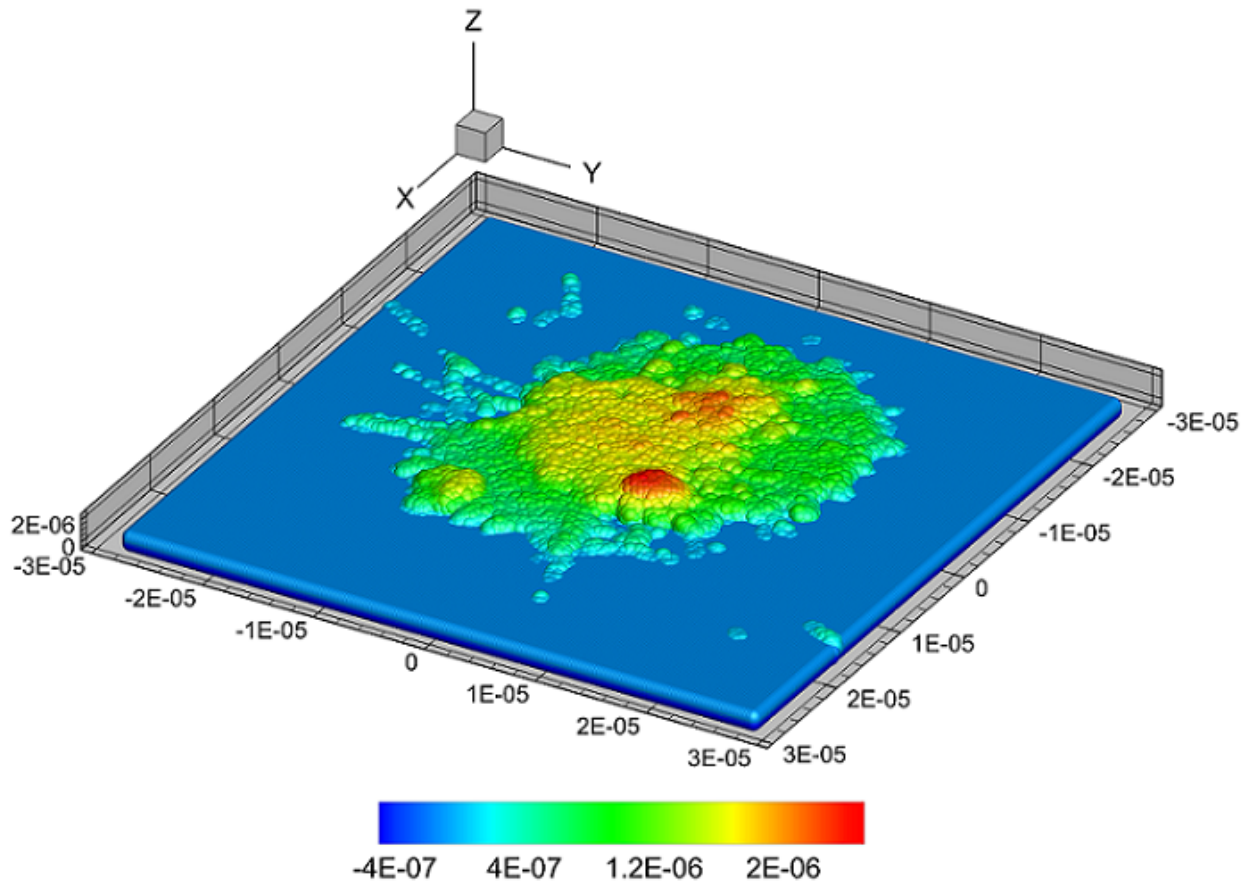


Figure 26: Solidification of five drops on the substrate (table 4) colored by the height from the substrate.

direction imposed by injection angle.

It is evident that small size ranges below $3 \mu m$ exhibit smaller impact velocities (smaller \bar{w}). These droplets are also falling further from the center of the substrate (larger \bar{r}). Larger YSZ droplets, on the other hand, have filled an area with diameter of $10mm$, potentially influenced by the torch nozzle diameter which is $7mm$. Combining findings from impact studies with the statistics here, it can be estimated that during this spray time, the substrate would possess a rougher finish inside the $10mm$ circle, which results from large particles imparting and generating overlapping of splats. The overlap of the two large particles in the test case conducted here (particles #1 and #2 in table 4) generated a height of $1.76\mu m$. The SPH simulation of drop #1 impact shows a spread factor (D/D_0) of 3.

Table 5: Average impact velocity (\bar{w}) and distance from substrate center (\bar{r}) for different diameter ranges in case E (table 1).

$D (\mu m)$	count (%)	$\bar{w} (m/s)$	$\bar{r} (mm)$	$\max(r) (mm)$	$\min(r) (mm)$	$\bar{T} (K)$
1-2	1	43	10.46	35.66	1.38	3142
2-3	7	80	7.73	37.56	0.10	3330
3-4	13	131	5.84	31.27	0.25	3468
4-5	16	169	5.75	39.41	0.09	3522
5-6	17	197	5.37	21.59	0.11	3591
6-7	16	211	5.33	30.39	0.13	3656
7-8	12	213	5.31	16.34	0.10	3690
8-9	8	199	5.64	15.14	0.31	3673
9-10	7	194	5.33	15.66	0.29	3717
10-11	3	179	5.49	12.55	0.39	3685
11-12	1	204	5.53	8.54	2.30	3905

Scatterness of particles on the substrate has been shown in figures 27 and 28 for different particle diameters. Results show for particle sizes between 1 to $3\mu m$ the particles cover a larger area on the substrate with a radius near 3.5 to $4cm$. Particles get closer to the center as the sizes grow higher.

To get a better prediction on the final conditions of the substrate, the SPH solver has been used here to calculate spread factor at three different velocities of 50, 100, and $200m/s$, which covers the velocity range of YSZ droplets impacting the substrate obtained from SPS simulation. Results of this test case are plotted in figure 29 as a function of the non-dimensional time ($t^* = tV/D_0$). These configurations leads to non-dimensional values of 96, 192, 383 for $Re = \frac{\rho V_0 D_0}{\mu}$, and 323, 1293, 5172 for $We = \frac{\rho V_0^2 D_0}{\sigma}$. Since Weber numbers here are much larger compared to Reynolds values, i.e. $We \gg \sqrt{Re}$, the capillary effects can be neglected [53]. Pasandideh-Fard et al. [53] have predicted that for these conditions and with $We \gg 12$, spread factor can be approximated by $0.5Re^{0.25}$. Results obtained here also suggest a similar correlation for spread factor in the form of ($R^2 = 0.9960$)

$$\xi_{max} = \frac{D_{max}}{D_0} = 0.59 Re^{0.28} \quad (63)$$

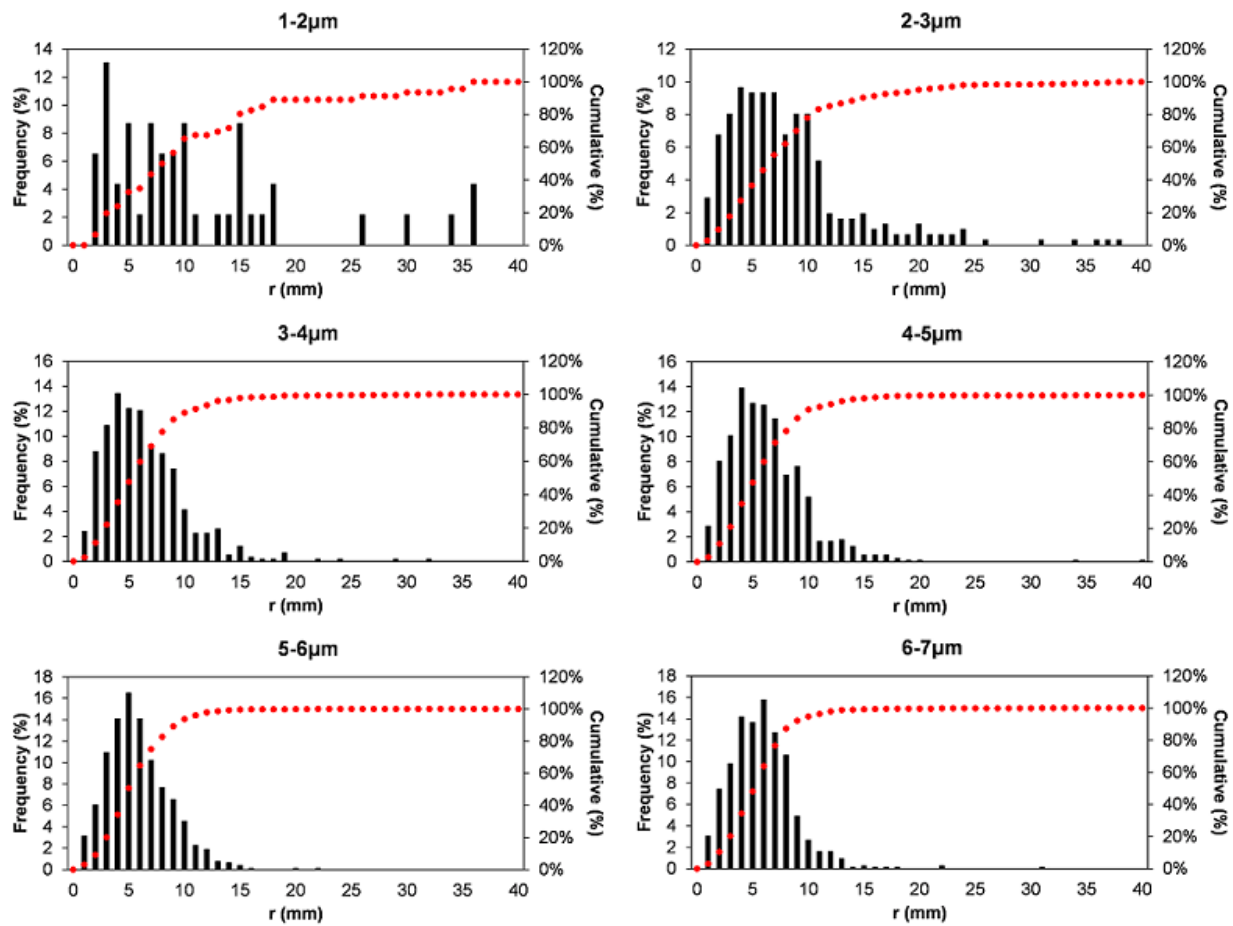


Figure 27: Distribution of impact position classified based on particle diameter.

Table 6: An estimate of the number of splat overlaps after impact on the substrate.

# overlaps	count (%)
0	59.61
1	22.19
2	9.99
3	4.61
4	2.04
5	0.95
6	0.35
7	0.17
8	0.06
9	0.03
10	0.01
11	0.00

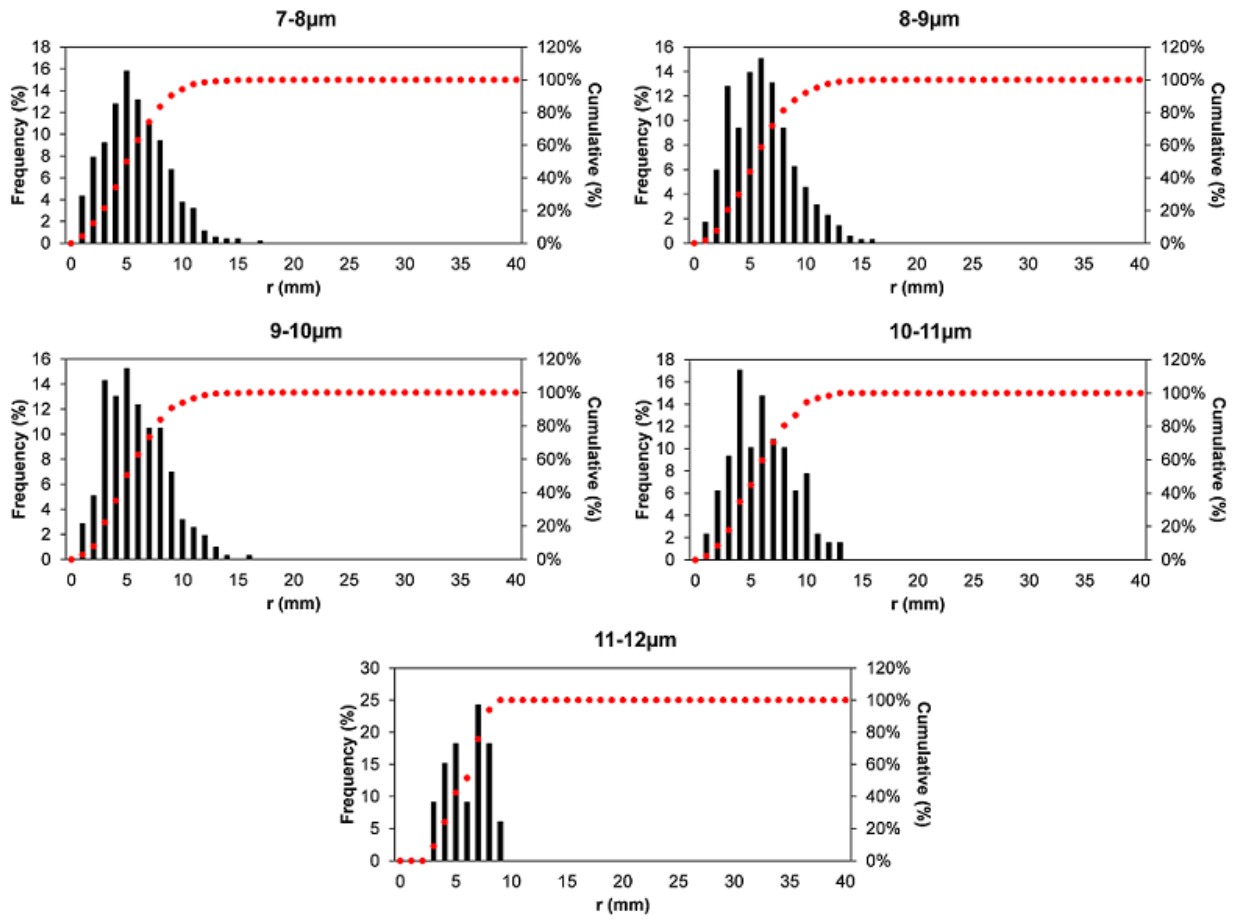


Figure 28: Distribution of impact position classified based on particle diameter.

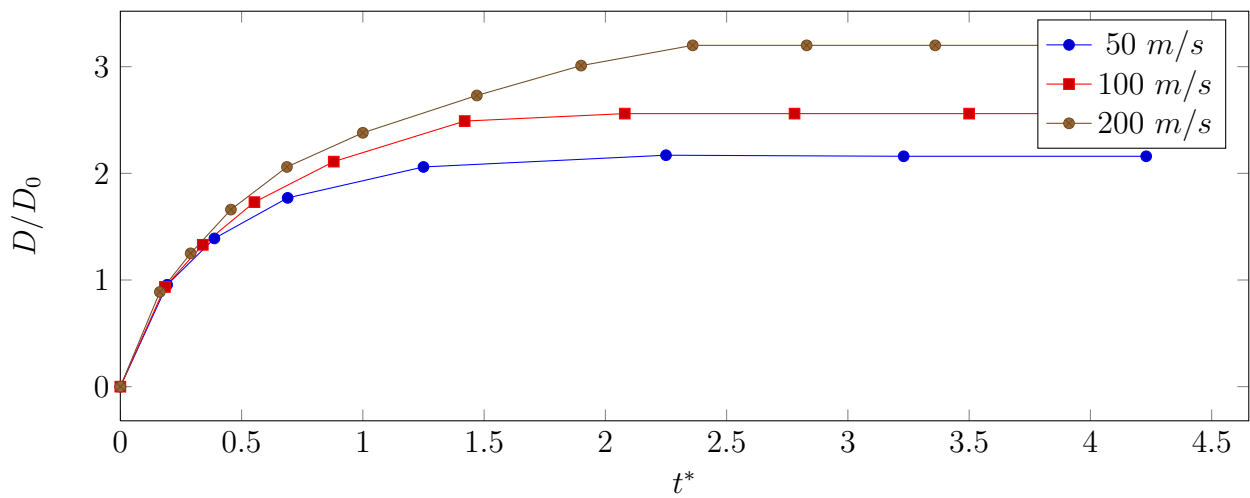


Figure 29: Spread factor (D/D_0) for a YSZ droplet impacting the substrate at 50, 100, and 200 m/s ($t^* = tV/D_0$).

3.5.4 Solidification Time and Heat Flux

A test case is conducted here to examine the solidification time and amount of heat transferred from an individual molten YSZ droplet to the substrate. A droplet with diameter of $3\mu m$ impacts the substrate at $3000K$ and velocity of $150m/s$. The substrate is at $600K$. The substrate is chosen from two different materials. The first is YSZ, identical to the material inside the droplets. For the second, thermal conductivity of the substrate is chosen to be $66W/(m \cdot K)$ (similar to Tin), mimicking initial layer of coating where droplets hit a metallic substrate. Figure 30 shows this droplet at various stages of impact and solidification at non-dimensional times of $t^* = 0.5, 10, 500, 1000, 1400,$ and 1500 on the YSZ substrate. Solidification starts from lower parts of the splat, and grows faster near the splat edges and in the middle, potentially due to lower thicknesses and longer contact time with the substrate, respectively. The splat fully solidifies here by nearly $t^* = 1500$.

Figure 31 shows the amount of heat flux at the impact point of the droplet on the substrate with higher thermal conductivity as a function of non-dimensional time. Results show that moments after impact, the heat transfer to the substrate grows suddenly to a very large value. The reason behind this sudden jump is that at the moment of impact, the substrate and droplet are at their highest temperature difference. Moreover, the impact area between these two is at its smallest near the impact time. As the droplet hits the surface and expands, the area underneath grows and distribute the heat transfer underneath the droplet. As the droplet spreads and loses heat, the temperature difference between the substrate and droplet becomes smaller causing a decrease in heat flux values. The high thermal conductivity of the substrate here contributes to a fast formation of a solidified layer next to the boundary. The cooling process of the material in the bulk of splat is still limited by the low thermal conductivity of the YSZ.

Another case of importance comes from examination of YSZ droplets obtained from SPS data. Results indicate that many of the binary impacts of splats occurring on the substrate involve $4 - 6\mu m$ droplets. This is due to the fact that these droplets are large enough to create big splats that can effectively contribute to overlaps and surface coverage. In this manner, a test is performed here for impact of a candidate droplet from SPS data with a diameter of $4.59\mu m$ impacting the substrate at $175m/s$ with a temperature of $3517K$. The solidified splat for this case is shown in figure 32. The impact and spread of this drop on the substrate is finished by nearly $t^* = 110$. It then takes up to $t^* = 1500$ for the splat to fully solidify.

From the binary impacts involving the droplet shown in figure 32, a common sample is chosen as an example here, where the splat generated by the droplet mentioned before with diameter of $4.59\mu m$ is impacted by a droplet with diameter of $6.8\mu m$ at a velocity of $231m/s$ and temperature of $3795K$. The point of impact for this droplet is nearly $14\mu m$ away from the center of impact of the first droplet. Result of this binary impact is shown in figure 33. As the time between the two impacts is much longer than the solidification time, it is safe to assume that the first droplet's splat has already solidified by the time the second droplet impacts. It can be observed that the second droplet becomes more spread in the free directions where there were no obstacles, in contrast to the direction where the splat from first droplet is present. In that direction, the second splat has spread into three main branches, two bypassing the first droplet's solidified splat, and one being forced to splash

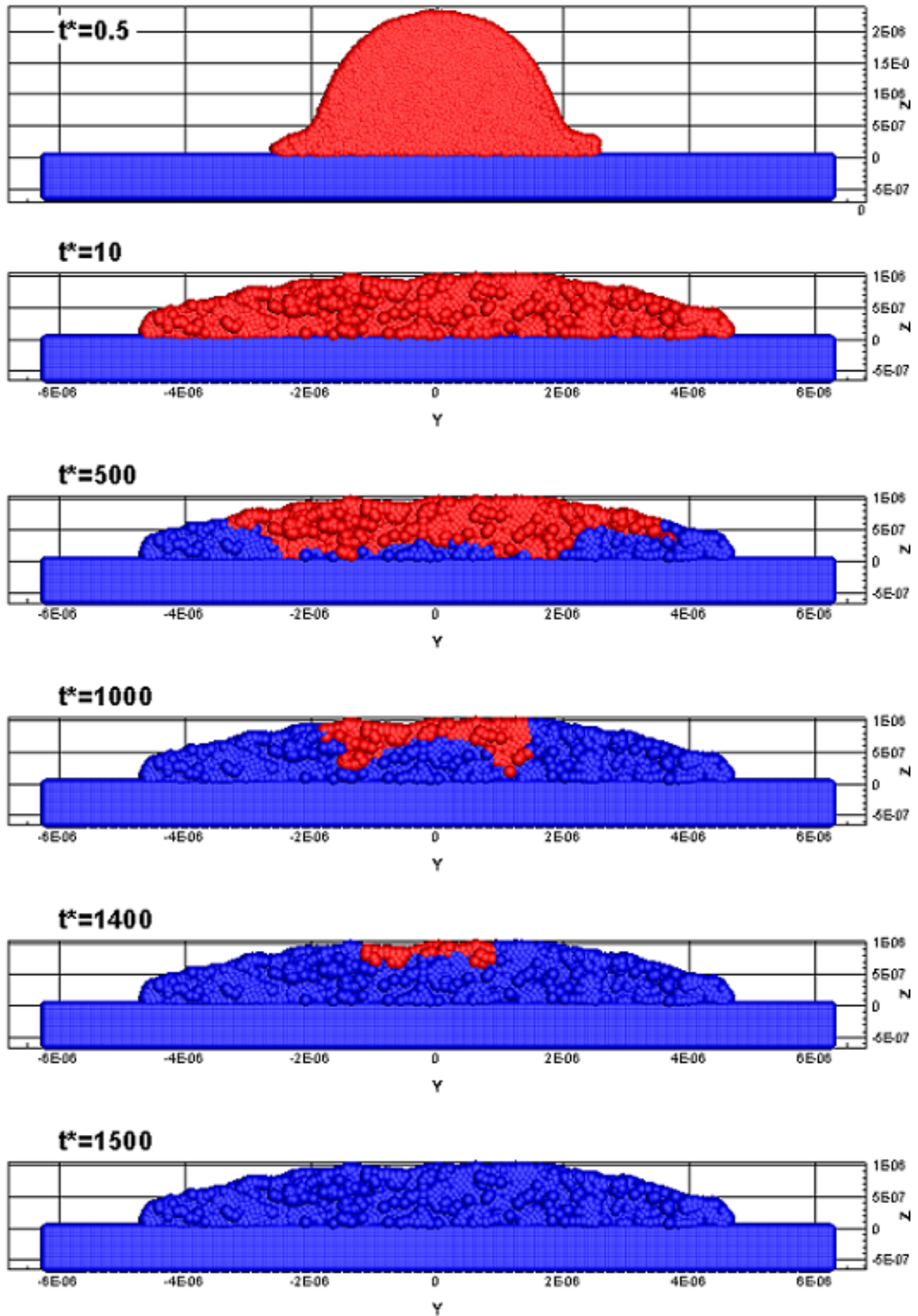


Figure 30: Impact and solidification time for a droplet at temperature of $3000K$ with radius of $3\mu m$ and velocity of $150m/s$.

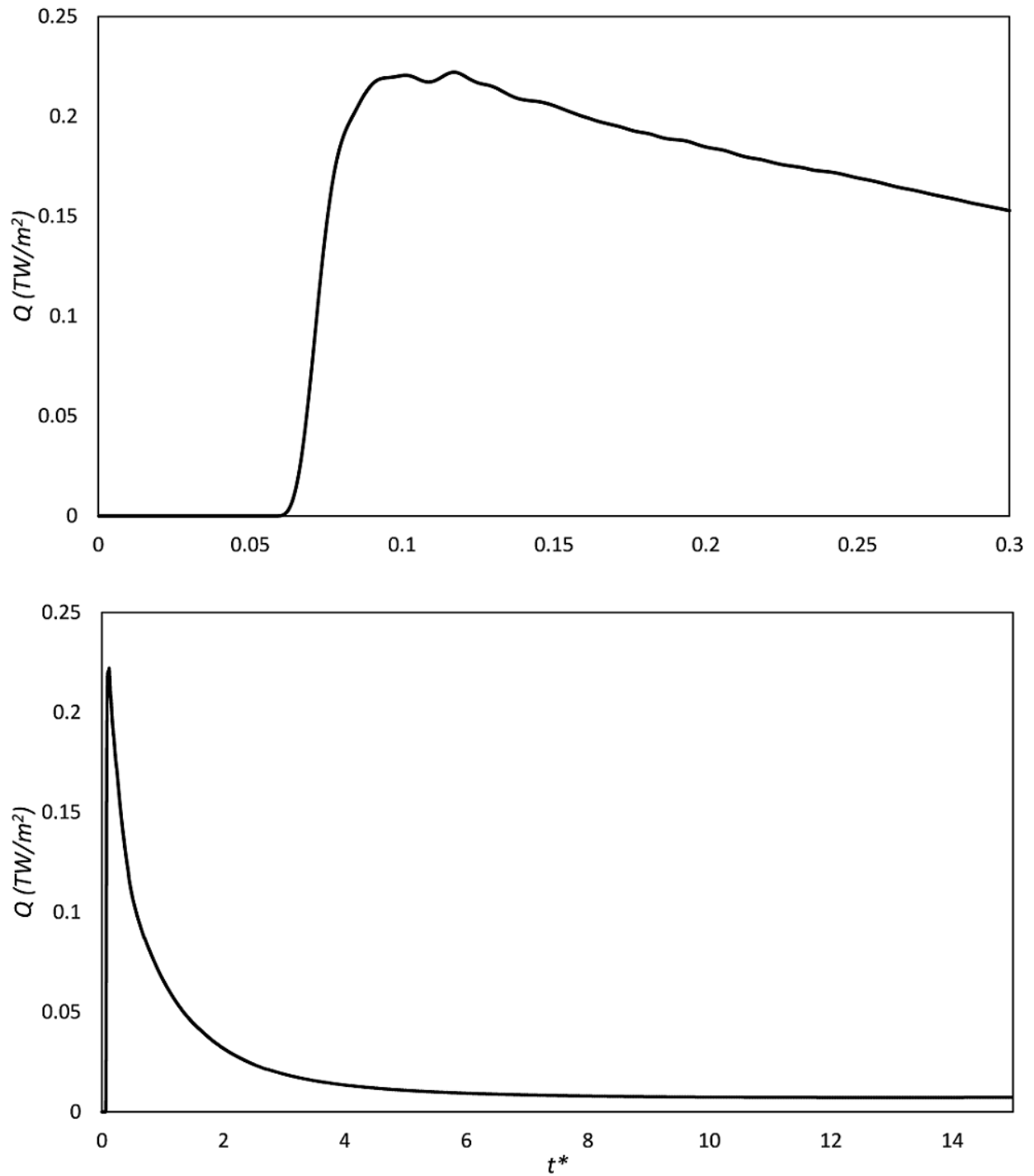


Figure 31: Heat flux at the impact point of the droplet on the substrate as a function of non-dimensional time ($t^* = tV/D_0$), shown near the time of impact (figure on top) and afterwards (figure on bottom).

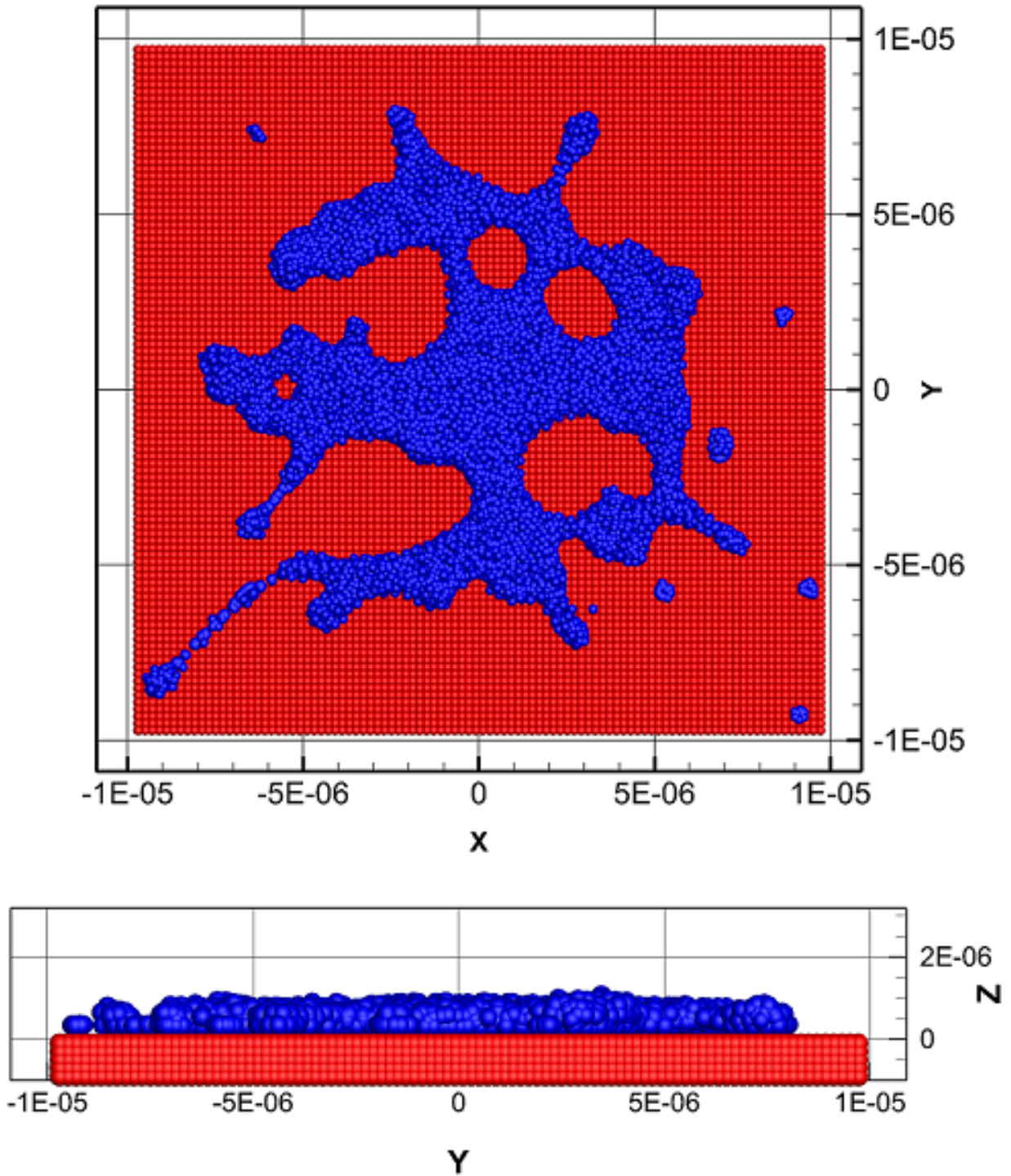


Figure 32: Solidified splot from a droplet with $4.59\mu m$ diameter, impacting the substrate at $175ms/$ with a temperature of $3517K$, shown at $t^* = 1500$.

over it.

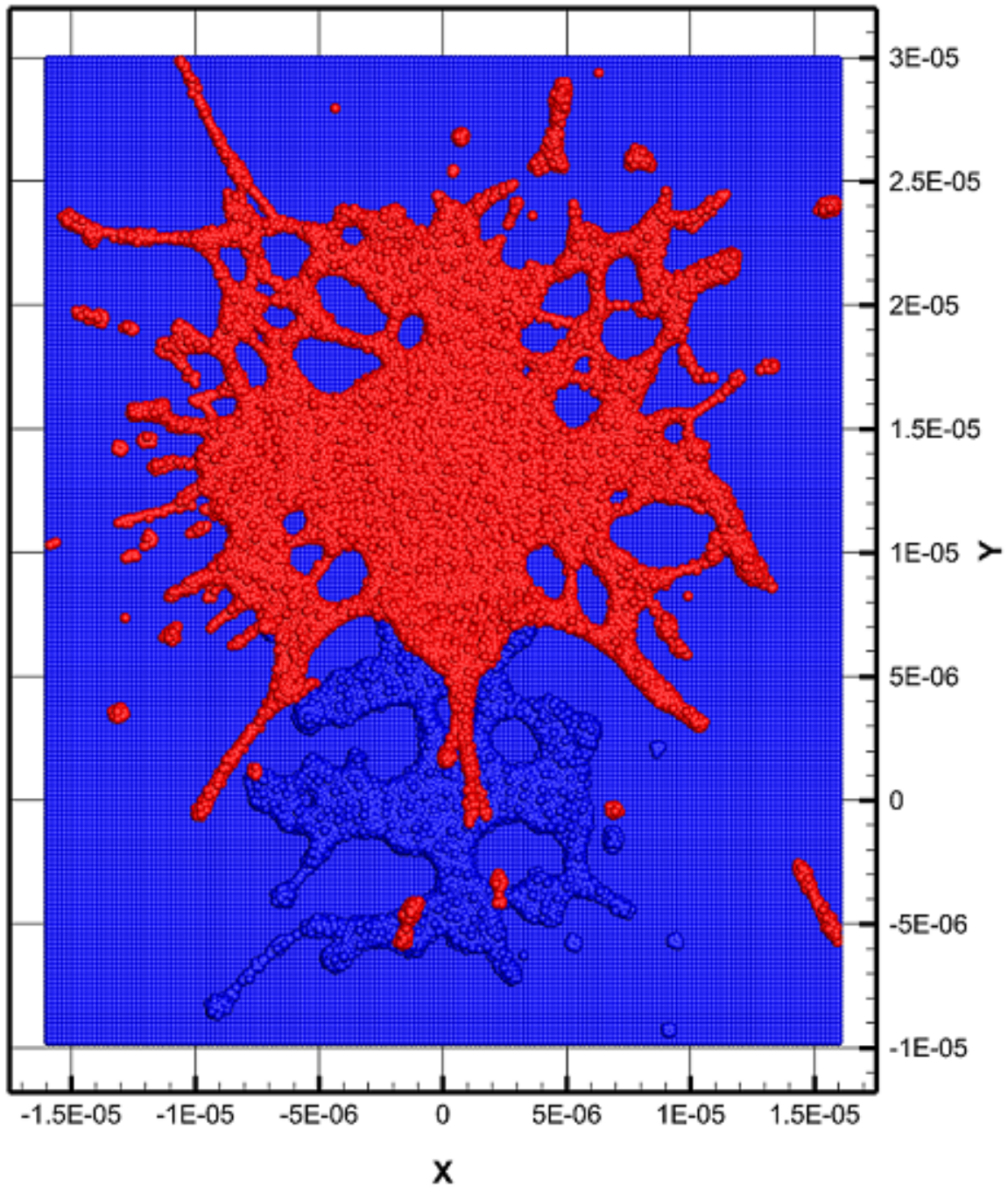


Figure 33: Binary impact of two droplets with diameters of 4.59 and $6.8\mu m$ at velocities of 175 and $231m/s$ and temperature of 3517 and $3795K$. The position of impact is offset by $14\mu m$.

3.5.5 Predictions for Finished Coating

Equation 63 is now used in a Matlab subroutine to examine the droplets collected on the substrate from SPS results. Having an approximation for spread of each droplet upon impact allows us to calculate the number of splats that will overlap in forming the final coated substrate. Results obtained are shown in table 6. It can be seen that near 22% of the total droplets hitting the substrate will generate splats with binary overlaps. In addition, 10%, 5%, and 2% will have two, three, and four splat overlappings, respectively. The rest of overlaps start to fall below 1% of the total droplets. The maximum number of overlaps is 12 with only 3 occurrences here. Overall, the finished coating of the substrate will be dominated by 60% isolated impacts and 22% binary-overlapped impacts. Finally another subject of interest is efficiency calculation for the total spray process. For this calculation, the total area of the substrate that is covered by solidified splats is needed. Using the correlation derived here for the final splat sizes (equation 63), the total covered area can be calculated. Overlaps of different splats however needs to be subtracted from calculated area. As multiple overlaps are occurring here, the calculation is conducted in another manner. The substrate surface is meshed in fine resolution. The summation of the areas of those cells that fall under at least one splat will result in the total area of substrate that has been covered. The resolution of this mesh has been increased till no noticeable variation in calculated area is observed. Resulted total area of the substrate that has been successfully coated is 80.57 mm^2 . The total area of this part of the substrate has also a value of 4975 mm^2 .

By applying the information gathered so far to cases A to E, effects of different parameters of the plasma torch on the finished surface can be studied. Taking droplets' spread according to equation 63 and assuming no pore formations occurring between the splats, the final coated surface for cases A to E can be predicted as shown in figure 34. The results show that after coating, the highest points from the substrate' surface are 4.28, 1.07, 2.44, 5.28, and $1.65 \mu\text{m}$ for cases A to E, respectively.

It has to be noted that by considering the temperature particles and omitting droplets that have not fully melted, the substrate will be clear for cases A, B, and C. These are droplets that have not received enough energy from the torch to finished their evaporation and melting cycles completely. Under this condition, the substrate for cases D and E is shown in figure 35. The maximum height of the coating on the substrate is 2.14 and $1.65 \mu\text{m}$ for cases D and E, respectively. The coating does not change significantly for case E, as most of the particles under these torch conditions reach the substrate being fully molten. Results for case E show that the points on the positive side of the x axis have higher heights compared to the left side. This is due to the injection angle for the suspension stream, which points from positive x values towards negative values (right to left).

3.5.6 Pore Formation

A two-dimensional setup has been used here to study the cases where droplet impacts are prone to void formation. For the test cases below, a droplet with a radius of $3 \mu\text{m}$ is impacted on a surface. The surface geometry is changed going from a flat surface to surfaces with step sizes of 0.12, 0.24, 0.36, $0.54 \mu\text{m}$. Impact velocity is 150 m/s for all the cases. Initial temperature of the substrate is 300 K . All figures have been reported at $t = 0.1 \mu\text{s}$, which is

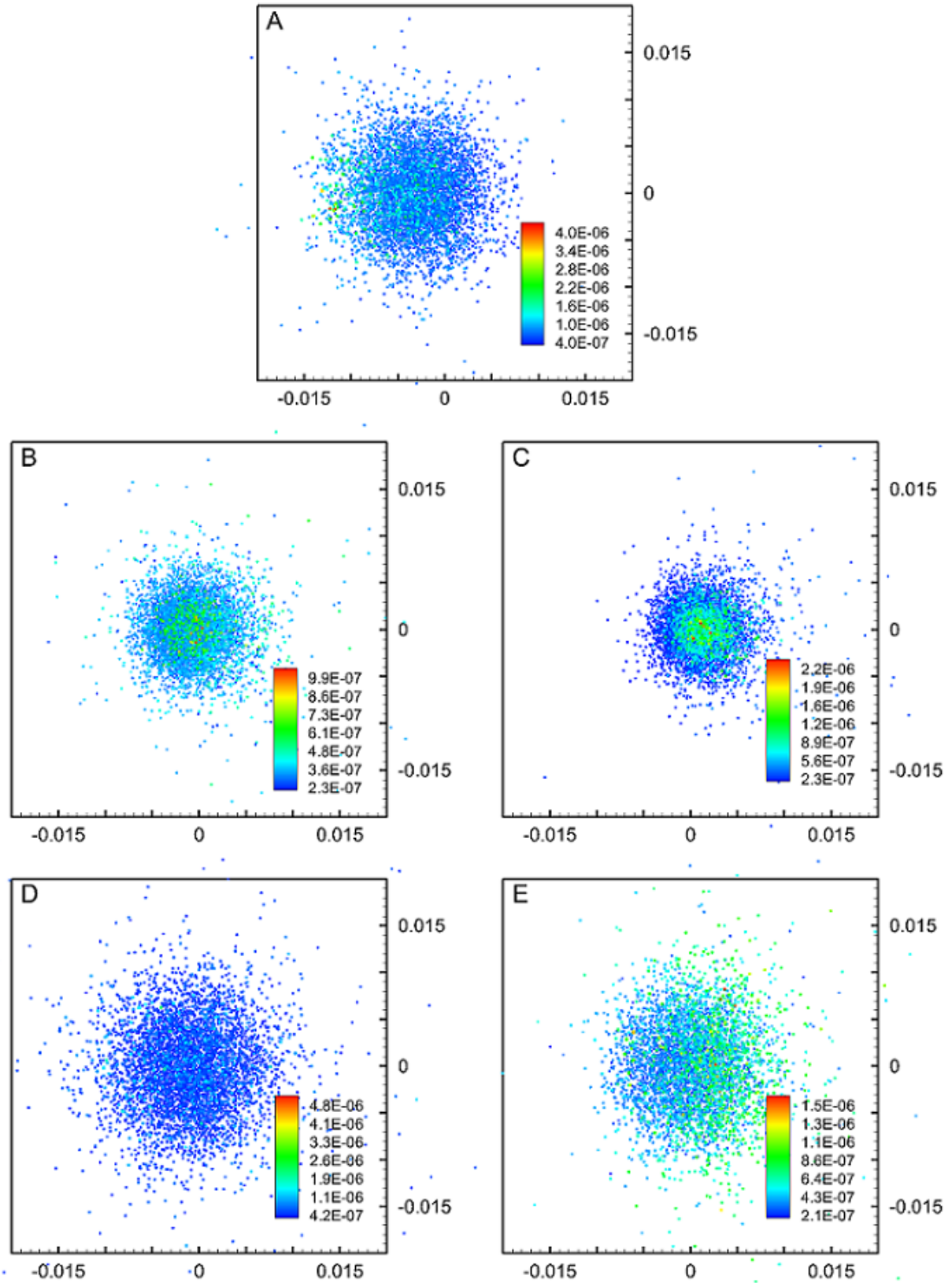


Figure 34: Finished surface of the substrate for cases A to E, colored by the height from the substrate's surface.

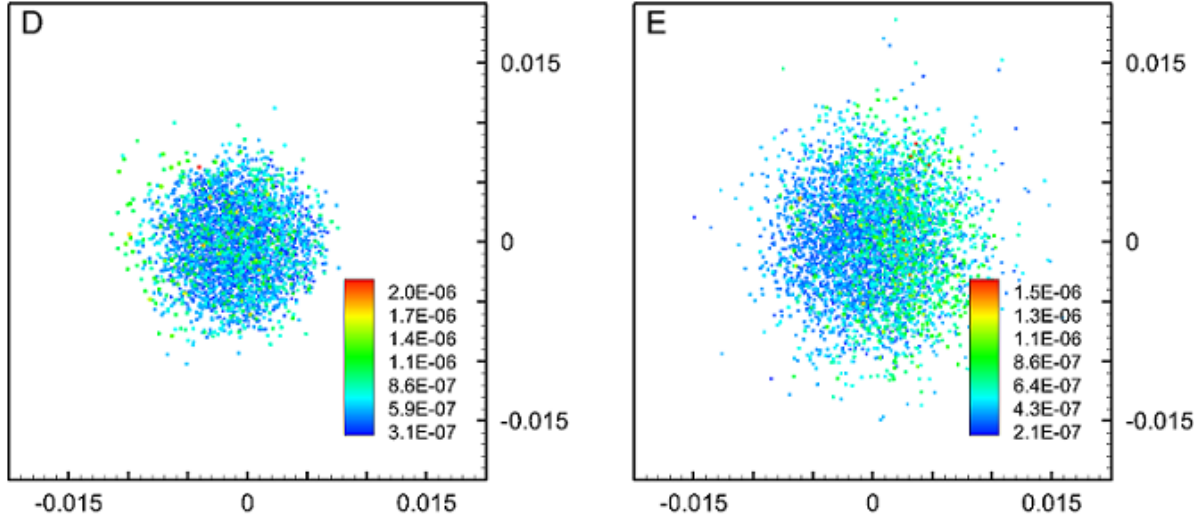


Figure 35: Finished surface of the substrate for cases D and E taking particle temperatures into account, colored by the height from the substrate's surface.

when the spread and recoil of the droplet have already finished and the shape of the splat is not going through any significant changes.

In the first case, the initial temperature for the droplet is $2985K$. This temperature is slightly above solidification point of YSZ. Results for this test have been shown in figure 36. Since the drops here are close to their melting point, solidification occurs shortly after they come in contact with the substrate. This prevents any significant pore formation near the step dent on the surface. However, as test cases described in table 5 show, with the right choice of parameters for the torch and injection, drops reaching the substrate are at higher temperatures, mostly way above the melting point of YSZ. Hence, the same test case is repeated here with now an initial temperature of $3500K$ for the droplets. Results for this case have been shown in figure 37. In these cases, as the droplet needs more time to solidify, the spread and recoil occurs while the droplet has not lost enough heat for solidification. The impact this time is being controlled by the momentum force spreading the drop over the step boundary and surface tension forces acting upon it. Here the pore that is formed is nearly a quarter of circle whose radius is very close to the the step height. A possible explanation for this behaviour might be due to large surface tension magnitude of molten YSZ, which forces the splat to form a nice curvature over the discontinuity. It is evident where the temperature was close to melting point of YSZ, the solidification process has prevented pore formation.

An important case where gaps and voids may appear is during the coating process of a rough surface. Several researches like the works of Xue et al. [54], Shinoda et al. [55], and Parizi et al. [56] have focused on this topic, using a patterned substrate making conditions better for studying. In these studies, YSZ droplets are impacting patterned solid surfaces. The size of these droplets, however, are typically large, in the orders near $15\mu m$. As this size is large compared to SPS-generated particles, an alternative test is used. Here, seven droplets with a size of $3\mu m$ have been used on the same substrate.

Before seeing results for this case, for comparison reasons, initially two test cases similar

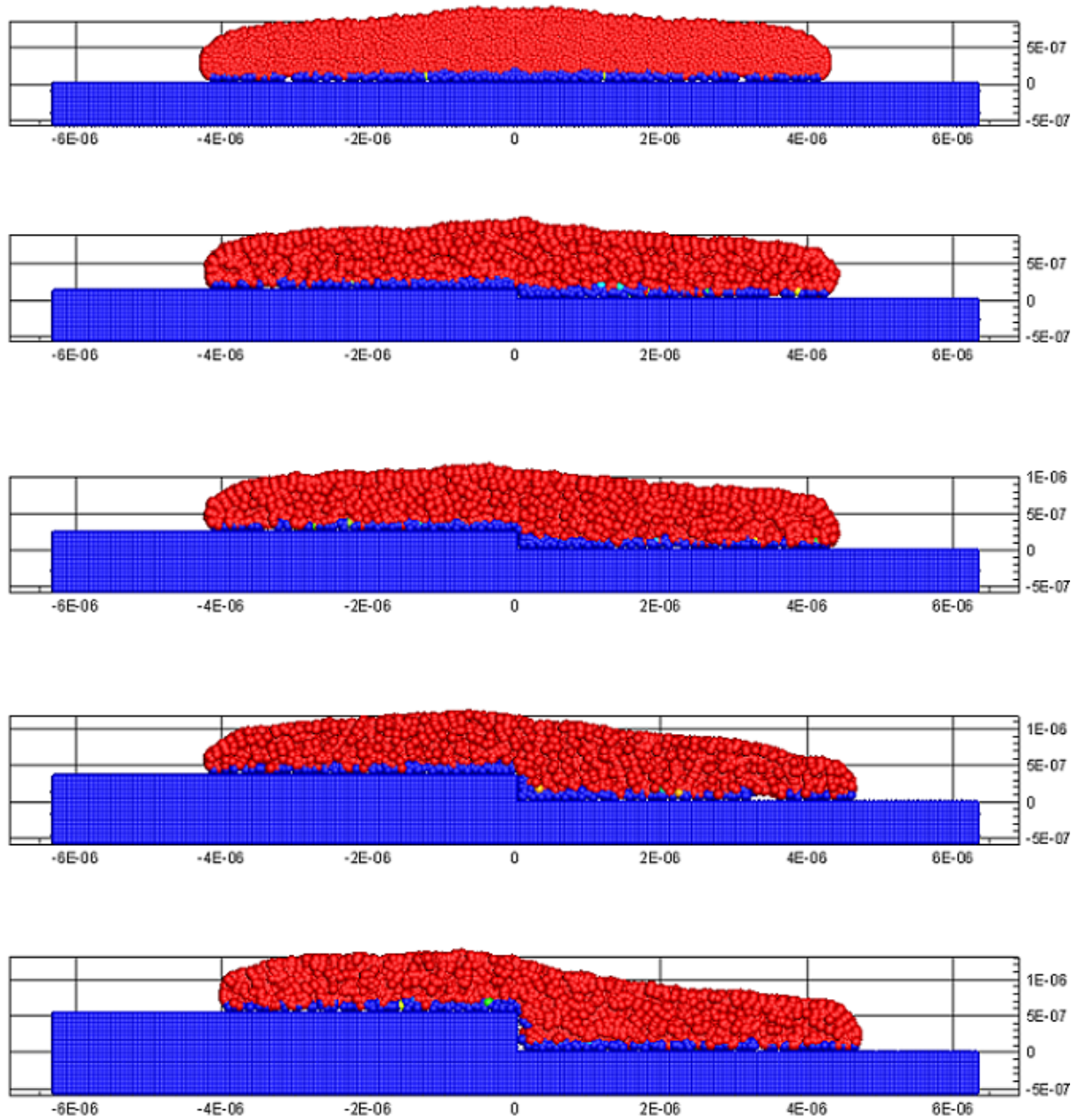


Figure 36: Normal impact of droplet with a radius of $3\mu m$ on flat surface against surfaces with step sizes of 0 , 0.12 , 0.24 , 0.36 , and $0.54\mu m$, from top to bottom respectively. Impact velocity is $150m/s$ and the initial temperature for the droplet and the substrate are 2985 and $300K$. Current time for all cases is $0.1\mu s$.

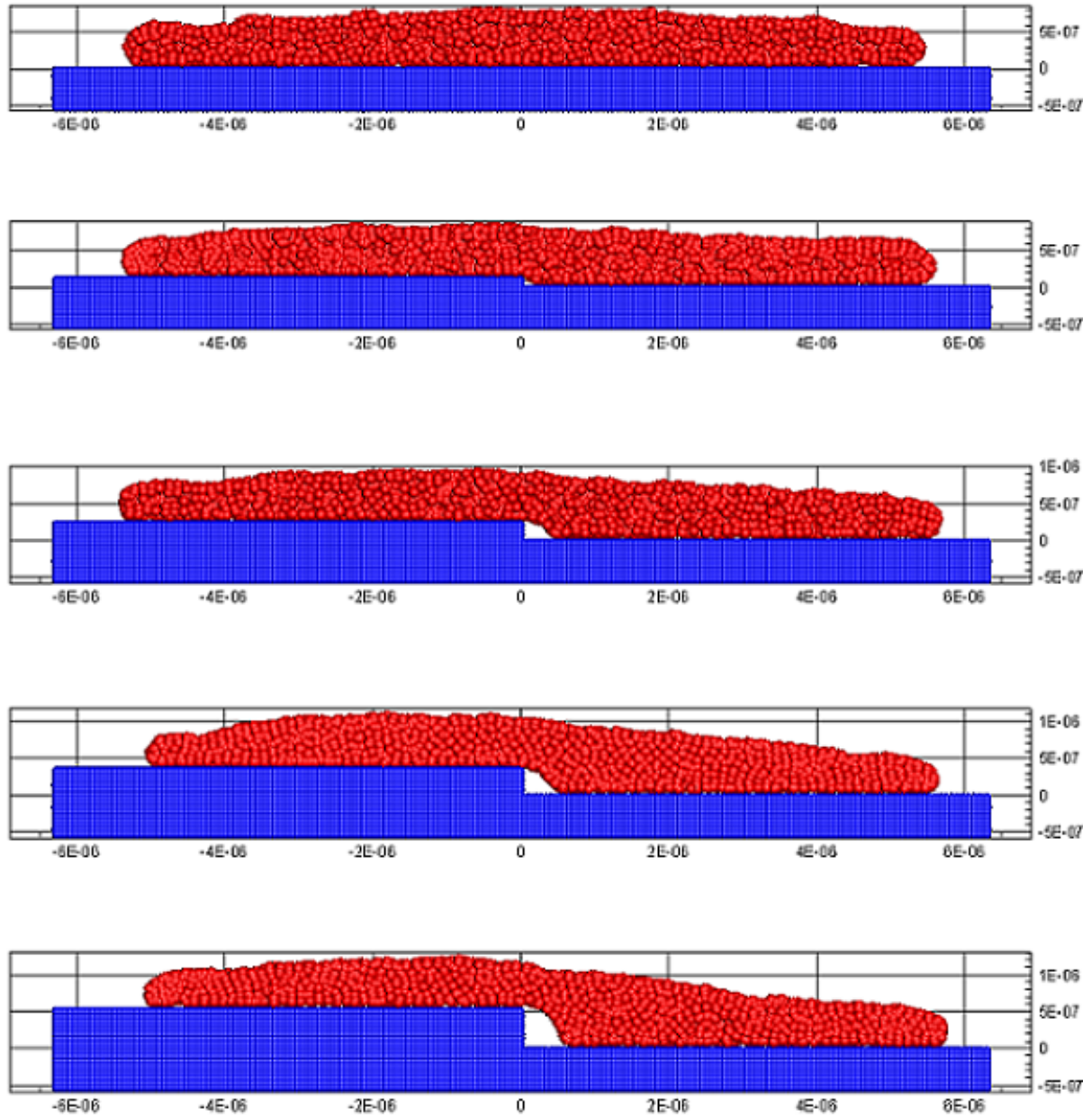


Figure 37: Normal impact of droplet with a radius of $3\mu\text{m}$ on flat surface against surfaces with step sizes of 0 , 0.12 , 0.24 , 0.36 , and $0.54\mu\text{m}$, from top to bottom respectively. Impact velocity is 150m/s and the initial temperature for the droplet and the substrate are 3500 and 300K . Current time for all cases is $0.1\mu\text{s}$.

to previous studies are conducted here. In the first, similar to Xue et al. [54], a drop with diameter of $18\mu m$ is impacting a patterned solid surface at a velocity of $250m/s$ and temperature of $3173K$. The surface is patterned with columns with a width of $4\mu m$, height of $3.3\mu m$, and distance of $1\mu m$. Schematic drawing for this test is shown in figure 38. Results of this simulation are shown in figures 39 to 41. The impact point here has been located over the middle solid column. In the second case, similar to Shinoda et al. [55], the same test is repeated, this time with a diameter of $15\mu m$ and the impact point for the droplet is located in the middle of a column void. Results for this simulation are shown in figures 42 and 43. As it can be seen, similar to reports of Shinoda et al., results here show that the YSZ impact will fill 5 voids in the middle of the substrate and get scattered over the rest. Closeup of the three middle voids showing the movement of the solidification front is shown in figure 44. The material in middle column, being in contact with the substrate the longest, has started to solidify first. By near $t^* = 250$, all the material inside the three voids has completely solidified. The rest of the material solidifies here nearly by $t^* = 1000$.

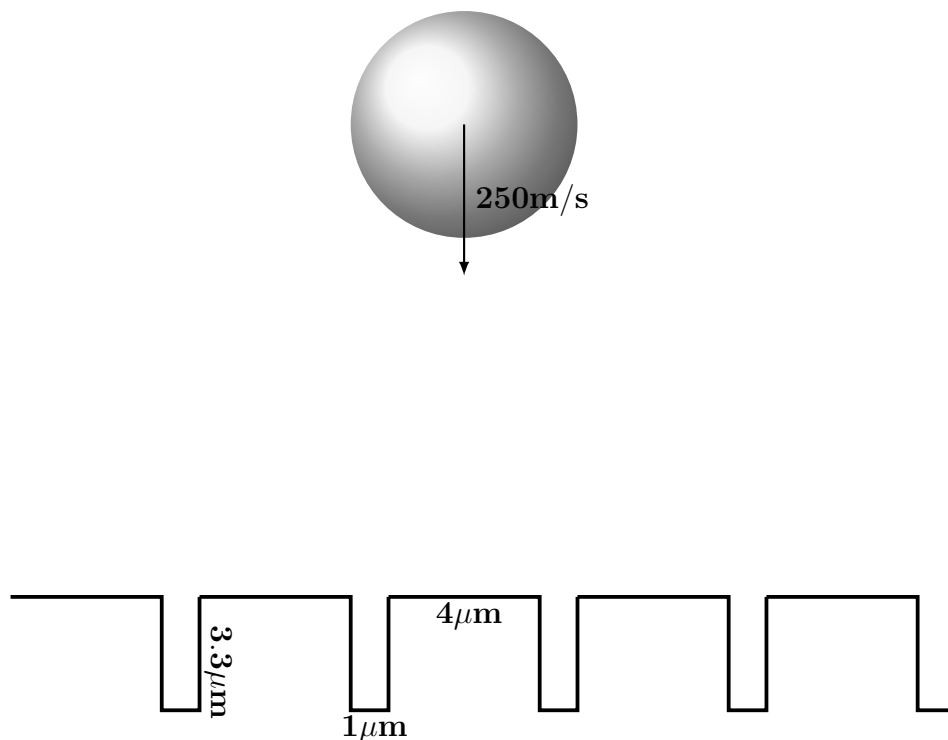


Figure 38: Two-dimensional simulation of droplet with diameter of $18\mu m$ impacting a patterned surface at velocity of $250m/s$.

Void formations inside each column have been compared here against experimental and analytical results of Xue et al. [54]. This comparison is shown in figure 45. The two dots at each distance are for the columns to the left and right of the impact point. Results indicate that for voids close to the impact point, the pressure under the drop will force a

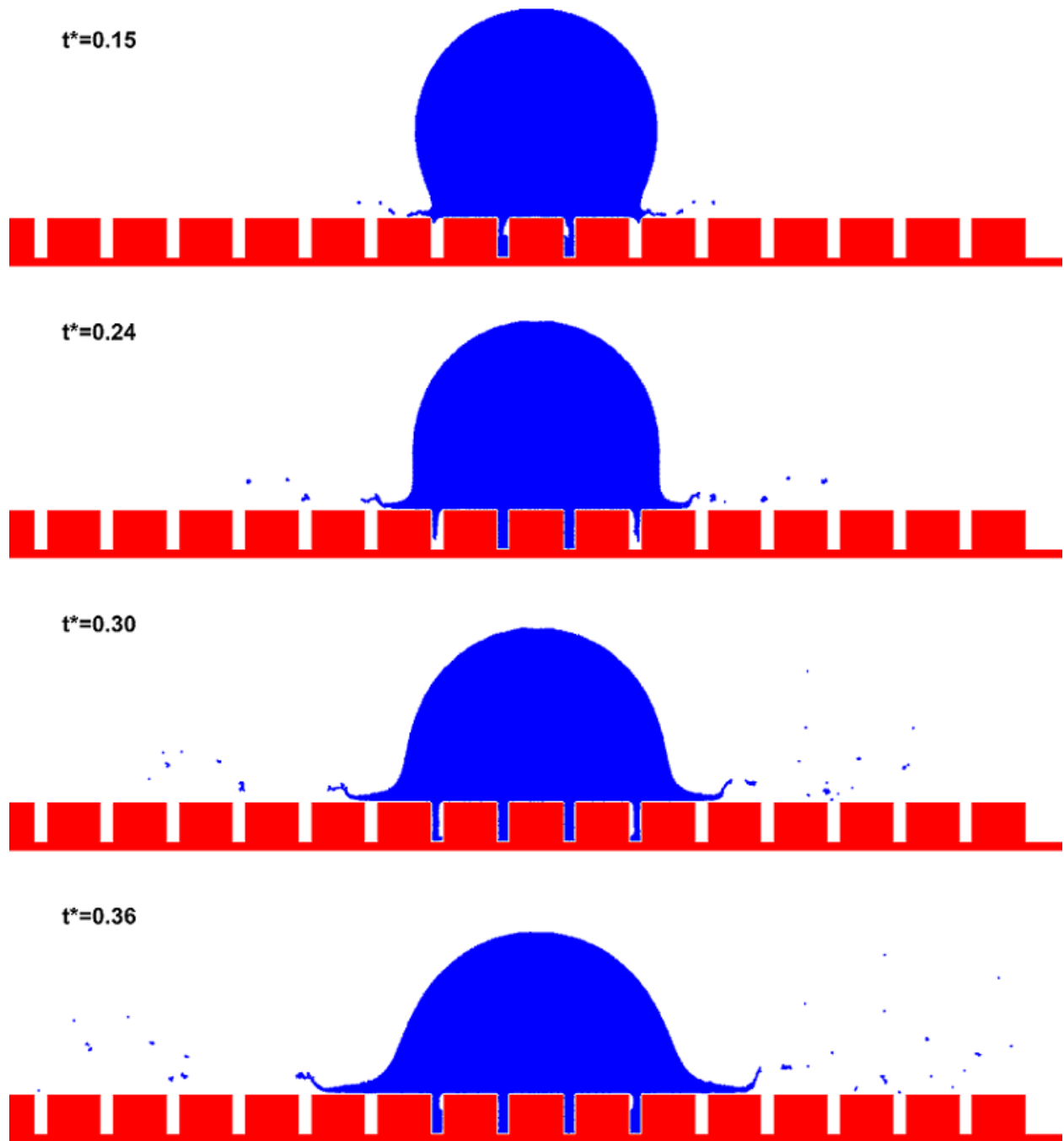


Figure 39: Droplet with a diameter of $18\mu m$ impacting a patterned substrate at velocity of $250m/s$ and temperature of $3173K$.

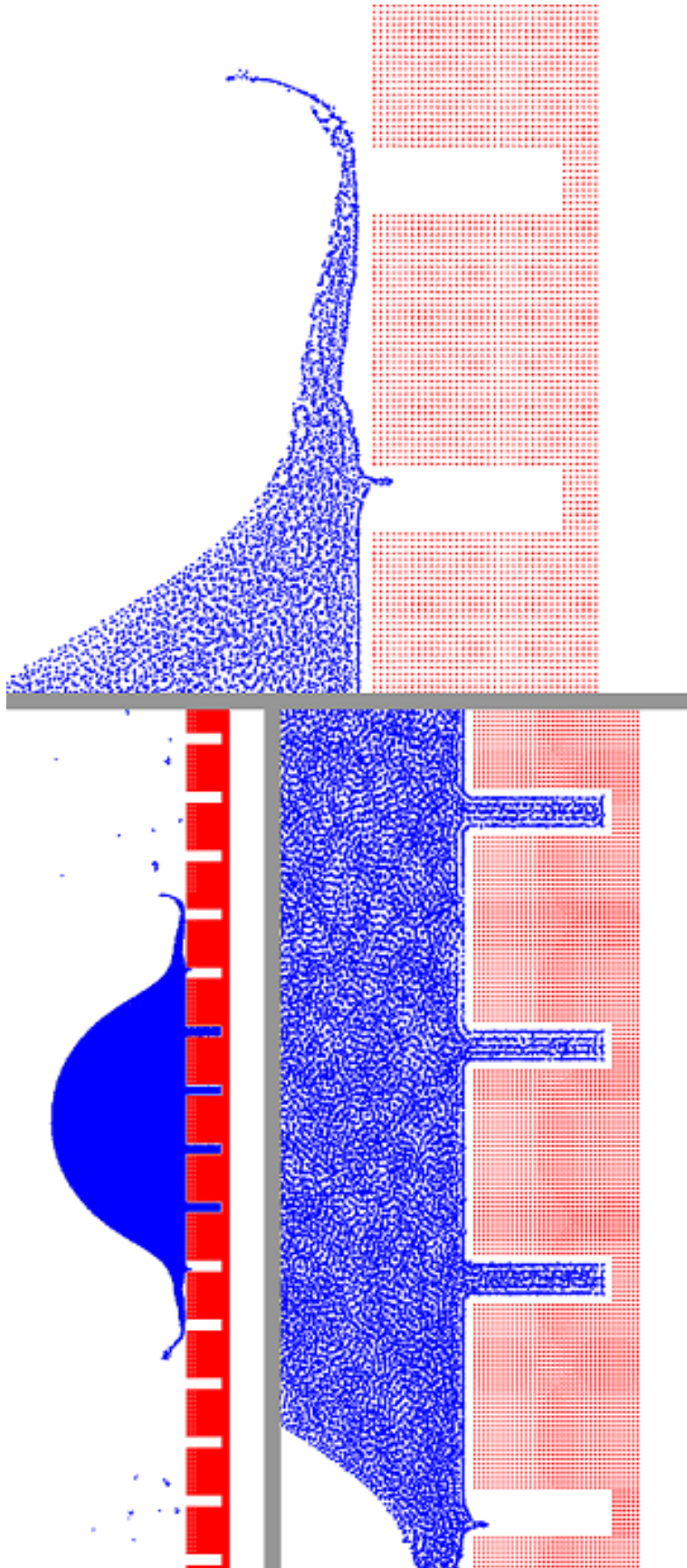


Figure 40: Closeup at $t^* = 0.5$ for a droplet with diameter of $18\mu m$ impacting a patterned substrate at velocity of $250m/s$ and temperature of $3173K$.

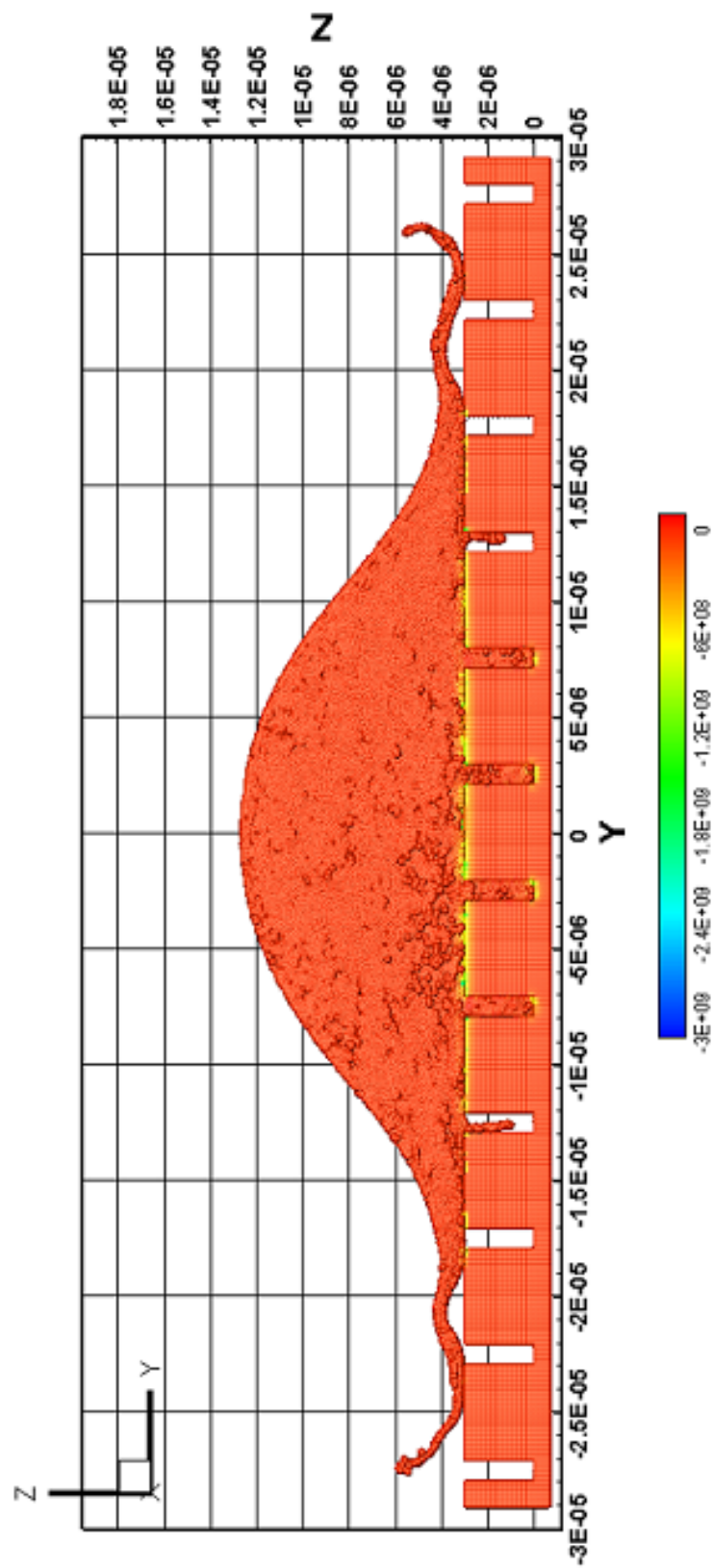


Figure 41: Heat flux magnitude (W/m^2) for a droplet with diameter of $18\mu m$ spreading on a patterned substrate at velocity of $250m/s$ and temperature of $3173K$ at nearly $t^* = 0.6$.

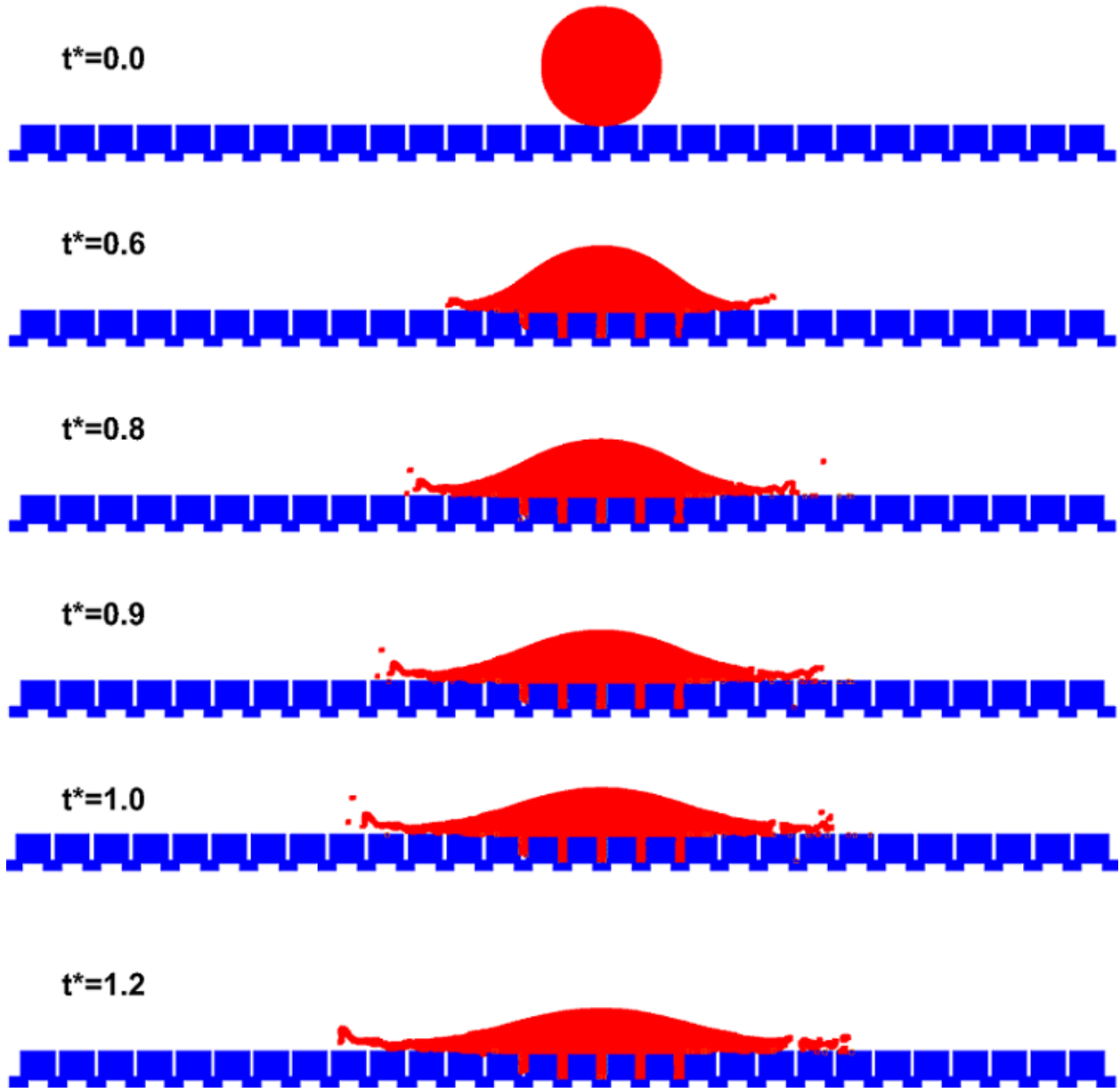


Figure 42: Droplet with a diameter of $15\mu m$ impacting a patterned substrate at velocity of $250m/s$ and temperature of $3173K$.

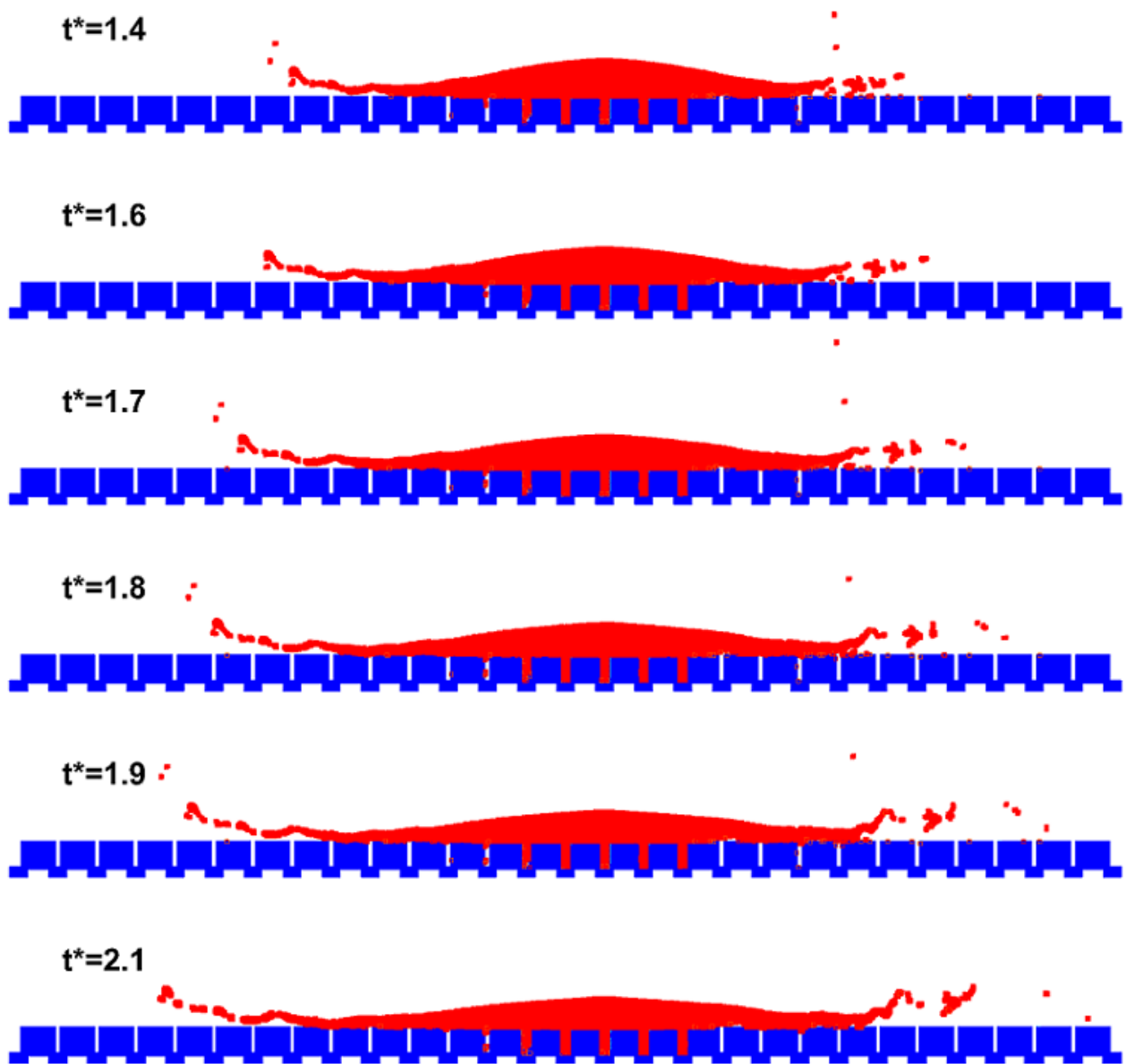


Figure 43: Droplet with a diameter of $15\mu m$ impacting a patterned substrate at velocity of $250m/s$ and temperature of $3173K$.

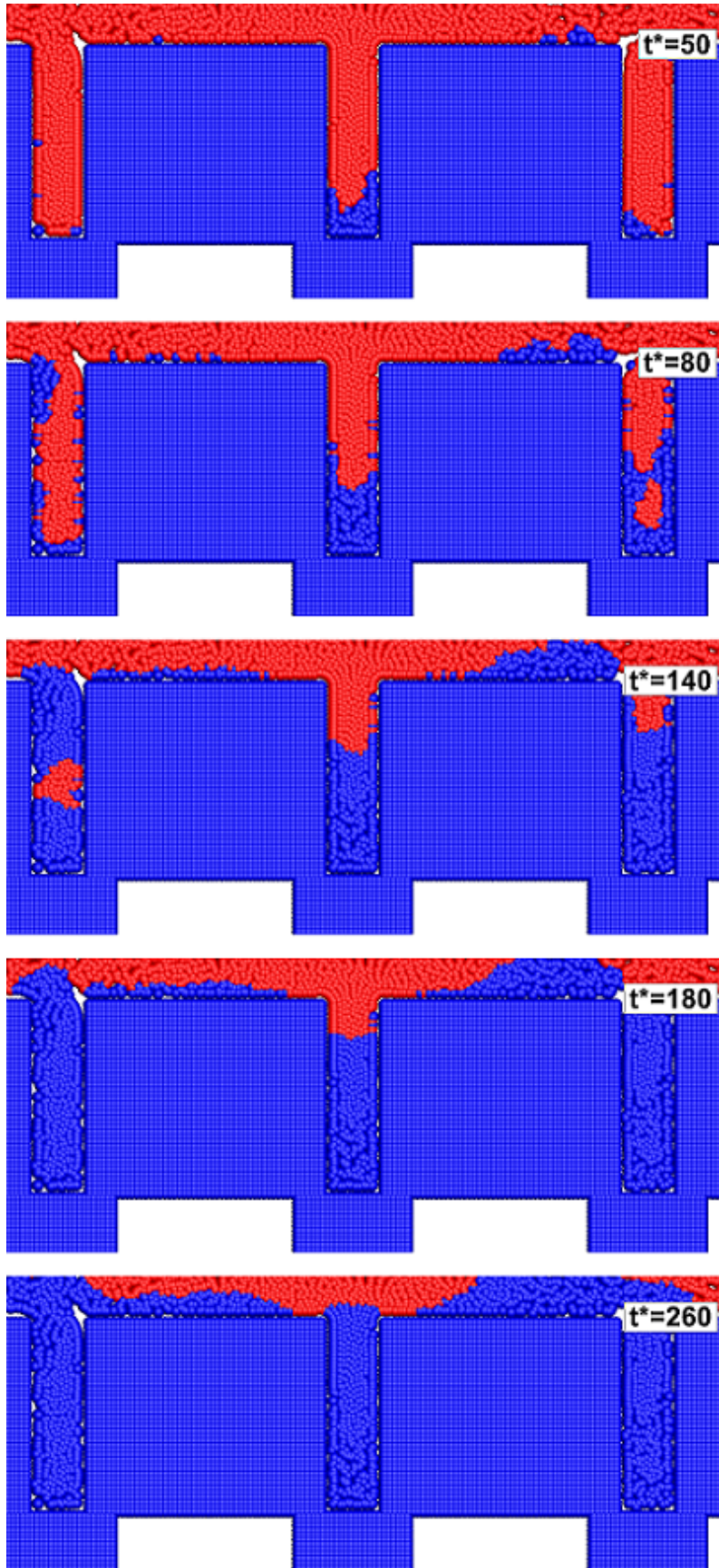


Figure 44: Closeup of the solidification front movement inside the column voids, after impact of a droplet with diameter of $15\mu m$ on a patterned substrate at velocity of $250m/s$ and temperature of $3173K$.

complete filling of the columns. As the splat spreads away, the pressure is lost and the voids are filled with the fluid being forced into the patterns from the sides, and columns are filled with a circulating flow pouring in them. As current simulation is single phase, effects of air entrapment would not be captured. The test case here is also performed in two dimensions, which can be a source for the differences for columns located further from impact point.

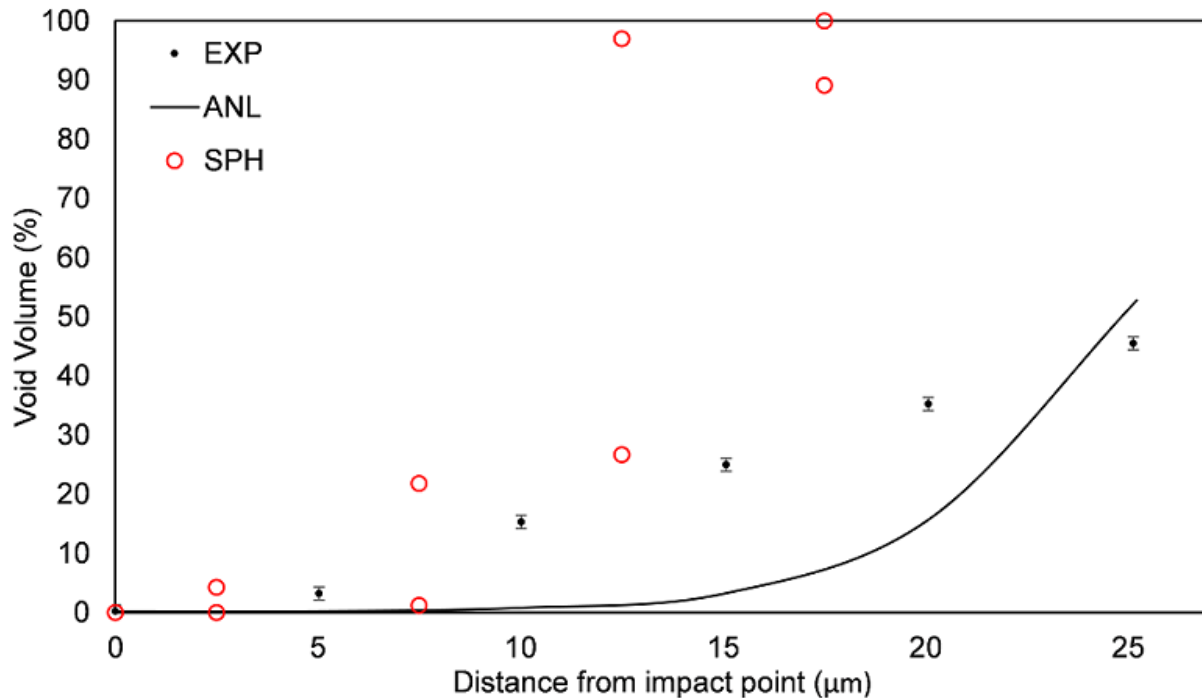


Figure 45: Void formation as a function of distance from impact point, against experimental and analytical results of Xue et al. [54].

As the size of droplets in suspension plasma spraying is in order of a couple of micrometers, these tests are repeated here using droplets with smaller sizes, as shown in 46. As droplets reaching the substrate can have different temperatures, it has also been assumed here that the droplets will reach the substrate at different temperatures above melting point of YSZ. While in theory if the SPS injection is ideal, as shown before, most particles will reach the substrate at temperatures much higher than melting point, in practice, particles will not be all at a high quality. Hence, the temperatures for the seven droplets used in the following test, shown in figure 46, are chosen to be 2985, 3000, 3200, 3400, 3500, 3000, and 3000K, for droplets #1 to #7, respectively. The material for the droplets is YSZ. The substrate has a thermal conductivity of Tin, i.e. $66W/(m \cdot K)$. For simplicity, the rest of physical properties of the substrate are identical to the droplets.

Results for this test at various values of t^* have been plotted in figures 47 to 51. Findings suggest that since the size of the droplets is comparable to the size of patterns, the splat reaching the void first will most likely contribute to filling the void. Also for a void to be filled with more matter, the impact site needs to be closer to its center. For instance, the void to the left of droplet #3 is only partially filled compared to the rest, as the passive impact of this droplet with respect to this void does not provide the splat with a downward spread

direction. Binary collision of spreading splats, as of droplet #1 and #2, can provide the downward momentum direction needed for filling the void. The voids with most penetrated matter here are a byproduct of direct impacts of the droplets, as seen for droplets #4 and #5. Here, droplet #1 spreads over the void to its right. By the time drop #4 reaches this void, the splat of #1 has already covered the opening. As the splat has not yet solidified, droplet #4 pushes in what is already on the top of this void and fills the rest by its own, which can be seen in figure 48. The final filling of this void has come from #1 at the bottom, and #4 in the heart of filling, clearly identified from drop's #1 and #4 initial temperature differences. The temperature of the fillings in voids will be closer to the drop that reaches the void sooner. It has to be noted that all these are under the assumption that impacts are happening shortly one after another, with small time for solidification to occur. If the impacts occur over a longer period of time, there would possibly exist many column openings that are covered by solidified splats. Moreover, effects of air entrapment are neglected here, as the gas phase is not simulated. With the assumption of having impact shortly one after another, final droplets will hit the molten bath formed below them. In this particular test case here, droplets #5-#7 do not come in direct contact with the substrate. Impact of droplets #5 and #6, being close, cancels the inward splashes creating a calm zone in the middle of the substrate. Droplet #7, hits this center, causing a washout where the multiple outward splashes are formed that will carry considerable amount of molten matter away from the impact site.

Heat flux values between the substrate and droplets and also among the droplets at $t^* = 1.9$ is shown in figure 52. Magnitude of velocity and acceleration components due to pressure, viscous, and surface tension forces are shown in figure 53 at $t^* = 1.3$. It becomes evident here that as expected, the effects of surface tension forces are negligible at this stage of simulation compared to pressure and viscous effects. The final material that becomes frozen and fills the void between the columns has been shown in figure 54. The solidification process is completely finished by $t^* = 15000$, which is higher than superposition of 7 droplets on a flat surface ($t^* \approx 1000 - 1500$ for each droplet), even though the substrate surface is expanded due to existence of patterns compared to a flat surface. This can be explained by noting the fact that most of the molten matter has not completely penetrated the voids leaving gaps behind. Hence, the liquid materials are accumulated on top of one another, decreasing the effective area of the substrate that comes in direct contact, leading to lower heat transfer rates to the substrate.

The main assumption in the aforementioned example is having the molten droplets impacting with short time intervals between them. SPS results, however, suggest this will be a rare occurrence. Hence it is reasonable to repeat the same test case here with an improved condition. In the following test case, it has been assumed that each of the 7 droplets will impact individually and solidify. Only then the next droplet impact is executed. Result for this simulation is presented in figure 55. It can be seen that unlike previous cases, the chaotic behavior of splashes are now limited. The largest void penetration this time has been obtained from impact of droplet #3. Both droplets #1 and #3 possess passive impacts with respect to the voids next to them. Droplet #3, however, being nearly $200K$ hotter than #1, has had more time to spread before the solidified layer underneath immobilized it. Final coated splat shows two large voids being formed between the layers. The lower void, between droplet #1 and #4 and the upper void is surrounded by #5, #6, and #7. In the lower void,

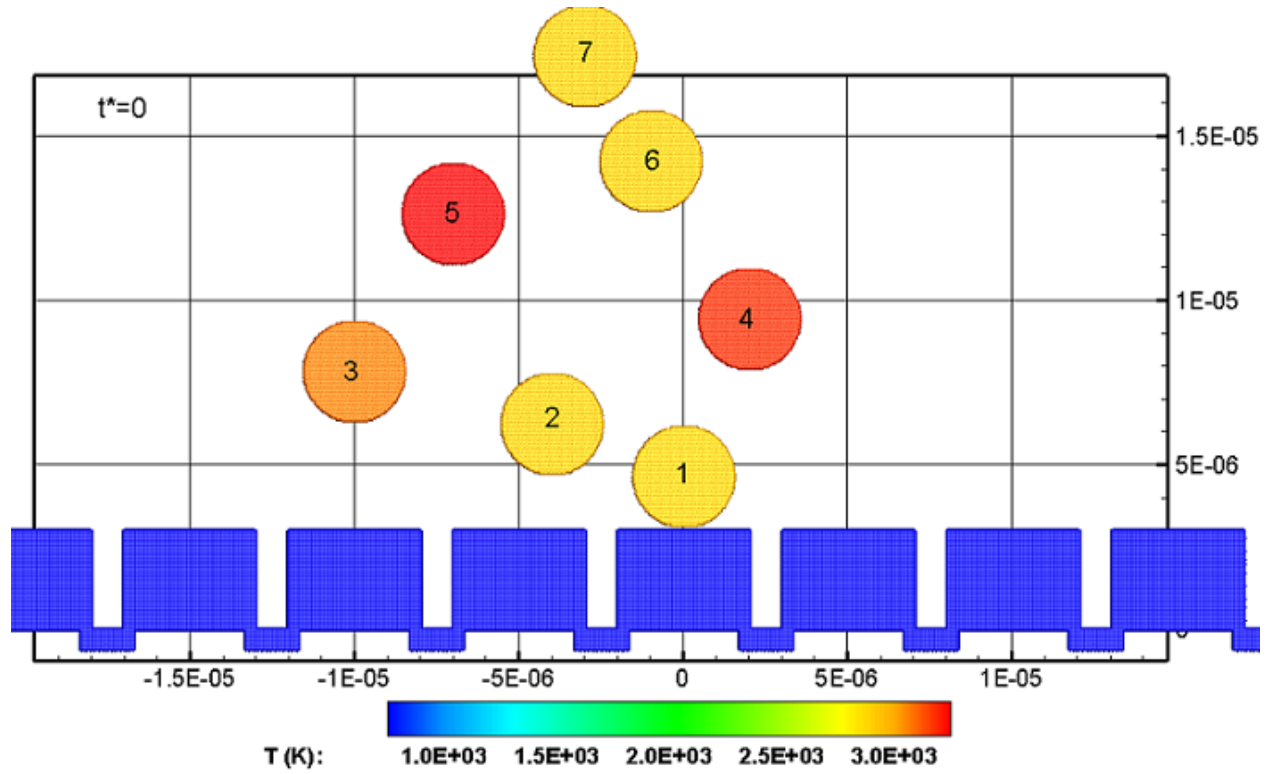


Figure 46: Impact of seven droplets on a patterned surface at $150m/s$, colored by temperature (K).

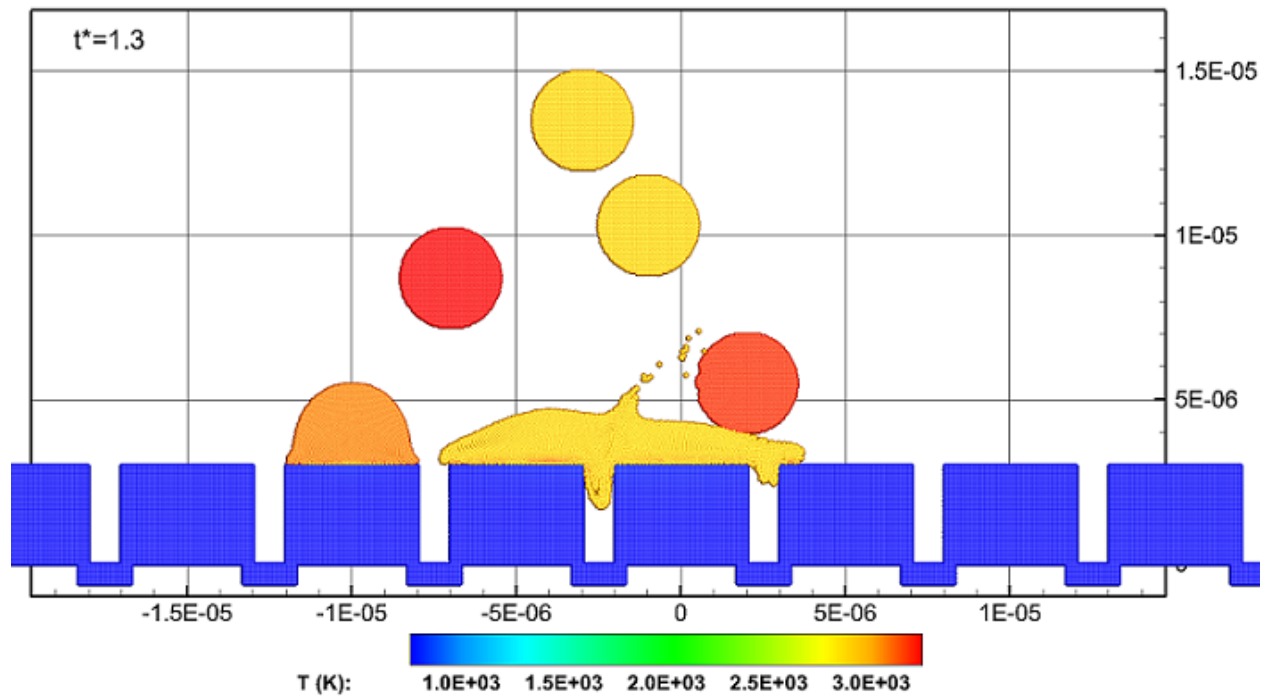


Figure 47: Coating process of a patterned substrate at $t^* = 1.3$, colored by temperature (K).

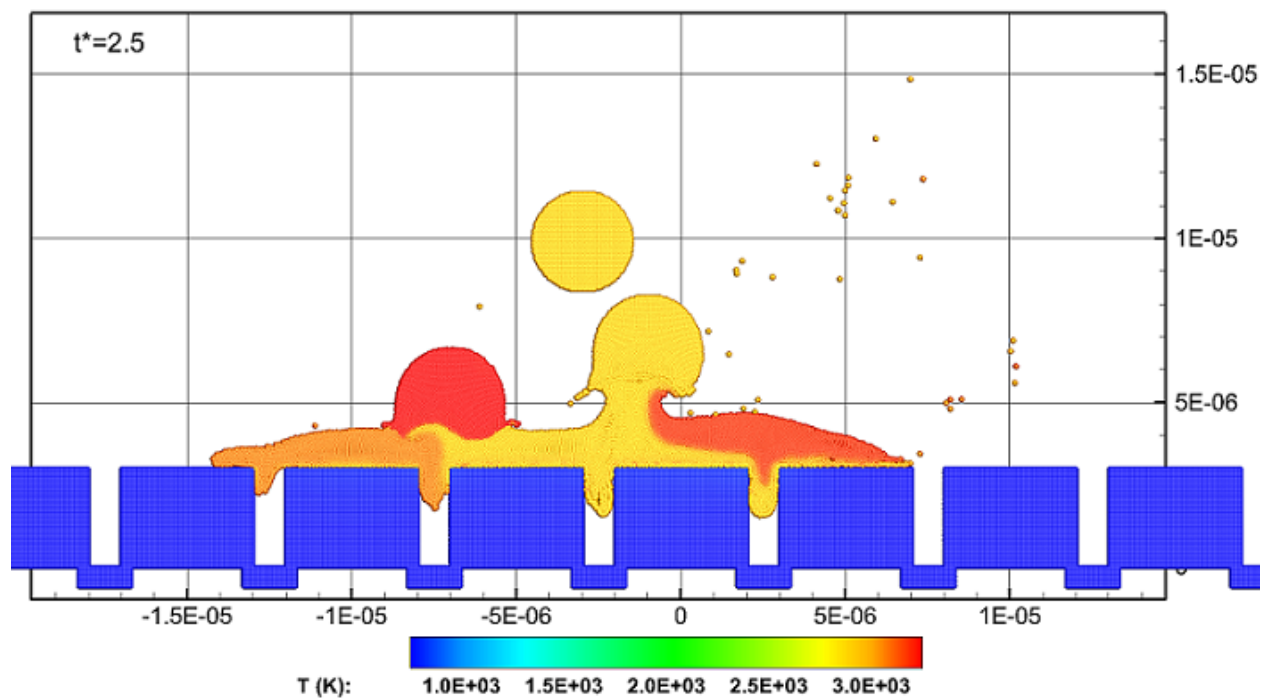


Figure 48: Coating process of a patterned substrate at $t^* = 2.5$, colored by temperature (K).

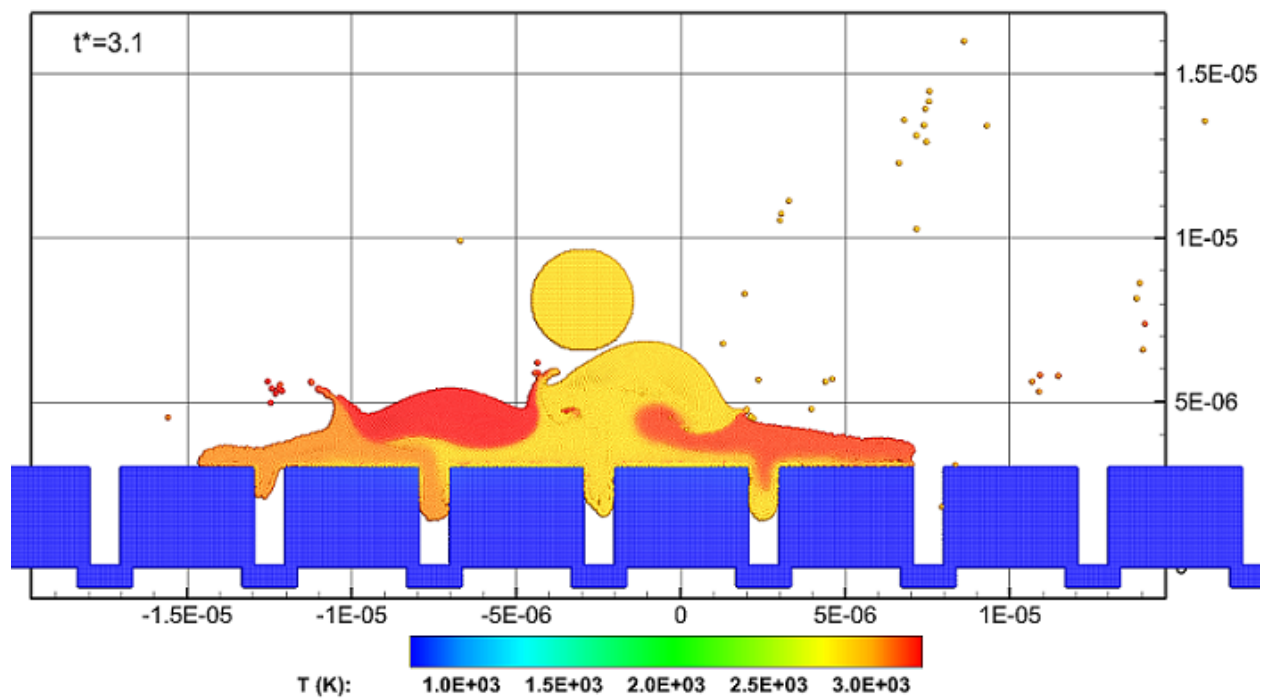


Figure 49: Coating process of a patterned substrate at $t^* = 3.1$, colored by temperature (K).

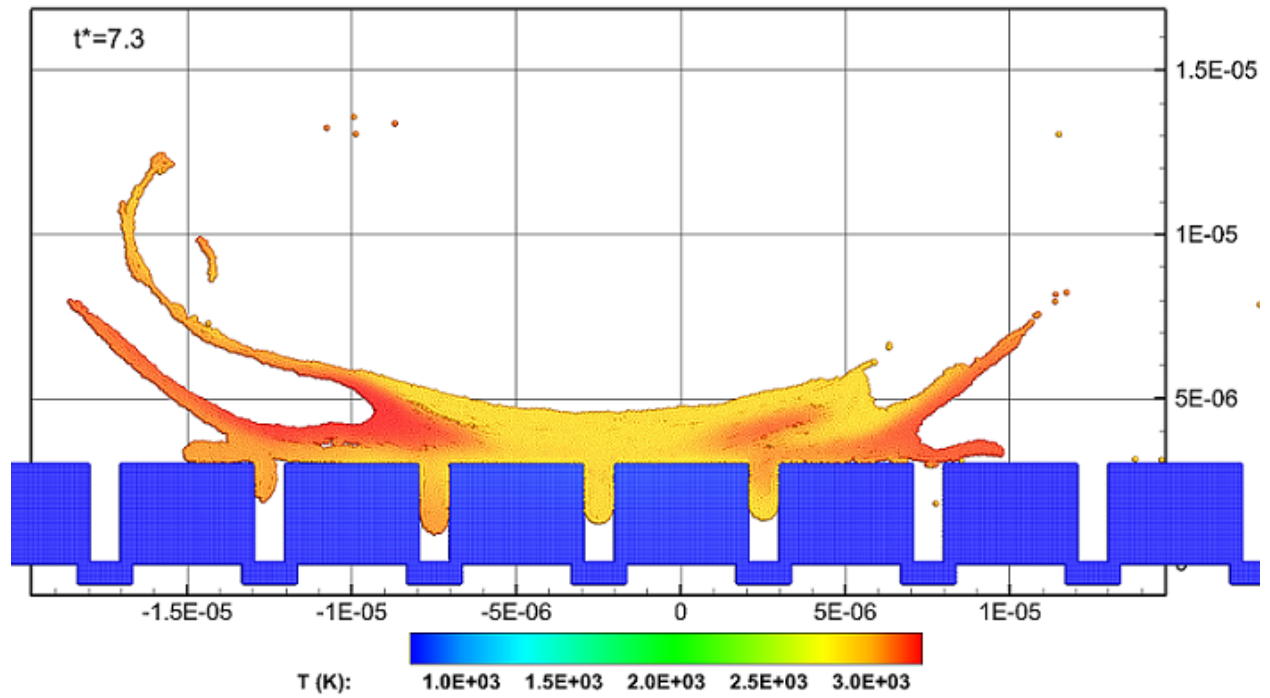


Figure 50: Coating process of a patterned substrate at $t^* = 7.3$, colored by temperature (K).

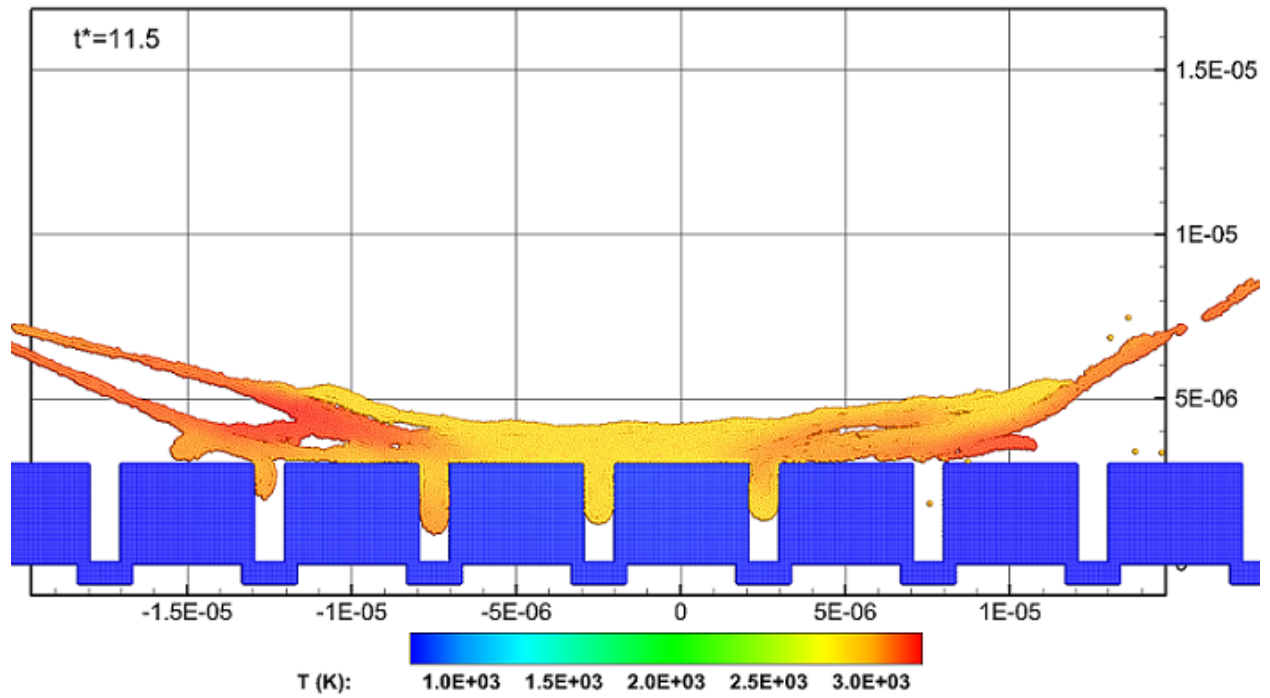


Figure 51: Coating process of a patterned substrate at $t^* = 11.5$, colored by temperature (K).

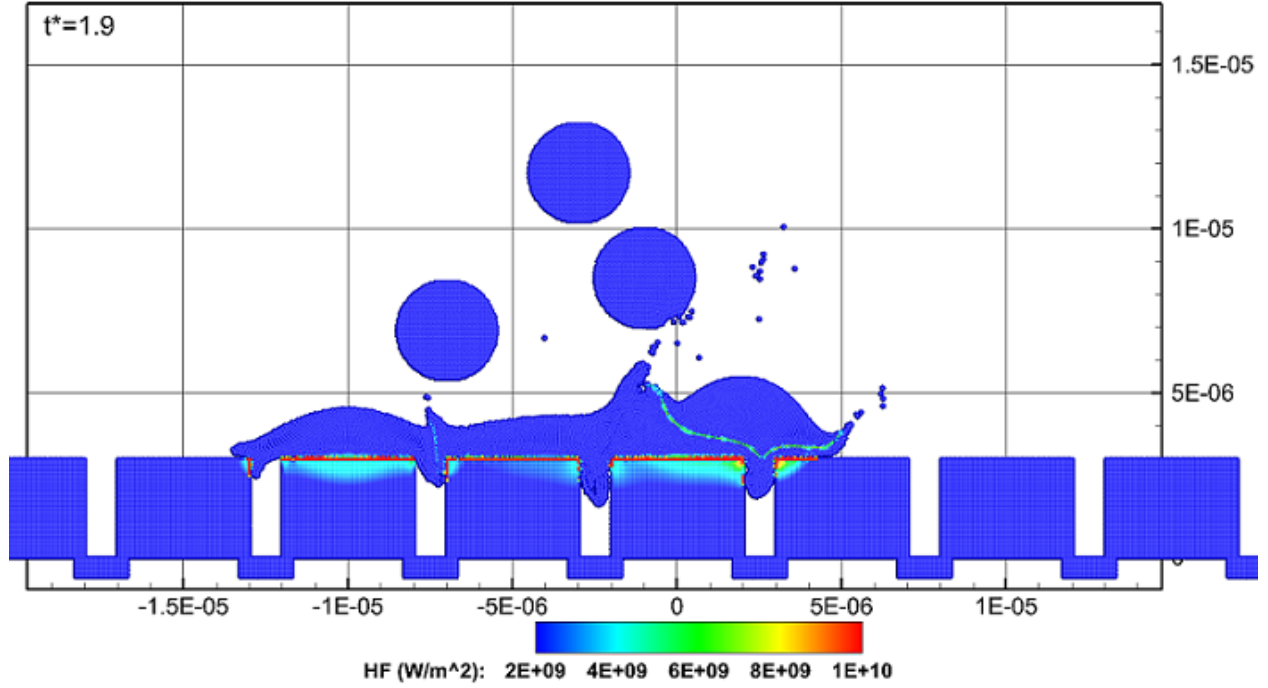


Figure 52: Heat flux magnitude (W/m^2) between substrate and droplets at $t^* = 1.9$.

the initial gap underneath the splat of droplet #1 has a height of $0.25\mu m$, while the gap underneath droplet #6 splat in the upper void measures at nearly $0.5\mu m$, which can explain the size difference between these two voids. The area of these voids are 2.5×10^{-13} and $1.2 \times 10^{-13}m^2$ for upper and lower voids, respectively. Moreover, two smaller voids between the splats and substrate exist with areas of 9.6×10^{-14} and $6.1 \times 10^{-14}m^2$. There are also 32 smaller voids between the splats of the 7 droplets with an approximate average area of $4.7 \times 10^{-15}m^2$ per void.

Using the information on void formations, it is useful to repeat the test case on prediction of final coated surface using Matlab routine and account for the void formations. To save computational time, only test case E has been chosen for further study here. For enhancing the predictions, more SPS droplets for case E have been obtained from the numerical simulation, bringing the total number of droplets gathered on the substrate to near a million, sprayed over $0.61s$. Equation 63 has been used for predicting the spread diameter of SPS particles on the substrate. It has been assumed that molten particles form discs on the substrate. The tangential component of the impact velocities has been neglected here. Results of simulations in previous sections suggested that when a droplet at high temperature impacts an uneven surface, there is a high chance for void formation with a similar size to the height of the void. This has also been included here by making the assumption that droplets impacting the surface with high temperatures will contribute to formation of voids beneath them, although the dimensions of the voids are small compared to other dimensions. Application of these procedures to the example of five droplets of table 4 is shown in figure 56. It can be observed that using this method, the overall behavior of impacts can be predicted as the high and low points in both simulation and prediction are close. Visualization of the substrate's surface for the deposition of this 1 million droplets has been

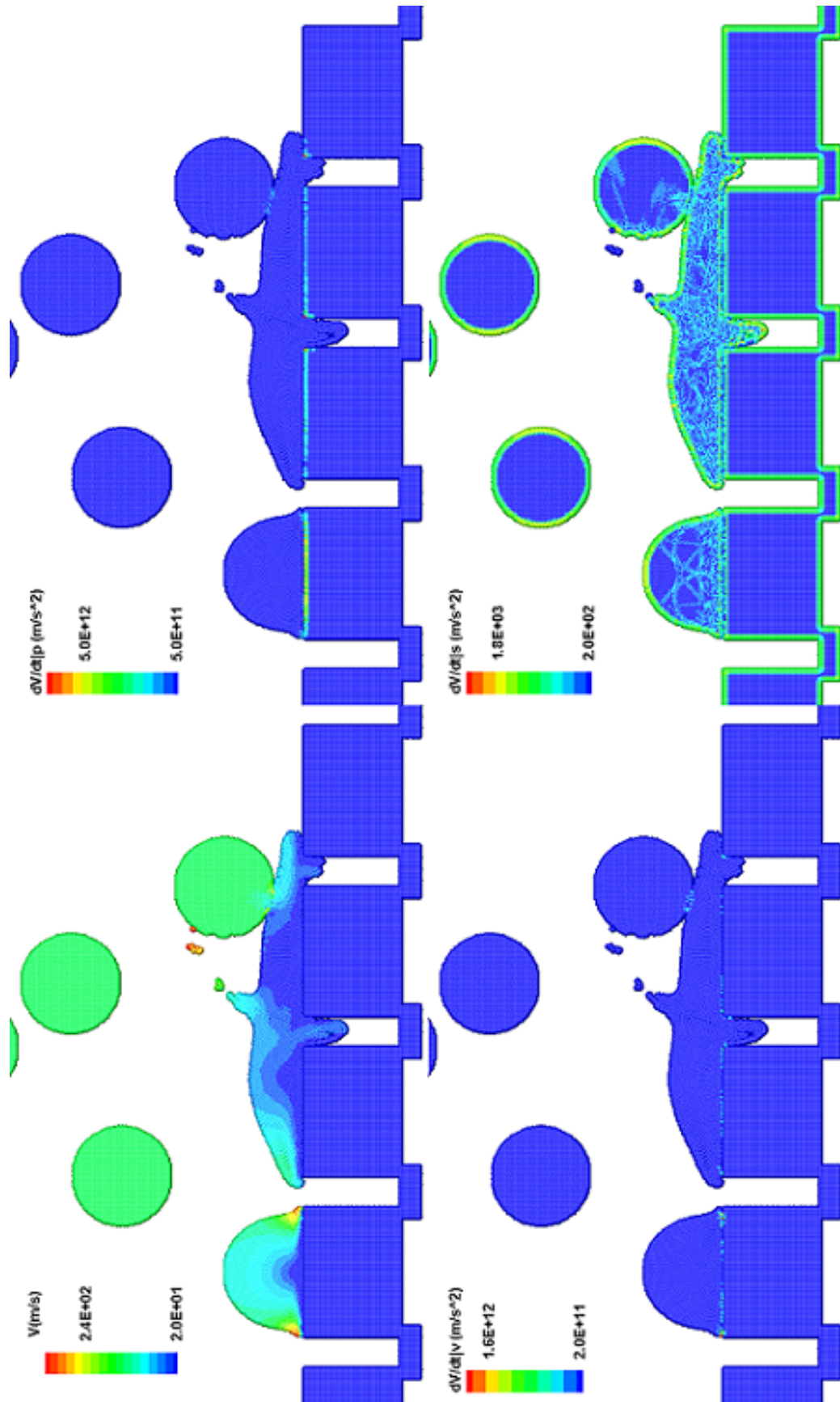


Figure 53: Magnitude of velocity (V) and acceleration components due to pressure (p), viscous (v), and surface tension (s) forces at $\text{Gr}^4 = 1.3$.

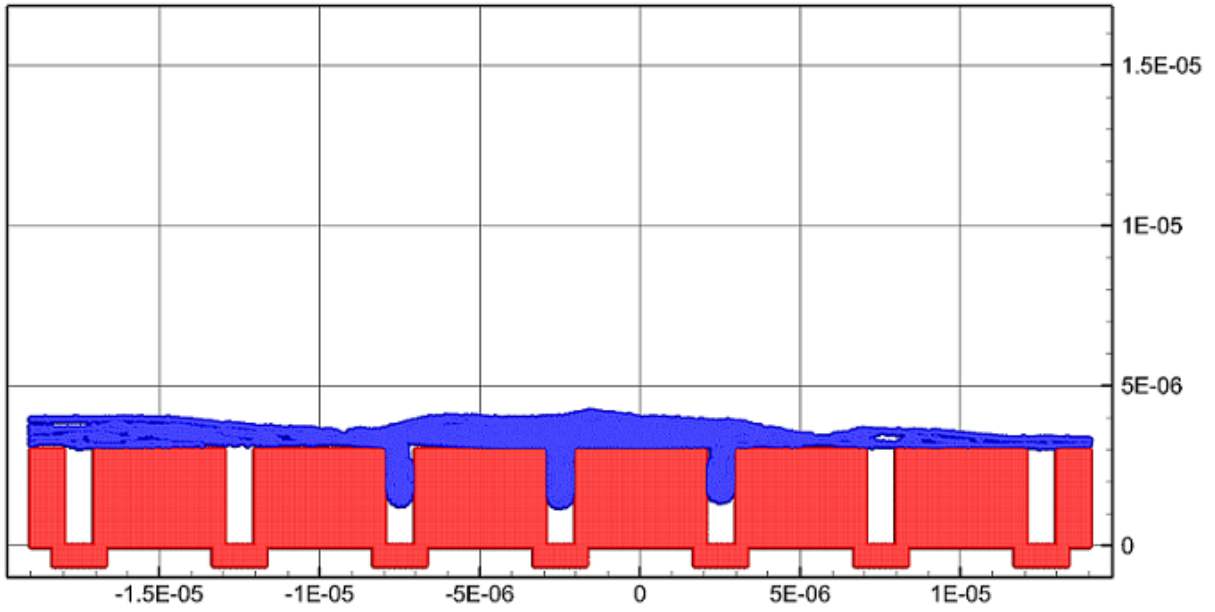


Figure 54: Solidified material left in the voids at $t^* = 15000$.

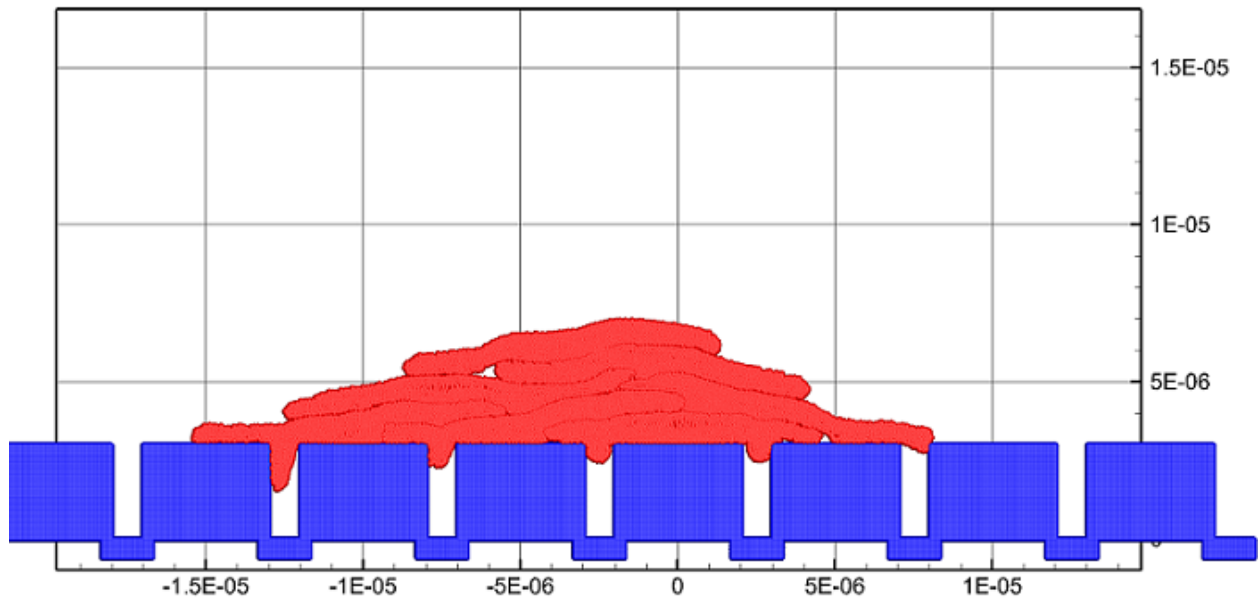


Figure 55: Solidified material on the substrate with the assumption of having individual impacts and solidifications for each of the 7 droplets.

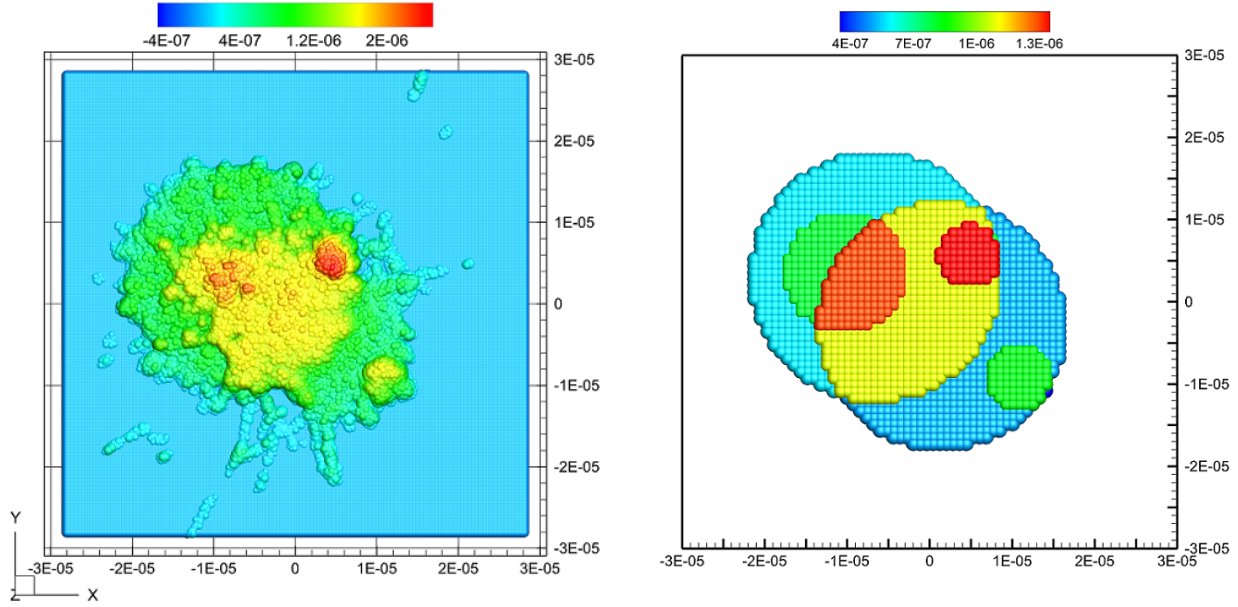


Figure 56: Estimation of substrate coverage using overlapping discs, shown for the case of five droplets in table 4.

shown in figure 57. Results indicate that over the 0.61(s) spray time, 69.80% of the total solid mass of YSZ initially injected into the domain has been deposited onto the substrate, leading to a deposition efficiency of 69.80%. Growth of the area of the solidified material on the substrate as a function of time for this 1 million droplets has been shown in figure 58.

4 Conclusion

Modelling heat transfer with phase change in SPH has been investigated by study of impact and solidification of ceramic droplets on the surface. Release and absorption of latent heat during phase change is accounted for by modifying the enthalpy equation by adding source terms. These models are validated against various available analytical, experimental, and numerical results from literature. Results indicate that the enthalpy formulation provides a reliable platform for free surface flows that are of particular interest in the current study. It also provides the opportunity of modelling pure molten materials without the need of introducing a phase change interval.

Results obtained from previous studies using Finite Volume solution of Suspension Plasma Spraying are also closely examined here using the SPH solver. It is shown that due to mist-like fragmentation of the liquid suspension, the substrate is coated gradually over a large area with sub-micron droplets. Combining the wide range of YSZ droplets collected on the substrate, with the splat formation and solidification results obtained from the SPH solution shows that the surface is coated by isolated splats solidifying far from one another. The droplets studied here will mostly have completed their impact and recoil cycle by $t^*(=tv/D)$ values below 10. For the splat to fully cool down and solidify, it has to remain on the substrate for t^* values near 1000 to 1500. This is mainly due to the high temperature of the

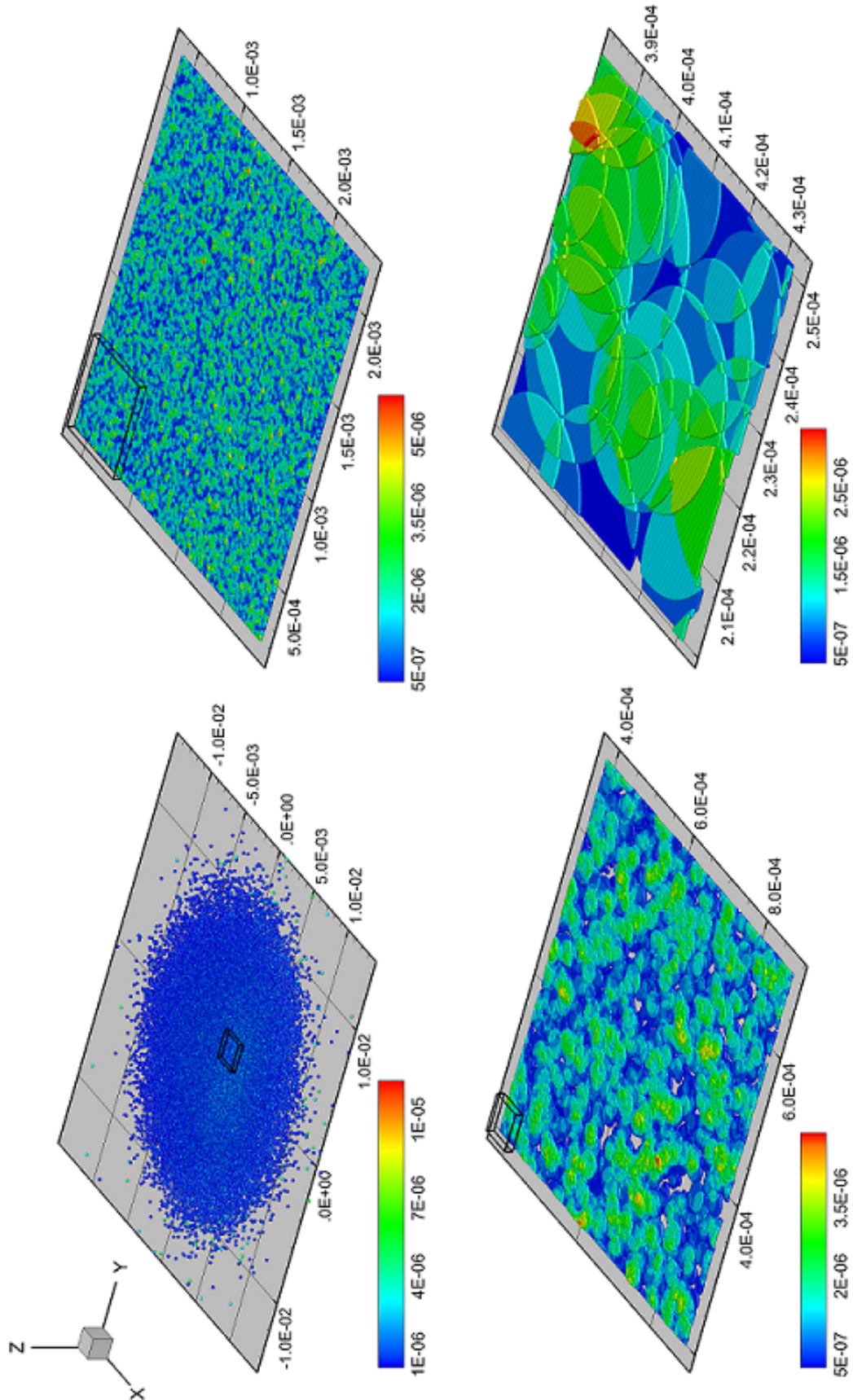


Figure 57: Solidified material on the substrate for 1 million droplets obtained from numerical superposition of splats on the substrate (colored by height from the surface of the substrate).

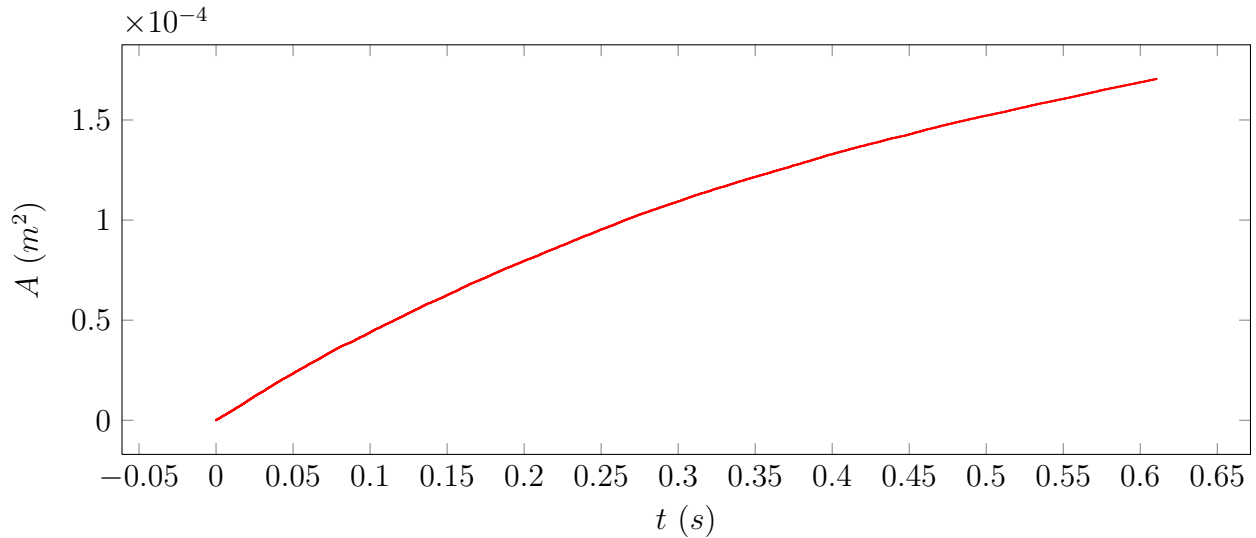


Figure 58: Growth of the area of the solidified material on the substrate as a function of time for 1 million droplets obtained from numerical superposition of splats on the substrate.

molten ceramics at the time of impact. Comparing these results with findings from Finite Volume solution confirms that droplets will solidify before being hit by another splat (wait time between impacts is $t^* = 300,000$ to 5 million), hence it is rare for two droplets to hit one another on the substrate while both being in at molten state. Findings also suggest noticeable differences between the first coating layer compared to others. For YSZ droplets that come in direct contact with metallic substrates, higher thermal conductivity of the substrate material will contribute to fast formation of a solid layer beneath the splat that will eventually immobilize it. For next layers of coating, where YSZ droplets hit solidified YSZ splats, lower thermal conductivities of the ceramic material will delay the cooling process, resulting in a more free spread of YSZ droplets on the substrate.

References

- [1] Mohammad Pasandideh-Fard. *Droplet Impact and Solidification in a Thermal Spray Process*. PhD thesis, University of Toronto, 1998.
- [2] Leon B Lucy. A numerical approach to the testing of the fission hypothesis. *The Astronomical Journal*, 82:1013–1024, 1977.
- [3] Robert A Gingold and Joseph J Monaghan. Smoothed Particle Hydrodynamics: theory and application to non-spherical stars. *Monthly Notices of the Royal Astronomical Society*, 181(3):375–389, 1977.
- [4] Joseph P. Morris, Patrick J. Fox, and Yi Zhu. Modeling low Reynolds number incompressible flows using SPH. *Journal of Computational Physics*, 136(1):214–226, 1997.
- [5] Philip Li-Fan Liu, Harry Hsiu-Jen Yeh, and Costas Synolakis, editors. *Advanced Numerical Models for Simulating Tsunami Waves and Runup*. World Scientific, 2008.

- [6] Bruce Cartwright, PHL Groenenboom, and Damian McGuckin. Examples of ship motion and wash predictions by Smoothed Particle Hydrodynamics (SPH). In *9th Symposium on Practical Design of Ships and Other Floating Structures, Luebeck-Travemuende, Germany*, 2004.
- [7] Amirsaman Farrokhpanah and Javad Mostaghimi. Application of multiphase particle methods in atomization and breakup regimes of liquid jets. In *ASME 2014 4th Joint US-European Fluids Engineering Division Summer Meeting*, page V01AT05A009. American Society of Mechanical Engineers, 2014.
- [8] Amirsaman Farrokhpanah, Babak Samareh, and Javad Mostaghimi. Droplet impact: A GPU based Smoothed Particle Hydrodynamics (SPH) approach. In *ASME 2012 Fluids Engineering Division Summer Meeting*, pages 615–623. American Society of Mechanical Engineers, 2012.
- [9] XY Hu and NA Adams. A multi-phase SPH method for macroscopic and mesoscopic flows. *Journal of Computational Physics*, 213(2):844–861, 2006.
- [10] N Grenier, DL Touze, M Antuono, and A Colagrossi. An improved SPH method for multi-phase simulations. In *8th International Conference on Hydrodynamics, ICHD*, 2008.
- [11] Alexandre M Tartakovsky, Kim F Ferris, and Paul Meakin. Lagrangian particle model for multiphase flows. *Computer Physics Communications*, 180(10):1874–1881, 2009.
- [12] Andrea Colagrossi and Maurizio Landrini. Numerical simulation of interfacial flows by Smoothed Particle Hydrodynamics. *Journal of Computational Physics*, 191(2):448–475, 2003.
- [13] Joseph P Morris. Simulating surface tension with Smoothed Particle Hydrodynamics. *International Journal For Numerical Methods in Fluids*, 33(3):333–353, 2000.
- [14] XY Hu and Nikolaus A Adams. An incompressible multi-phase SPH method. *Journal of Computational Physics*, 227(1):264–278, 2007.
- [15] XY Hu and NA Adams. A constant-density approach for incompressible multi-phase SPH. *Journal of Computational Physics*, 228(6):2082–2091, 2009.
- [16] S Adami, XY Hu, and NA Adams. A new surface-tension formulation for multi-phase SPH using a reproducing divergence approximation. *Journal of Computational Physics*, 229(13):5011–5021, 2010.
- [17] JU Brackbill, Douglas B Kothe, and C1 Zemach. A continuum method for modeling surface tension. *Journal of Computational Physics*, 100(2):335–354, 1992.
- [18] S Nugent and HA Posch. Liquid drops and surface tension with smoothed particle applied mechanics. *Physical Review E*, 62(4):4968, 2000.

- [19] Mohammad Passandideh Fard. Droplet impact and solidification in a thermal spray process: Droplet-substrate interactions. In *Proceedings of the 9th National Thermal Spray Conference*, 1996.
- [20] Vaughan R Voller and C Prakash. A fixed grid numerical modelling methodology for convection-diffusion mushy region phase-change problems. *International Journal of Heat and Mass Transfer*, 30(8):1709–1719, 1987.
- [21] BG Thomas, IV Samarasekera, and JK Brimacombe. Comparison of numerical modeling techniques for complex, two-dimensional, transient heat-conduction problems. *Metalurgical Transactions B*, 15(2):307–318, 1984.
- [22] JS Hsiao and Benjamin TF Chung. An efficient algorithm for finite element solution to two-dimensional heat transfer with melting and freezing. *Journal of Heat Transfer*, 108(2):462–464, 1986.
- [23] AJ Dalhuijsen and A Segal. Comparison of finite element techniques for solidification problems. *International Journal For Numerical Methods in Engineering*, 23(10):1807–1829, 1986.
- [24] PW Cleary, Joseph Ha, John Mooney, and Vikas Ahuja. Effect of heat transfer and solidification on high pressure die casting. In *Proc. 13th Australasian Fluid Mechanics Conference, Melbourne*, pages 679–682, 1998.
- [25] P.W. Cleary, J. Ha, M. Prakash, and T. Nguyen. 3D SPH flow predictions and validation for high pressure die casting of automotive components. *Applied Mathematical Modelling*, 30(11):1406–1427, 2006.
- [26] Paul W. Cleary. Extension of SPH to predict feeding, freezing and defect creation in low pressure die casting. *Applied Mathematical Modelling*, 34(11):3189–3201, 2010.
- [27] Mingyu Zhang, Hui Zhang, and Lili Zheng. Application of Smoothed Particle Hydrodynamics method to free surface and solidification problems. *Numerical Heat Transfer, Part A: Applications*, 52(4):299–314, 2007.
- [28] MY Zhang, H Zhang, and LL Zheng. Simulation of droplet spreading, splashing and solidification using Smoothed Particle Hydrodynamics method. *International Journal of Heat and Mass Transfer*, 51(13):3410–3419, 2008.
- [29] Mingyu Zhang, Hui Zhang, and Lili Zheng. Numerical investigation of substrate melting and deformation during thermal spray coating by SPH method. *Plasma Chemistry and Plasma Processing*, 29(1):55–68, 2009.
- [30] Joseph J Monaghan, Herbert E Huppert, and M Grae Worster. Solidification using Smoothed Particle Hydrodynamics. *Journal of Computational Physics*, 206(2):684–705, 2005.
- [31] Amirsaman Farrokhpanah, Thomas Coyle, and Javad Mostaghimi. Numerical study of suspension plasma spraying. *Journal of Thermal Spray Technology*, 26(1-2), 2016.

- [32] Gui-Rong Liu and Moubin B Liu. *Smoothed Particle Hydrodynamics: A Meshfree Particle Method*. World Scientific, 2003.
- [33] J J Monaghan. Smoothed Particle Hydrodynamics and its diverse applications. *Annual Review of Fluid Mechanics*, 44:323–346, 2012.
- [34] Alexandre M Tartakovsky and Paul Meakin. A Smoothed Particle Hydrodynamics model for miscible flow in three-dimensional fractures and the two-dimensional Rayleigh–Taylor instability. *Journal of Computational Physics*, 207(2):610–624, 2005.
- [35] Douglas Enright, Ronald Fedkiw, Joel Ferziger, and Ian Mitchell. A hybrid particle level set method for improved interface capturing. *Journal of Computational Physics*, 183(1):83–116, 2002.
- [36] David W Holmes, John R Williams, and Peter Tilke. Smooth Particle Hydrodynamics simulations of low Reynolds number flows through porous media. *International Journal for Numerical and Analytical Methods in Geomechanics*, 35(4):419–437, 2011.
- [37] Yasmin Melean, Leonardo Di G Sigalotti, and Anwar Hasmy. On the SPH tensile instability in forming viscous liquid drops. *Computer Physics Communications*, 157(3):191–200, 2004.
- [38] JP Gray, JJ Monaghan, and RP Swift. SPH elastic dynamics. *Computer Methods in Applied Mechanics and Engineering*, 190(49):6641–6662, 2001.
- [39] Joseph J Monaghan. SPH without a tensile instability. *Journal of Computational Physics*, 159(2):290–311, 2000.
- [40] Yiding Cao, Amir Faghri, and Won Soon Chang. A numerical analysis of Stefan problems for generalized multi-dimensional phase-change structures using the enthalpy transforming model. *International Journal of Heat and Mass Transfer*, 32(7):1289–1298, 1989.
- [41] Paul W Cleary and Joseph J Monaghan. Conduction modelling using Smoothed Particle Hydrodynamics. *Journal of Computational Physics*, 148(1):227–264, 1999.
- [42] VR Voller, AD Brent, and C Prakash. Modelling the mushy region in a binary alloy. *Applied Mathematical Modelling*, 14(6):320–326, 1990.
- [43] S Alavi, M Passandideh-Fard, and J Mostaghimi. Simulation of semi-molten particle impacts including heat transfer and phase change. *Journal of Thermal Spray Technology*, 21(6):1278–1293, 2012.
- [44] Horatio Scott Carslaw and John Conrad Jaeger. *Conduction of heat in solids*. Oxford: Clarendon Press, 1959, 2nd ed., 1959.
- [45] AB Crowley. Numerical solution of Stefan problems. *International Journal of Heat and Mass Transfer*, 21(2):215–219, 1978.

- [46] Chi-Sing Keung. *The use of sources and sinks in solving two-dimensional heat conduction problems with change of phase in arbitrary domains*. PhD thesis, Columbia University, 1980.
- [47] Shuai Meng, Rui Yang, Jian-Song Wu, and Hui Zhang. Simulation of droplet spreading on porous substrates using Smoothed Particle Hydrodynamics. *International Journal of Heat and Mass Transfer*, 77:828–833, 2014.
- [48] Gordon R Johnson, Robert A Stryk, and Stephen R Beissel. SPH for high velocity impact computations. *Computer Methods in Applied Mechanics and Engineering*, 139(1):347–373, 1996.
- [49] Joseph J Monaghan and John C Lattanzio. A refined particle method for astrophysical problems. *Astronomy and Astrophysics*, 149:135–143, 1985.
- [50] Shiraz D Aziz and Sanjeev Chandra. Impact, recoil and splashing of molten metal droplets. *International Journal of Heat and Mass Transfer*, 43(16):2841–2857, 2000.
- [51] M Pasandideh-Fard, S Chandra, and J Mostaghimi. A three-dimensional model of droplet impact and solidification. *International Journal of Heat and Mass Transfer*, 45(11):2229–2242, 2002.
- [52] Tommy Che-Ming Wu, Markus Bussmann, and Javad Mostaghimi. The impact of a partially molten YSZ particle. *Journal of Thermal Spray Technology*, 18(5-6):957–964, 2009.
- [53] Mohammad Pasandideh Fard, Y. M. Qiao, Sanjeev Chandra, and Javad Mostaghimi. Capillary effects during droplet impact on a solid surface. *Physics of Fluids (1994-Present)*, 8(3):650–659, 1996.
- [54] M Xue, S Chandra, J Mostaghimi, and HR Salimijazi. Formation of pores in thermal spray coatings due to incomplete filling of crevices in patterned surfaces. *Plasma Chemistry and Plasma Processing*, 27(5):647–657, 2007.
- [55] Kentaro Shinoda, Mehdi Raessi, Javad Mostaghimi, Toyonobu Yoshida, and Hideyuki Murakami. Effect of substrate concave pattern on splat formation of yttria-stabilized zirconia in atmospheric plasma spraying. *Journal of thermal spray technology*, 18(4):609–618, 2009.
- [56] Hamideh B Parizi, L Rosenzweig, J Mostaghimi, S Chandra, T Coyle, H Salimi, L Pershin, A McDonald, and C Moreau. Numerical simulation of droplet impact on patterned surfaces. *Journal of Thermal Spray Technology*, 16(5-6):713–721, 2007.